

QCD Scattering Amplitudes and Prescriptive Unitarity

Sérgio Carrôlo,^a Dmitry Chicherin,^b Johannes Henn,^a Qinglin Yang,^a Yang Zhang^{c,d,e}

^a*Max-Planck-Institut für Physik, Werner-Heisenberg-Institut, Boltzmannstr.8, 85748 Garching, Germany*

^b*LAPTh, Université Savoie Mont Blanc, CNRS, B.P. 110, F-74941 Annecy-le-Vieux, France*

^c*Interdisciplinary Center for Theoretical Study, University of Science and Technology of China, Hefei, Anhui 230026, China*

^d*Peng Huanwu Center for Fundamental Theory, Hefei, Anhui 230026, China*

^e*Center for High Energy Physics, Peking University, Beijing 100871, People's Republic of China*

E-mail: scarrolo@mpp.mpg.de, chicherin@lapth.cnrs.fr, henn@mpp.mpg.de,
qlyang@mpp.mpg.de, yzhphy@ustc.edu.cn

ABSTRACT: We present a systematic framework for the maximally-transcendental part of planar QCD scattering amplitudes and perform the first bootstrap computation of six-gluon MHV amplitudes in massless QCD at the symbol level. By analyzing the *maximal weight projection* of amplitudes at the integrand level, we relate their maximally-transcendental parts to *prescriptive unitarity* integrals. This reveals a novel analytic structure: the prefactors multiplying the functions of maximal transcendentality are identified with the four-dimensional leading singularities of the theory. As a consequence, these prefactors admit a complete classification and can be computed using *on-shell diagrams*, a formalism originally developed in $\mathcal{N}=4$ super Yang-Mills theory. As a concrete application, we determine the two-loop prefactors for planar MHV gluon amplitudes at arbitrary multiplicity. Combining these prefactors with recent advances in the planar two-loop six-point function space and explicit six-point prescriptive-unitarity input, we construct a complete symbol ansatz and uniquely fix the maximally-transcendental part of the two-loop six-gluon MHV QCD amplitudes by imposing physical constraints. The resulting symbols are expressible in a reduced 137-letter alphabet, suggesting that this alphabet is complete for two-loop six-point massless MHV scattering. We also discuss the implications for multi-collinear splitting and multi-soft functions.

Contents

1	Introduction	1
2	Preliminaries	5
2.1	Six-particle kinematics	5
2.2	Iterated integrals and symbols	6
2.3	Color decomposition and planar limit	8
2.4	IR subtraction, UV renormalisation and hard function	9
2.5	Basis of planar six-point two-loop functions	11
3	Maximal weight projection	13
3.1	Maximally-transcendental part of hard functions	13
3.2	IR-finite contributions	15
3.3	IR-divergent contributions	16
4	Prefactors for MHV QCD amplitudes	18
4.1	Non-singlet on-shell diagrams and one-loop prefactors	18
4.2	Two-loop MHV prefactors for pure YM amplitudes	21
4.3	Two-loop MHV prefactors for QCD amplitudes	26
5	Prescriptive unitarity integrals	32
5.1	One-loop prescriptive unitarity integrals and amplitudes	32
5.2	Two-loop prescriptive unitarity integrals	34
5.3	More examples at two loops	36
6	Bootstrapping six-gluon QCD amplitudes	39
6.1	Bootstrapping pure YM amplitudes	39
6.2	From pure YM to QCD hard functions	43
6.3	Six-point two-loop MHV symbol alphabet	47
6.4	From pure YM to $\mathcal{N}=4$ sYM hard functions	47
7	Multi-collinear and multi-soft limits and splitting functions	49
7.1	Review of collinear limit	49
7.2	Review of triple-collinear limits	51
7.3	Two-loop triple-collinear splitting functions	54
7.4	Soft and double-soft limits	55
8	Discussion and outlook	58
A	IBP reduction calculation for the prescriptive unitarity integrals	60

B A review of on-shell diagrams and on-shell functions	61
B.1 Three-particle amplitudes and gluing	62
B.2 BCFW-bridges and Inverse-soft factor	64
C Multi-Regge limit	67

1 Introduction

Nowadays, our understanding of the fundamental interactions of elementary particles is deeply rooted in Quantum Field Theory (QFT), particularly described by Quantum Chromodynamics (QCD) within the Standard Model framework. Scattering amplitudes stand as one of the most crucial observables in perturbative QFT, serving as a vital bridge between theoretical predictions in high-energy particle physics and experimental observations at particle colliders such as the Large Hadron Collider (LHC) (For reviews about modern amplitude study, see [1–3].) The study and computation of scattering amplitudes therefore not only address phenomenological needs, but also deepen our understanding of the Standard Model and QCD, as well as the formal structure of QFT itself, ultimately advancing our grasp of the fundamental principles of nature.

The calculation of QCD amplitudes, particularly at loop level, remains a highly non-trivial task. At the integrand level, whether derived from Feynman rules and Feynman integrals or from unitarity-based methods [4–6], the result is invariably a complicated rational function. An even greater challenge lies in performing loop momentum integrations to obtain final results in terms of transcendental functions, which remains the primary bottleneck in analytic computations. Ultraviolet (UV) and infrared (IR) divergences in scattering amplitudes also make the choice of subtraction schemes a non-trivial issue. Currently, loop-level calculations proceed through several steps: integral reduction via integration-by-parts (IBP) identities [7], evaluation of master integrals using the method of canonical differential equations [8–10], and reconstruction of kinematically-dependent series coefficients via numerical algorithms [11–13]. For parton scattering processes, analytic results are currently available only for four-point amplitudes up to three loops [14–20], and five-point amplitudes up to two loops [21–31]. Beyond five points, as the loop order increases and the number of independent kinematic variables grows, the computational complexity increases substantially.

Recent years have witnessed remarkable advances in the study of scattering amplitudes in planar maximally supersymmetric Yang-Mills theory ($\mathcal{N}=4$ sYM theory [32]; for a recent review, see [33]). As conformally-invariant quantities dual to null polygonal Wilson loops [34–39], scattering amplitudes in $\mathcal{N}=4$ sYM possess elegant structures, enjoying exceptional physical and mathematical properties. Many pivotal modern methods in the study of scattering amplitudes either originated from, or were profoundly shaped by, studies within this theory. These include on-shell methods and BCFW recursion relations [40–44], Grassmannian geometry and the classification of leading singularities [45–48], the

Amplituhedron and Positive Geometry framework [49, 50] at integrand level, as well as symbol technology [51, 52], cluster algebra structures for singularities [53–57] and the amplitude bootstrap [55, 58–69] at integrated level.

Despite the remarkable success achieved within this formal theory, a significant gap remains when applying these advanced tools to experimentally relevant theories, and in particular to QCD scattering amplitudes. First, due to the constraints of dual conformal invariance (DCI) and Yangian invariance [70, 71], scattering amplitudes in $\mathcal{N} = 4$ sYM are fully governed by the Bern-Dixon-Smirnov (BDS) ansatz at four and five points to all loops [72]. Non-trivial kinematics first appears at six points, where amplitudes depend on just three variables. In contrast, QCD scattering amplitudes, even in the planar limit, already exhibit intricate analytic structures at four and five points. Second, amplitudes in $\mathcal{N} = 4$ sYM are uniform and expressed entirely in terms of maximal transcendental weight functions. QCD amplitudes, on the other hand, contain contributions of mixed transcendental weight as well as rational terms. Studying and computing these rational terms analytically remains highly challenging, even at one loop. So far, only limited analytic results and structural understanding have been obtained.

However, the *principle of maximal transcendentality* reveals striking connections between the observables of QCD and $\mathcal{N} = 4$ sYM (for a recent review, see [73]). It has been observed that the “most complicated terms”, i.e. the maximally-transcendental part, in QCD twist-two anomalous dimensions are the same as in $\mathcal{N}=4$ sYM, due to the fact that gluons give the relevant dominant contribution in the BFKL equation [74, 75]. Related heuristic observations of this principle also include duality between $H \rightarrow 3g$ processes and supersymmetric half-BPS form factors [76–78], anomalous dimensions at higher loops [79, 80], and a duality between Wilson loops with Lagrangian insertions and all-plus YM amplitudes [81, 82]. It is worth noting that, already at one loop, the maximally-transcendental part of the four-gluon QCD amplitude $(-+--)$ exhibits a richer structure than its sYM counterpart. Nevertheless, the maximally-transcendental part of QCD amplitudes shares striking similarities with sYM amplitudes. In particular, the prefactors multiplying maximally-transcendental functions are conjectured to be closely tied to the leading singularities of the theory [83], which are conformal invariant [84]. This observation opens the possibility of applying on-shell methods and advanced tools originally developed in $\mathcal{N}=4$ sYM to the study of QCD amplitudes.

In this paper, we study the two-loop maximal-helicity-violating (MHV) six-gluon amplitude in planar massless QCD, a frontier problem in the analytic computation of QCD amplitudes. With particle momenta restricted to four dimensions, this scattering amplitude depends on seven independent scale-invariant kinematic variables. Important progress has been made recently on two-loop six-point massless integrals and their differential equations. All planar integral sectors have now been computed [85, 86], and the corresponding planar massless hexagonal function space has been constructed. In principle, one could therefore attempt a direct computation by constructing the integrand via Feynman rules and reducing it to master integrals through IBP identities. However, such an analytic calculation would be prohibitively lengthy and cumbersome, while revealing very little structural insight into the amplitude itself. We therefore seek a modification of this procedure.

In this work, we adopt the *symbol bootstrap* method to approach this problem. The

symbol bootstrap is a powerful method for analytically computing perturbative observables, by combining mathematical structures with physical constraints. The procedure begins by constructing a parametrized ansatz: the perturbative series expansion of the observable is expressed as a linear combination of complete symbol basis f_j , associated leading singularities R_i , with undetermined rational coefficients $c_{i,j}$, i.e.

$$\mathcal{A}^{(L)} = \sum_{i,j} c_{i,j} R_i f_j^{(L)}. \quad (1.1)$$

Physical constraints are then systematically imposed to fix these parameters. These constraints include symmetry requirements, analytic behavior in various kinematic limits, and branch-cut consistency conditions. This approach has demonstrated remarkable computational power, enabling the analytic calculation of six- and seven-point scattering amplitudes [55, 58–69], as well as three- and four-point form factors of half-BPS operators in $\mathcal{N}=4$ sYM theory [87–91]. It has been applied for the first time to two-loop QCD amplitudes in the Letter [92]. The present paper refines the bootstrap procedure for QCD amplitudes developed there and generalizes it to more complicated helicity sectors.

To construct the bootstrap ansatz, two types of input are required. First, regarding the symbol basis $f_j^{(2)}$, bootstrap calculations for $\mathcal{N}=4$ sYM scattering amplitudes typically build such bases by forming integrable symbols from the anticipated singularity structure of the transcendental functions. In our case, since the planar hexagonal function space has been fully constructed, it naturally constitutes a complete basis for our bootstrap procedure. Second, in this work we focus solely on the maximally-transcendental part of QCD amplitudes. All corresponding prefactors R_i can be computed using on-shell methods. We demonstrate that these prefactors are completely classified by contours that satisfy triangle power counting, and by their associated maximal cut residues introduced in [93]. In that reference, such contours are argued to form a complete basis for MHV ultraviolet-finite amplitudes. In our context, since the maximally-transcendental part of the amplitude is always decoupled from UV-divergent Feynman integrals, these contours are sufficient to classify all relevant prefactors. This therefore provides the foundational ansatz for our bootstrap computations.

It is worth emphasizing that our bootstrap calculation establishes a refined connection between *prescriptive unitarity* [93–96] and the maximally-transcendental part of QCD amplitudes. Prescriptive unitarity refines the generalized unitarity approach by first classifying all independent L -loop contours and then constructing pure Feynman integrals that possess non-trivial, unit leading singularities only on specific contours. These integrals are called prescriptive unitarity integrals. The coefficients of the integrals in the construction of a scattering amplitude integrand are then determined by their corresponding leading singularities. In our approach, the two-loop prescriptive unitarity integrals of Ref. [96] constitute a part of the transcendental function basis. The connection to prescriptive unitarity not only elucidates the analytic structure of the maximally-transcendental part of QCD amplitudes, but also significantly simplifies our bootstrap computations.

After constructing the ansatz, we proceed to determine the integrated scattering amplitude—bypassing the cumbersome IBP reduction—by imposing mathematical and

physical consistency conditions such as spurious pole cancelation and (multi)collinear limits. We present the calculation for three independent helicity configurations of the two-loop six-gluon MHV amplitude, covering both pure Yang–Mills theory and QCD. The use of information from prescriptive unitarity integrals significantly reduces the number of undetermined coefficients in the ansatz, thereby enabling us to extend the method straightforwardly to QCD amplitudes involving external quarks. In the resulting symbols, we observe the reappearance of the 137-letter alphabet previously identified in related observables [92, 97, 98].

Finally, we derive new results for the triple-collinear splitting and double-soft functions from our bootstrap analysis. In gauge theories, scattering amplitudes exhibit universal factorization properties when subsets of external particles become collinear or soft. In multi-collinear limits [99–105] and multi-soft limits [102, 106–109], amplitudes factorize into lower-point amplitudes multiplied by universal process-independent splitting functions. These splitting functions encode the singular behavior associated with the emission of unresolved particles and depend only on the quantum numbers and kinematics of the collinear or soft partons. The universality of these factorization structures plays a central role in higher-order perturbative calculations, underpinning subtraction schemes for infrared divergences, and providing deep insight into the infrared structure of gauge theories. From our bootstrapped results, we extract two-loop triple-collinear splitting and double-soft gluonic functions at maximal weight. We find that these functions are closely related to their counterparts in $\mathcal{N}=4$ sYM theory, once again highlighting a connection between $\mathcal{N}=4$ sYM and pure YM theory in the maximally transcendental sector.

The paper is organized as follows. In section 2 we review the basic ingredients and notation used throughout this work. In section 3 we discuss the maximal weight projection and the corresponding decomposition of QCD amplitudes. Building on this general structure, in section 4 we compute all linearly independent two-loop prefactors contributing to the maximally-transcendental part of MHV gluonic QCD amplitudes, arising from five types of maximal cuts and corresponding on-shell diagrams. In section 5 we discuss the relation between maximally-transcendental functions and prescriptive unitarity integrals. We list the prescriptive integrals required in this work and provide non-trivial checks of this correspondence using available perturbative data. In section 6 we present the bootstrap computation. We determine all independent MHV helicity sectors, namely $(--++++)$, $(-+-+++)$, and $(-++-++)$, both for pure YM amplitudes and for the N_f^k terms of six-gluon QCD amplitudes, and discuss the properties of the resulting symbols. In section 7, we summarize essential features of multi-collinear/soft limits of QCD scattering amplitudes, which serve as necessary input for the bootstrap. We also extract new multi-collinear/soft splitting functions from our results. We conclude in section 8 and outline future directions. In Appendix A, we provide more details on the computation of prescriptive unitarity integrals via IBP reduction. In Appendix B, we review on-shell diagrams and provide relevant references. Appendix C contains a discussion of the multi-Regge behavior of the amplitudes.

2 Preliminaries

2.1 Six-particle kinematics

In this work, we calculate six-gluon planar massless scattering amplitudes in QCD. These amplitudes are defined on the kinematic space of six outgoing four-momenta satisfying momentum conservation and on-shell conditions, which read

$$\sum_{i=1}^6 p_i = 0, \quad p_i^2 = 0, \quad i \in \{1, \dots, 6\}, \quad (2.1)$$

and we denote $p_{6+i} := p_i$. However, instead of working with the constrained momenta, we employ variables that trivialize both of these conditions simultaneously.

We start by making the massless condition of p_i manifest using the spinor-helicity variables λ_i and $\tilde{\lambda}_i$. These are introduced via the map

$$p_i^\mu \rightarrow p_i^{\alpha\dot{\beta}} \equiv (p_i^\mu \sigma_\mu)^{\alpha\dot{\beta}} = \lambda_i^\alpha \tilde{\lambda}_i^{\dot{\beta}}, \quad (2.2)$$

where the momentum is contracted with the four-vector of Pauli matrices $\sigma^\mu = (\mathbb{1}, \vec{\sigma})$. Notice that the last equality in (2.2) follows from the determinant of $p^{\alpha\dot{\beta}}$ vanishing for a massless momentum. In these variables, Lorentz transformations act linearly. Thus, we can form invariants by contracting helicity spinors with the Levi-Civita tensor ϵ to yield

$$\langle ab \rangle = \epsilon_{\alpha\beta} \lambda_a^\alpha \lambda_b^\beta, \quad [ab] = \epsilon_{\dot{\alpha}\dot{\beta}} \tilde{\lambda}_a^{\dot{\alpha}} \tilde{\lambda}_b^{\dot{\beta}}. \quad (2.3)$$

Helicity spinors are uniquely defined up to a little-group rescaling. This is particularly important because an amplitude involving a particle of helicity h_a is homogeneous under the corresponding rescaling of λ_a and $\tilde{\lambda}_a$,

$$A\left(t_a \lambda_a, \frac{1}{t_a} \tilde{\lambda}_a; h_a\right) = t^{-2h_a} A(\lambda_a, \tilde{\lambda}_a; h_a). \quad (2.4)$$

In this work, we focus exclusively on six-gluon scattering with two negative-helicity gluons. The corresponding tree-level amplitude $A^{(0)}$ is given by the well-known Parke-Taylor (PT) factor, for which we adopt the shorthand notation in the n -point case,

$$\text{PT}_{n,ij} := \frac{\langle ij \rangle^4}{\langle 12 \rangle \langle 23 \rangle \dots \langle n1 \rangle}, \quad (2.5)$$

where i, j label the negative-helicity gluons.

Furthermore, since we consider planar amplitudes, we naturally choose the adjacent Mandelstam variables as a basis of parity-even Lorentz invariants,

$$\{s_{i,i+1} = (p_i + p_{i+1})^2\}_{i=1, \dots, 6} \cup \{s_{i,i+1,i+2} = (p_i + p_{i+1} + p_{i+2})^2\}_{i=1,2,3}. \quad (2.6)$$

However, they are not linearly independent in four-dimensional kinematics, since the momenta of the scattered particles are constrained by a Gram-determinant condition. Because our parametrization of the kinematics is manifestly four-dimensional, this constraint is automatically satisfied.

In addition to solving the on-shell constraints, we can also trivialize momentum conservation. Given an ordering of scattered particles, we arrange their momenta to form a closed polygon. Focusing on the polygon vertices $x_i \in \mathbb{R}^4$ instead of the edges p_i ,

$$p_i = x_{i+1} - x_i, \quad x_7 = x_1, \quad (2.7)$$

ensures that momentum conservation is automatically satisfied. Combining eqs. (2.2) and (2.7), we introduce momentum twistors $Z_i \in \mathbb{P}^3$,

$$Z_i^I = \begin{pmatrix} \lambda_i^\alpha \\ (x_i \lambda_i)^\dot{\beta} \end{pmatrix}, \quad I \in \{1, \dots, 4\}, \alpha, \dot{\beta} \in \{1, 2\}. \quad (2.8)$$

Thus, any collection of six momentum twistors $Z_{1, \dots, 6}$ specifies six massless four-dimensional external momenta that satisfy momentum conservation.

Both constraints in (2.1) are invariant under conformal transformations, which take a particularly simple form in momentum twistors variables. Indeed, momentum twistors transform in the fundamental representation of $SL(4)$ under conformal transformations. The conformal invariants are four-brackets given by contractions of momentum twistors with the Levi-Civita tensor ϵ as follows,

$$\langle abcd \rangle = \epsilon_{IJKL} Z_a^I Z_b^J Z_c^K Z_d^L. \quad (2.9)$$

In order to relate the momentum twistor four-brackets to the spinor-helicity two-brackets, we have to break conformal invariance. Thus, we introduce a point at infinity that corresponds to the infinity bi-twistor

$$I_\infty := \begin{pmatrix} 0 & 0 & 1 & 0 \\ 0 & 0 & 0 & 1 \end{pmatrix}. \quad (2.10)$$

Then, the spinor-helicity brackets are simply given by

$$\langle ij I_\infty \rangle = \langle ij \rangle. \quad (2.11)$$

Finally, the Mandelstam variables are given by ratios of momentum twistor four-brackets,

$$s_{i,i+1} = \frac{\langle i-1 \ i \ i+1 \ i+2 \rangle}{\langle i-1 \ i \rangle \langle i+1 \ i+2 \rangle}, \quad s_{i,i+1,i+2} = \frac{\langle i-1 \ i \ i+2 \ i+3 \rangle}{\langle i-1 \ i \rangle \langle i+2 \ i+3 \rangle}. \quad (2.12)$$

2.2 Iterated integrals and symbols

All transcendental functions appearing in our calculation are Chen iterated integrals with dlog kernels [110]; multiple polylogarithms (MPLs) are among the functions of this type. The transcendental weight counts the number of iterated integrations. The total differential of a weight- w d log-iterated integral $\mathcal{F}^{(w)}$ satisfies the following recursive relation

$$d\mathcal{F}^{(w)} = \sum_i \mathcal{F}_i^{(w-1)} d\log \alpha_i, \quad (2.13)$$

where $\mathcal{F}_i^{(w-1)}$ are weight- $(w-1)$ $d\log$ -iterated integrals, and *letters* α_i are algebraic functions in the kinematic variables of $\mathcal{F}^{(w)}$. Based on (2.13), we introduce the *symbol* map \mathcal{S} for $d\log$ -iterated integrals [51, 52]. This map is linear and defined recursively in weight,

$$\mathcal{S}(\mathcal{F}^{(w)}) = \sum_i \mathcal{S}(\mathcal{F}_i^{(w-1)}) \otimes \alpha_i , \quad (2.14)$$

and $\mathcal{S}(1) = 1$. Thus, the symbol of $\mathcal{F}^{(w)}$ is a tensor product with w entries,

$$\mathcal{S}(\mathcal{F}^{(w)}) = \sum_k c_k \alpha_1^k \otimes \cdots \otimes \alpha_w^k , \quad (2.15)$$

where the coefficients c_k are rational numbers. More generally, if the function $\mathcal{F}^{(w)}$ is a homogeneous linear combination of weight- w $d\log$ -iterated integrals, then the coefficients c_k in eq. (2.15) are the so-called *leading singularities*, and they are typically rational functions of external kinematics. If coefficients c_k are rational numbers, then the corresponding function $\mathcal{F}^{(w)}$ is called *pure*. Furthermore, the full collection of α_i^k forms the *symbol alphabet* of $\mathcal{F}^{(w)}$. The zero loci of the letters are branch-cut singularities of $\mathcal{F}^{(w)}$ and its analytic continuation.

In the method of differential equations [9], for a fixed number of scattered particles and fixed loop order, one constructs a basis of dimensionally regularized *master integrals*. In the *uniform transcendental* (UT) basis, the master integrals satisfy canonical differential equations

$$d\mathbf{I} = \epsilon \, dA \cdot \mathbf{I} , \quad (2.16)$$

with the dimensional-regularization parameter ϵ factored out. The matrix dA depends on the external kinematic variables only in the following way,

$$dA = \sum_i A_i \, d\log W_i , \quad (2.17)$$

where A_i are matrices whose entries are rational numbers, and W_i are symbol letters (also denoted as α_i above).

With the symbol alphabet known prior to performing loop integrations, one can attempt to compute the amplitude, as well as other observables, using the *symbol bootstrap* strategy. This calculation usually starts with constructing the function space from the symbol letters and imposing the integrability conditions. Given the function space and the collection of leading singularities, one then builds an ansatz for the observable containing a finite number of free parameters. To fix these parameters, one typically uses the known behaviour of the observable in singular kinematic regions. After imposing these physical conditions, all parameters can ideally be determined, yielding a unique result. Following this approach, outstanding progress has been made in bootstrapping scattering amplitudes of planar $\mathcal{N}=4$ sYM theory [55, 58–69], both at the symbol and function level. However, despite these remarkable advances for $\mathcal{N}=4$ sYM, these methods remain largely unexplored for physically realistic theories, such as the theory of the strong interactions.

2.3 Color decomposition and planar limit

For the sake of generality, we consider a gauge theory with an $SU(N_c)$ gauge group. The generators are denoted by T^a and the gauge bosons are referred to as gluons. The scattering amplitudes contain both color, associated with the gauge group, and kinematic structures. At tree-level, we disentangle color and kinematics via the standard color decomposition [111], which takes the following form for n -point gluon scattering

$$A_n^{(0)} = g^{n-2} \sum_{\text{perm } \sigma} \text{Tr}\left(T^{\sigma(a_1 \dots T^{a_n})}\right) A_n^{(0)}(\sigma(1 \dots n)), \quad (2.18)$$

where the summation is over $(n-1)!$ permutations σ of n elements modulo cyclic shifts and $A_n^{(0)}$ are called the color-ordered partial amplitudes. The latter are given by the PT factors (2.5) in the MHV helicity case.

The tree-level amplitudes involve only single-trace terms. Starting from one-loop, multi-trace color structures contribute. However, they are suppressed in the large N_c approximation. For example, a one-loop gluonic amplitude in the notation of [111]

$$A_n^{(1)} = g^n \left[\sum_{\sigma} N_c \text{Tr}\left(T^{\sigma(a_1 \dots T^{a_n})}\right) A_{n;1}^{(1)} + \sum_c \sum_{\sigma} \text{Tr}\left(T^{\sigma[1 \dots T^{(c-1)}]}\right) \text{Tr}\left(T^{\sigma[c \dots T^n]}\right) A_{n;c}^{(1)} \right]. \quad (2.19)$$

In the previous expression, in the large N_c limit at fixed 't Hooft coupling $\lambda = g^2 N_c$, the double-trace contributions are suppressed relative to the single-trace contributions. Only Feynman integrals of planar topology contribute in this limit, motivating the term planar limit. Similarly, in the planar limit at L -loop order, only single-trace contributions survive,

$$A_n^{(L)} = g^{n-2+2L} \left[\sum_{\sigma} N_c^L \text{Tr}\left(T^{\sigma(a_1 \dots T^{a_n})}\right) A_{n;1}^{(L)} + \text{subleading} \right]. \quad (2.20)$$

The corresponding partial amplitudes $A_{n;1}^{(L)}$ are called the leading-color partial amplitudes.

For gluon scattering in QCD, it is necessary to include contributions with quarks running in the loops. The quarks are fermions in the fundamental representation of $SU(N_c)$, and there are N_f quark flavors. To extract the planar quark contributions, we take both N_f and N_c to be large, with the ratio N_f/N_c held fixed and finite,

$$\text{planar limit : } N_c \rightarrow \infty, \quad \lambda = g^2 N_c = \text{fixed}, \quad N_f/N_c = \text{fixed}. \quad (2.21)$$

For example, in the planar limit, the two-loop partial amplitudes receive contributions from both gluons and quarks running in the loops in the form of the following expansion

$$A_{n;1}^{(2)} = A_{n;1}^{[1]} + \left(\frac{N_f}{N_c}\right) A_{n;1}^{[\frac{1}{2}]} + \left(\frac{N_f}{N_c}\right)^2 A_{n;1}^{[\frac{1}{2}, \frac{1}{2}]} . \quad (2.22)$$

All partial amplitudes in the previous equation are understood to be at two-loop order. $A_{n;1}^{[1]}$ is the contribution from gluons circulating in both loops, which corresponds to the pure YM theory. $A_{n;1}^{[\frac{1}{2}]}$ denotes the contribution from diagrams involving a single quark loop

and a single gluon loop, and $A_{n;1}^{[\frac{1}{2}, \frac{1}{2}]}$ corresponds to quarks running in both loops. Note that there is a subtlety in the on-shell diagrams that one has to take into account in the planar limit. Namely, not all on-shell diagrams with a quark loop contribute to the N_f/N_c -term. We will comment on this below when discussing relevant leading singularities in Section 4.3.

2.4 IR subtraction, UV renormalisation and hard function

Two-loop color-ordered amplitudes contain IR poles up to the fourth order in the dimensional regulator ϵ , where $D = 4 - 2\epsilon$. Since we assign transcendental weight -1 to ϵ , the maximally-transcendental part of the two-loop n -point amplitude is given schematically by the following sum

$$A_n^{(2)} = \sum_{\ell=0}^2 \frac{1}{\epsilon^{2\ell}} f_n^{(4-2\ell)} + \mathcal{O}(\epsilon), \quad (2.23)$$

where $f_n^{(w)}$ is a function (which is not pure) of transcendental weight w .

The infrared structure of gauge theory amplitudes is well-understood [112–115]. Their IR poles exponentiate, and this exponentiation is governed by the cusp [116, 117] and collinear [118] anomalous dimensions. Consequently, the IR divergences of the amplitudes have a universal form and can be systematically subtracted. This generic treatment of IR divergences considerably simplifies in our calculation set up, because we

- consider the planar limit,
- keep only the maximally-transcendental terms,
- and omit transcendental constants.

Thus, we can rely on the dipole formula to implement the IR subtraction of the amplitudes [119]. Moreover, we can ignore the collinear anomalous dimension and retain only the leading order expression for the cusp anomalous dimension. Thus, at one-loop order, we choose the IR subtraction function

$$I_n^{(1)} = -\frac{1}{\epsilon^2} \sum_{i=1}^n \left(-\frac{s_{i,i+1}}{\mu^2} \right)^{-\epsilon}. \quad (2.24)$$

Working at the symbol level and retaining only the maximally-transcendental contributions, the two-loop IR subtraction can be simplified to (cf. [120])

$$I_n^{(2)} \longrightarrow -\frac{1}{2} \left(I_n^{(1)} \right)^2. \quad (2.25)$$

In addition to IR divergences, loop integrations also generate UV divergences. These are typically eliminated by expressing the bare coupling in terms of the renormalized coupling. Diagrammatically, UV divergences of scattering amplitudes are always contributed by bubble-counting integrals, which always leads to weight-drop after integration due to the double-pole at $\ell \rightarrow \infty$. Since we focus on the leading transcendentality part, UV poles can be safely ignored in the present analysis. Accordingly, g denotes the renormalized coupling.

Using this subtraction scheme, we then define the finite parts, so-called *hard functions*, of the amplitudes as

$$H_n^{(L)} = \lim_{\epsilon \rightarrow 0} \left(A_n^{(L)} - \sum_{\ell=1}^L A_n^{(L-\ell)} I_n^{(\ell)} \right). \quad (2.26)$$

Usually, loop integrations in dimensional regularization introduce explicit dependence on the renormalization mass scale μ^2 in the form of powers of $\log(\mu^2)$. With our choice of the IR subtraction scheme, the maximally-transcendental parts of hard functions $H_n^{(L)}$ contain no explicit dependence of this mass scale, and thus they are well-defined in four dimensions.

Finally, the two-loop QCD hard functions allow for the following decomposition in the planar limit (2.21),

$$H_n^{(2)} = H_n^{[1],(2)} + \left(\frac{N_f}{N_c} \right) H_n^{[\frac{1}{2}],(2)} + \left(\frac{N_f}{N_c} \right)^2 H_n^{[\frac{1}{2},\frac{1}{2}],(2)}, \quad (2.27)$$

which is analogous to (2.22). In this work, we consider gluonic amplitudes in QCD. The term $H_n^{[1]}$ in (2.27) corresponds to the pure YM theory, while the second $H_n^{[\frac{1}{2}]}$ and third $H_n^{[\frac{1}{2},\frac{1}{2}]}$ terms originate from Feynman diagrams with quark loops. Since in the following sections we mainly discuss the details of pure YM amplitudes, if we omit the $[k]$ superscript in an expression, it should be understood that we are referring to the results for the pure YM hard function, $H_n^{[1],(L)}$.

We must also specify the helicity of the scattered particles. Our primary interest in the present work is six-gluon scattering amplitudes in the MHV helicity configuration, which involve two negative helicity gluons. There are 15 distinct ways to assign negative helicity to a pair of gluons among the six. Fortunately, the corresponding helicity amplitudes are not all independent. There are three inequivalent MHV helicity configurations,

$$1^-2^-3^+4^+5^+6^+, \quad 1^-2^+3^-4^+5^+6^+, \quad 1^-2^+3^+4^-5^+6^+, \quad (2.28)$$

and the remaining MHV configurations are cyclic permutations thereof. Indeed, recall that we consider the planar limit and the leading color structures in (2.20) are invariant under dihedral permutations of the scattered particles. The dihedral transformations $\mathbb{Z}_6 \times \mathbb{Z}_2$ are generated by the cyclic shift $i \rightarrow i + 1$ (assuming $7 \equiv 1$) and reflection $i \rightarrow 7 - i$. Modding out these dihedral symmetries therefore leaves three distinct configurations (2.28). Furthermore, the helicity configurations in (2.28) retain residual dihedral symmetries, which in turn imply dihedral symmetry relations for the six-gluon hard functions,

$$\begin{aligned} H(1^-2^-3^+4^+5^+6^+) &= H(2^-1^-6^+5^+4^+3^+), \\ H(1^-2^+3^-4^+5^+6^+) &= H(3^-2^+1^-6^+5^+4^+), \\ H(1^-2^+3^+4^-5^+6^+) &= H(4^-3^+2^+1^-6^+5^+) = H(4^-5^+6^+1^-2^+3^+) \end{aligned} \quad (2.29)$$

where H stands for L -loop planar $H_6^{(L)}$, as well as individual terms in its N_f -decomposition, see (2.27). We tacitly understand the hard function to refer to the symbol projection of its maximally-transcendental part, so that $H_6^{(L)}$ is a weight- $2L$ symbol.

Transcendental weight	1	2	3	4
# Two-loop six-point symbols	9	59	266	639
# Two-loop five-point one-mass symbols	9	59	263	594
# Genuine two-loop six-point symbols	0	0	3	45
# One-loop six-point symbols	9	26	32	32

Table 1. Dimensions of symbol basis for planar six-point massless Feynman integrals.

2.5 Basis of planar six-point two-loop functions

In this subsection, we summarize the key features of the planar two-loop six-particle Feynman integral function space, which serves as our basis for symbol bootstrap calculation.

A symbol bootstrap calculation typically begins with a given symbol alphabet. It then proceeds by constructing integrable symbols of a given transcendental weight dictated by the loop order. The size of the resulting symbol ansatz is determined by the number of integrable symbols, as briefly outlined in subsection 2.2. In this approach, computational challenges grow rapidly with both the size of the symbol alphabet and the loop order. In the present work, by contrast, we exploit that the amplitudes must lie within the function space of the planar two-loop six-particle Feynman integrals. A similar strategy has been employed in Refs. [121, 122] for bootstrapping two-loop four-point form factors, and more recently in six-point two-loop [92, 97] and five-point three-loop [123] bootstrap computations.

In a series of recent works [85, 86, 124–126], the planar two-loop six-particle Feynman integrals have been computed analytically, and the corresponding space of transcendental functions has been determined. These Feynman integrals satisfy the canonical DE given by (2.16), which are solved in terms of Chen’s iterated integrals. In the first three rows of Table 1, we present the counting of the corresponding symbols up to weight four [85]. Note that two-loop five-point Feynman integrals with one massive leg belong to the same planar two-loop six-point massless integral families. As a result, their symbols span a linear subspace of the six-point symbol space. The dimension of the corresponding quotient space therefore counts the number of genuine six-point two-loop symbols.

At maximal transcendentality, the finite term in the ϵ -expansion of the two-loop amplitude belongs to the 639-dimensional space of weight-four symbols counted in the “two-loop six-point symbols” row of Table 1. However, the two-loop hard functions require a larger symbol space. Specifically, we also have to include the weight-four symbols arising from the subtraction terms $I_6^{(1)} A_6^{(1)}$ and $I_6^{(2)}$. For this purpose, we need to include an extended symbol basis. The latter consists of the weight-four symbol space of the one-loop master integrals, together with cyclically symmetric sums of powers of logarithms $\log(s_{i,i+1})$ and their products with one-loop symbols of weights one through three. The result of counting one-loop symbols (from Ref. [85]) is listed in the “one-loop six-point symbols” row of Table 1. Extending the basis of the two-loop weight-four symbols in this manner, we obtain a total of 712 independent weight-four symbols, which form the basis for our six-gluon hard function ansätze.

When counting the independent symbols in Table 1, we imposed that the external

kinematics is four-dimensional. We identify 167 symbol letters appearing in the 712-dimensional space required for the two-loop hard functions. In the notation of Ref. [85], these symbol letters form a subset of $\{W_1, \dots, W_{289}\}$, which constitutes the complete planar two-loop six-point alphabet in D -dimensional kinematics. Among the 167 letters, 99 letters are parity even, while 68 are parity odd. Of these, 154 letters arise from two-loop five-point Feynman integrals with one massive leg, while 13 letters are genuine six-point letters,

$$\begin{aligned}
W_{100} = & -s_{23}s_{34}s_{56} + s_{23}s_{345}s_{56} - s_{12}s_{45}s_{61} - s_{34}s_{61}s_{123} + s_{12}s_{45}s_{234} + s_{34}s_{123}s_{234} \\
& + s_{61}s_{123}s_{345} - s_{123}s_{234}s_{345}, \\
W_{100+i} = & \tau^i(W_{100}), \quad i = 1, \dots, 5, \\
W_{138} = & \Delta_6 = \langle 12 \rangle [23] \langle 34 \rangle [45] \langle 56 \rangle [61] - [12] \langle 23 \rangle [34] \langle 45 \rangle [56] \langle 61 \rangle, \\
W_{242} = & \frac{s_{12}(s_{234}-s_{45}-s_{61}) + s_{23}(s_{34}+s_{56}-s_{345}) + s_{123}(-s_{34}+s_{61}-s_{234}+s_{345}) - \epsilon(1, 2, 3, 5)}{s_{12}(s_{234}-s_{45}-s_{61}) + s_{23}(s_{34}+s_{56}-s_{345}) + s_{123}(-s_{34}+s_{61}-s_{234}+s_{345}) + \epsilon(1, 2, 3, 5)}, \\
W_{242+i} = & \tau^i(W_{242}), \quad i = 1, \dots, 5,
\end{aligned} \tag{2.30}$$

where τ denotes the cyclic-shift generator, $\tau(p_i) = p_{i+1}$, and the parity-odd Lorentz-invariants are defined through the antisymmetric Levi-Civita tensor as

$$\epsilon(i, j, k, l) := 4i\epsilon_{\mu\nu\rho\sigma}p_i^\mu p_j^\nu p_k^\rho p_l^\sigma, \quad i, j, k, l \in \{1, \dots, 6\}. \tag{2.31}$$

As we will see at the end of our bootstrap calculation, the two-loop hard functions in fact involve a slightly smaller subset of 137 symbol letters.

3 Maximal weight projection

We begin this section by reviewing the basics of the *maximal weight projection* for QCD amplitudes and their hard functions [83], which is a primary focus of this work. We show that the maximally-transcendental part of a hard function naturally admits a decomposition into two contributions: an IR-finite term that is unaffected by IR subtraction, and an IR-subtracted term. This decomposition holds universally for the maximally-transcendental contributions to QCD hard functions of arbitrary helicity and multiplicity. The prefactors appearing in both terms of this decomposition are four-dimensional leading singularities, which are computed by taking maximal residues along closed contours in loop-momentum space. As proposed in Ref. [95], the basis integrals used in generalized unitarity calculations can be chosen more optimally such that their maximal residues are diagonalized on a set of linearly independent maximal-cut contours. This approach was called prescriptive unitarity by the authors. In Refs. [93, 96], the maximal cut contours for all basis integrals contributing to the IR-finite part and unaffected by IR subtractions were classified within this framework. In the present paper, combining insights from prescriptive unitarity and the maximal weight projection of Ref. [83] plays a central role.

3.1 Maximally-transcendental part of hard functions

In this work, we focus exclusively on the maximally-transcendental part of the QCD hard functions. To understand their general structure, let us recall how the maximal weight projection is implemented at the level of individual Feynman integrals, which may be both UV- and IR-divergent. It is understood that these Feynman integrals evaluate to Chen iterated integrals, for which the notion of transcendental weight is well defined. We adopt the algorithm introduced in Ref. [83], which builds on ideas pioneered in Ref. [47] on four-dimensional local integrals that evaluate, upon loop integration, to functions of maximal transcendentality. One starts from the four-dimensional L -loop integrand of a given Feynman integral,

$$\prod_{i=1}^L d^4 \ell_i \mathcal{I}(\ell_i, p_e) , \quad (3.1)$$

and then chooses a convenient parameterization of the loop momenta ℓ_i and identifies all propagator poles. Next, one constructs a basis of L -loop $d \log$ integrands with propagators appearing in the original integrand (3.1). In this parametrization, the basis elements take the form

$$\{\mathcal{I}_j\}_{j=1,\dots,N}, \quad \mathcal{I}_j = \sum_i b_i \bigwedge_{k=1}^{4L} d \log(\alpha_{i,j,k}) , \quad (3.2)$$

where coefficients b_j are rational numbers and $\alpha_{i,j,k}$ are poles of the integrand. By construction, these integrands possess only simple poles. Upon performing loop integrations, they evaluate to pure functions of weight $2L$, which is the maximal transcendental weight attainable at L loops¹.

¹Equivalently, the integrated basis elements can be represented by $2L$ -fold $d \log$ iterated integrals.

The original integrand may contain double poles (and higher) in loop momenta, as is typical for QCD loop integrands. Consequently, it cannot be expanded solely in terms of the $d\log$ basis, which we schematically write as

$$\prod_{i=1}^L d^4\ell_i \mathcal{I}(\ell_i, p_e) = \sum_{j=1}^N R_j \mathcal{I}_j + \text{double pole terms}. \quad (3.3)$$

The terms containing double poles give rise, upon loop integration, to contributions of sub-leading transcendental weight. Since we are interested only in the maximally-transcendental part, these terms can therefore be safely neglected. As a result, the maximal weight projection is implemented directly at the integrand level, without performing any loop integrations, as

$$\mathcal{P}_{\text{MT}} \left[\prod_{i=1}^L d^4\ell_i \mathcal{I}(\ell_i, p_e) \right] = \sum_j R_j \mathcal{I}_j. \quad (3.4)$$

The remaining tasks are to classify the rational prefactors R_j and to perform the loop integrations of the basis integrands \mathcal{I}_j . In what follows, we accomplish both goals without requiring explicit knowledge of the full QCD loop integrand.

For loop integrands of QCD amplitudes, the maximal weight projection admits a further refinement. UV divergences originate from double poles at infinity and are therefore projected out by \mathcal{P}_{MT} . By contrast, IR divergences contribute to the maximally-transcendental part. The infrared structure of QCD amplitudes is well understood and was briefly summarized in subsection 2.4. In particular, the IR poles of an L -loop amplitude factorize into products of lower-loop amplitudes and universal IR-subtraction operators. Consequently, the maximal weight projection of an L -loop QCD amplitude integrand $\mathcal{I}(\ell_i, p_e)$ naturally decomposes into an IR-divergent part and an IR-finite part, as follows,

$$\mathcal{P}_{\text{MT}} \left[\prod_{i=1}^L d^4\ell_i \mathcal{I}(\ell_i, p_e) \right] = \underbrace{\sum_{\ell=0}^{L-1} \sum_{j=1}^{k_\ell} R_j^{(\ell)} \mathcal{I}_{j,\ell}}_{\text{IR-subtraction needed}} + \underbrace{\sum_{k=1}^{k_L} R_k^{(L)} \mathcal{I}_k}_{\text{free from IR-divergence}}, \quad (3.5)$$

where $R_j^{(\ell)}$, with $\ell = 0, \dots, L-1$ and $j = 1, \dots, k_\ell$, denote the k_ℓ independent rational prefactors associated with the ℓ -loop amplitudes, whereas $R_k^{(L)}$ are genuinely L -loop prefactors that appear for the first time in the maximally-transcendental part of the L -loop amplitude. This distinction among the prefactors determines whether the accompanying loop integrals are IR divergent, owing to the universal structure of IR divergences in QCD amplitudes. In particular, the loop integrals accompanying the genuinely L -loop prefactors $R_k^{(L)}$ are unaffected by IR subtraction and are finite and well defined in four dimensions.

As explained in [83], since the basis elements \mathcal{I}_j are $d\log$ forms, the expansion coefficients R_j can be efficiently computed as maximal residues of the integrand. However, a purely four-dimensional analysis may be insufficient for the integrand $\mathcal{I}_{j,\ell}$ whose loop integrations are divergent in four dimensions and therefore require regularization. In dimensional

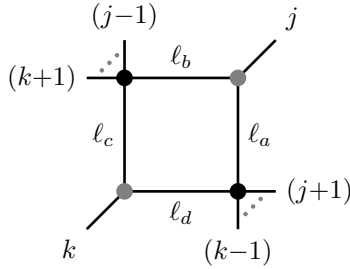


Figure 1. One-loop MHV contour.

regularization with $D = 4 - 2\epsilon$, the $\ell_i^{[-2\epsilon]}$ -components of the loop momenta must be taken into account, and *evanescent terms* may in general be missed by a strictly four-dimensional maximal-residue calculation. By contrast, the IR finite terms in (3.5) are completely characterized by four-dimensional L -loop maximal residues, *i.e.* by L -loop maximal-cut contours. The corresponding prefactors $R_k^{(L)}$ can therefore be computed using standard four-dimensional generalized unitarity methods. In what follows, we first discuss the IR-finite part of the maximal weight projection and then turn to the IR-divergent part.

3.2 IR-finite contributions

To classify the genuinely two-loop leading singularities $R_k^{(2)}$ in (3.5), we need to identify a complete basis of two-loop maximal-cut integration contours that contribute to the IR-finite part, and evaluate the maximal residues along them. According to the general framework of prescriptive unitarity in [95, 96], the IR-finite part receives contributions only from those contours whose maximal residue does not localize the loop momenta to integration regions that generate IR divergences in the amplitudes, *i.e.* collinear regions where $\ell_i \propto p_j$ for certain loop momentum ℓ_i and external momentum p_j [47, 127, 128]. For two-loop MHV gauge-theory amplitudes, such contours have been already fully classified in [93]. We collect all independent maximal-cut contours for MHV amplitudes in pure YM theory at one and two loops in Figures 1 and 2, respectively. In these figures, every edge of a diagram represents placing the corresponding propagator on-shell, while the black and gray vertices impose proportionality relations among the helicity spinors of the momenta flowing into the vertex. A solution to the cut conditions imposed by the on-shell propagators typically has several branches. The chirality of each branch is determined by the coloring of the vertices in the bipartite graph.

At one loop, the only maximal cut with a non-vanishing residue contributing to the IR-finite part is shown in Fig. 1. Let us use this example to illustrate the notation for contour diagrams employed in the figures. The two-mass-easy box maximal-cut imposes the following conditions on the loop momenta:

$$\ell_a^2 = \ell_b^2 = \ell_c^2 = \ell_d^2 = 0. \quad (3.6)$$

Solving these four-dimensional equations, we find two distinct maximal cut solutions,

denoted by $\ell_a^{(1)}$ and $\ell_a^{(2)}$, for the loop momentum ℓ_a ,

$$\left(\ell_a^{(1)}\right)^{\alpha\dot{\beta}} = \frac{\lambda_j^\alpha (p_{j+1,\dots,k-1} \cdot \lambda_k)^{\dot{\beta}}}{\langle jk \rangle}, \quad \left(\ell_a^{(2)}\right)^{\alpha\dot{\beta}} = \frac{(\tilde{\lambda}_k \cdot p_{j+1,\dots,k-1})^\alpha \tilde{\lambda}_j^{\dot{\beta}}}{[jk]}, \quad (3.7)$$

where we have written all spinor-helicity indices explicitly. We see that in the first solution branch $\lambda_{\ell_a} \propto \lambda_j$, whereas in the second branch $\tilde{\lambda}_{\ell_a} \propto \tilde{\lambda}_j$. These two solutions are also commonly referred to as the MHV and $\overline{\text{MHV}}$ branches, respectively. For the MHV amplitude integrand, only the first solution $\ell_a^{(1)}$ yields a non-trivial leading singularity [47, 94]. In Fig. 1, we use gray blobs in these contours to denote the proportionality relations $\lambda_j \propto \lambda_{\ell_a} \propto \lambda_{\ell_b}$ and $\lambda_k \propto \lambda_{\ell_c} \propto \lambda_{\ell_d}$ among the holomorphic helicity spinors attached to the corresponding three-vertices. Neither of the two maximal-cut solutions accesses the collinear region $\ell_a \propto p_j$ or $\ell_c \propto p_k$, indicating that these cuts do not probe soft or collinear regions.

It is worth noting that the contour diagrams shown in Figs. 1 and 2 closely resemble the on-shell diagrams [44], which are discussed in section 4. In fact, on-shell diagrams are in one-to-one correspondence with chiral solutions of maximal cuts. In this work, we deliberately distinguish between these two diagrammatic notations in order to clearly indicate whether we are referring to the on-shell propagator conditions associated with a given contour or to the leading singularities computed by that contour.

At two loops, there are five types of maximal cuts with non-vanishing residues, shown in Fig. 2. When considering QCD amplitudes, one must include the double-box cuts shown in Fig. 2(c), which are absent for amplitude integrands in $\mathcal{N}=4$ sYM (cf. Ref. [93].) This difference is closely related to the fact that $\mathcal{N}=4$ sYM amplitude integrands have vanishing residues at poles at infinity. For QCD amplitudes, by contrast, the double-box cut contours contribute precisely because of non-vanishing residues at poles at infinity. The cuts shown in Figs. 2(d) and 2(e) involve residues taken in a soft region, which set the momentum flowing through the dashed propagator to zero and thereby identify the loop momenta as $\ell_1 = \ell_2$ in the corresponding diagrams². Consequently, two-loop cuts in Figs. 2(d) and 2(e) are equivalent to the one-loop two-mass-easy box cut shown in Fig. 1. In section 4, we present a systematic calculation of the two-loop leading singularities in QCD based on these contours, their associated maximal residues, and the corresponding on-shell diagrams. In section 5, we further show that their accompanying integrands \mathcal{I}_k belong to a class of two-loop Feynman integrals known as prescriptive unitarity integrals. These integrals are IR finite, possess unit leading singularities, and evaluate to pure functions of uniform transcendentality. This structure enables their efficient computation via IBP reduction techniques.

3.3 IR-divergent contributions

Having addressed the IR-finite part of the amplitude in (3.5), we now turn to its IR-divergent contribution. From a four-dimensional perspective, the corresponding prefactors $R_{j,\ell}$ originate from lower-loop leading singularities. For two-loop MHV amplitudes, they are given by

²The cuts in Figs. 2(d) and 2(e) are special planar cases of IR-finite nonplanar cuts, which explains their naming. See Tables III and IV in Ref. [93] for further details.

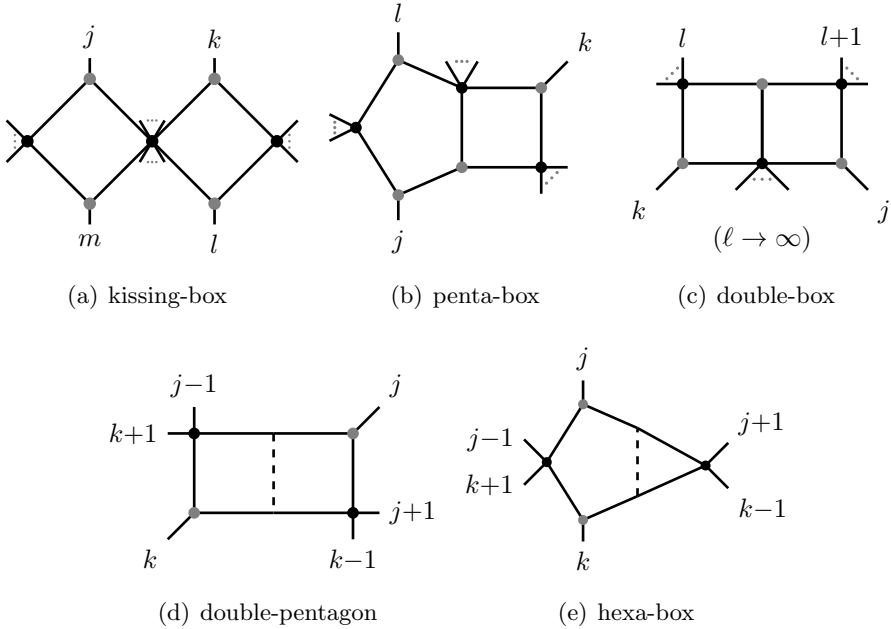


Figure 2. Five types of two-loop contours for MHV amplitudes.

one-loop leading singularities together with the tree-level Parker-Taylor factors (2.5). Since this contribution is IR divergent, it must be treated within dimensional regularization, and the corresponding integrands are therefore defined in $D = 4 - 2\epsilon$ dimensions. Consequently, a naive four-dimensional computation of the associated leading singularities is insufficient in general, and the hard function may receive contributions from evanescent terms. In other words, certain prefactors can be missed by the four-dimensional unitarity. Nevertheless, as discussed in [83], with an appropriate choice of IR-subtraction scheme, one may expect these terms to be artifacts of dimensional regularization that cancel out in the hard function, leaving only four-dimensional information.

In what follows, we adopt a bootstrap strategy to determine the IR-subtracted part, while reserving a tailored basis of prescriptive unitarity integrals for the IR-finite contribution. For each helicity sector, we begin with the tree-level $PT_{n,1i}$ factors and the corresponding one-loop prefactors $R_j^{(1)}$, construct a weight-four symbol ansatz for the accompanying pure transcendental functions, and fix all unknown coefficients by imposing physical constraints. We find that this strategy consistently leads to a unique solution satisfying all known physical requirements and exhibiting the expected analytic structure.

4 Prefactors for MHV QCD amplitudes

Having reviewed the classification of integration contours for IR-finite parts of one-loop and two-loop MHV amplitudes in the previous section, we now turn to the computation of the rational prefactors $R_k^{(\ell)}$ in (3.5). As discussed earlier, these prefactors are closely related to the maximal residues of the integrand and to the leading singularities. The one-loop and two-loop rational prefactors are determined by the maximal cuts shown in Fig. 1 and Fig. 2, respectively. Our calculation employs the formalism of *on-shell diagrams* and *on-shell functions* [48]. This formalism was pioneered in $\mathcal{N}=4$ sYM theory, but it can also be adopted to pure YM and QCD amplitudes.

We begin with a brief review of the basic aspects of on-shell diagrams needed for our discussion. Then we work out one-loop examples as a warm-up for two-loop computations. As discussed in [48, 129], on-shell diagrams giving rise to leading singularities beyond those of $\mathcal{N}=4$ sYM theory exhibit distinctive graphical features. These graphical rules greatly simplify the task of identifying all distinct prefactors of QCD amplitude. Finally, we consider the two-loop MHV QCD amplitudes, presenting a complete set of on-shell diagrams that determine all distinct amplitude prefactors and computing them explicitly. These results provide the foundational input for constructing the ansatz for hard functions in subsequent bootstrap calculations. A more detailed review of on-shell diagrams is presented in Appendix B.

4.1 Non-singlet on-shell diagrams and one-loop prefactors

The unitarity of scattering amplitudes implies that the loop integrand factorizes into simpler and lower-loop objects when certain propagators are put on shell. Putting the maximal allowed number of propagators on shell, thereby freezing all $4L$ degrees of freedom of the loop momenta, defines a maximal cut of the integrand. In this situation, all external and internal momenta are on shell, with the internal momenta localized on the maximal-cut solutions. The resulting factorized building blocks are represented as vertices in on-shell diagrams and correspond to tree-level amplitudes of the theory.

In pure YM theory, on-shell diagrams for MHV amplitudes involve two types of vertices: three-point $\overline{\text{MHV}}$ YM amplitudes $\bar{\mathcal{A}}_3$ and n -point MHV YM amplitudes \mathcal{A}_n . They are given by the PT factor, cf. eq. (2.5),

$$\begin{aligned}
 \text{Diagram: } & \text{Three-point vertex with external lines } a^+, b^+, c^- \text{ and internal loop line } \bar{a}^+ \text{ (arrow pointing up).} \\
 & \bar{\mathcal{A}}_3(a^+, b^+, c^-) = \frac{[ab]^4}{[ab][bc][ca]} \delta^{2 \times 2}(P), \\
 \text{Diagram: } & \text{Three-point vertex with external lines } 1^+, \dots, i^-, \dots, j^-, \dots, n^+ \text{ and internal loop line } \bar{i}^- \text{ (arrow pointing up).} \\
 & \mathcal{A}_n(1^+, \dots, i^-, \dots, j^-, \dots, n^+) = \text{PT}_{n,ij} \delta^{2 \times 2}(P).
 \end{aligned} \tag{4.1}$$

Here, the arrows indicate the helicity of the on-shell particles, and $\delta^{2 \times 2}(P)$ imposes momentum conservation. The resulting on-shell diagrams are bipartite, i.e. built from black and

white vertices sewn together by cut propagators. The three-point MHV and $\overline{\text{MHV}}$ vertices, $\mathcal{A}_3(a, b, c)$ and $\bar{\mathcal{A}}_3(a, b, c)$, play distinct roles in this formalism. They are related by parity conjugation, and complex kinematics is assumed. These vertices impose proportionality constraints on the momenta: for a three-point $\overline{\text{MHV}}$ vertex one has $\lambda_a \propto \lambda_b \propto \lambda_c$, while for a three-point MHV vertex $\tilde{\lambda}_a \propto \tilde{\lambda}_b \propto \tilde{\lambda}_c$.

As a simple example, by calculating the box on-shell diagram we reproduce the four-point PT factor as follows,

$$\begin{array}{c}
\text{Diagram:} \\
\begin{array}{c}
\text{A directed graph with 4 nodes labeled 1, 2, 3, 4.} \\
\text{Nodes 1 and 2 are black, nodes 3 and 4 are white.} \\
\text{Arrows: } 1 \rightarrow 2, 2 \rightarrow 3, 3 \rightarrow 4, 4 \rightarrow 1, 1 \rightarrow 3, 2 \rightarrow 4, 3 \rightarrow 2, 4 \rightarrow 3. \\
\text{Labels: } \ell_1, \ell_2, \ell_3, \ell_4 \text{ are associated with the edges.}
\end{array} \\
= \bar{\mathcal{A}}_3(\ell_1^+, \ell_4^+, 1^-) \bar{\mathcal{A}}_3(3^+, \ell_3^+, \ell_2^-) \mathcal{A}_3(2^-, \ell_1^-, \ell_2^+) \mathcal{A}_3(\ell_3^-, \ell_4^-, 4^+) \\
= \frac{\langle 12 \rangle^4}{\langle 12 \rangle \langle 23 \rangle \langle 34 \rangle \langle 41 \rangle} \delta^{2 \times 2}(P) \quad (4.2)
\end{array}$$

Here, we substitute the maximal-cut solution for the loop momenta flowing through the on-shell propagators,

$$\ell_1 = \frac{\langle 23 \rangle}{\langle 13 \rangle} \lambda_1 \tilde{\lambda}_2, \quad \ell_2 = \frac{\langle 12 \rangle}{\langle 13 \rangle} \lambda_3 \tilde{\lambda}_2, \quad \ell_3 = \frac{\langle 14 \rangle}{\langle 13 \rangle} \lambda_3 \tilde{\lambda}_4, \quad \ell_4 = \frac{\langle 34 \rangle}{\langle 13 \rangle} \lambda_1 \tilde{\lambda}_4. \quad (4.3)$$

We conclude that $\text{PT}_{4,12}$, see (2.5), is a one-loop leading singularity of the four-point pure YM amplitude in the helicity configuration $(1^-2^-3^+4^+)$. The three-point vertices in a bipartite on-shell diagram impose proportionality relations on the momenta. In the present example,

$$\lambda_1 \propto \lambda_{\ell_1} \propto \lambda_{\ell_4}, \quad \tilde{\lambda}_2 \propto \tilde{\lambda}_{\ell_1} \propto \tilde{\lambda}_{\ell_2}, \quad \lambda_3 \propto \lambda_{\ell_2} \propto \lambda_{\ell_3}, \quad \tilde{\lambda}_4 \propto \tilde{\lambda}_{\ell_3} \propto \tilde{\lambda}_{\ell_4}. \quad (4.4)$$

As a result, a bipartite graph also specifies the chirality of the corresponding maximal cut solution. This is the basic logic of Ref. [48] for classifying the leading singularities of gauge theory amplitudes at a given loop order. More details of this method are provided in Appendix B.

Several points are worth noting here. First, when focusing on a specific helicity sector and an on-shell diagram of fixed topology, the helicities of the external legs constrain the helicity assignments of the internal lines. Diagrammatically, this restricts the allowed bipartite colorings of the on-shell diagram. For example, a box on-shell diagram in the MHV helicity sector can never contain a next-to-MHV (NMHV) corner. This is because the required helicity distribution would necessarily force another corner to be single-minus, which gives a vanishing residue at one loop. From a combinatorial perspective, this implies that any admissible maximal cut contributing to MHV amplitudes necessarily exhibits MHV helicity counting. At one loop, any box MHV on-shell diagram necessarily consists of two MHV and two $\overline{\text{MHV}}$ tree-level amplitudes.

Second, it is crucial to keep track of the helicity of the internal states, which are indicated by arrows on the on-shell propagators. When computing the leading singularity

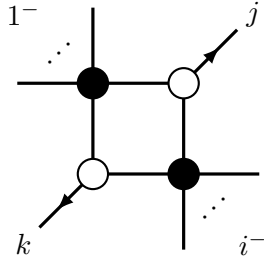


Figure 3. Non-singlet two-mass-easy box on-shell diagrams contributing genuinely one-loop prefactors.

associated with a given maximal cut, one must sum over all possible helicity assignments flowing through the on-shell diagram. As a result, it becomes clear how one-loop leading singularities beyond PT factors arise from on-shell diagrams. For the diagram in eq. (4.2), the helicity assignment of the internal lines is fixed uniquely by the helicity configuration of the external gluons and by the chirality of the three-point vertices. However, “*non-singlet*” on-shell diagrams contribute for certain other helicity configurations of the external gluons [48, 129, 130],

$$\begin{array}{c} 2^+ \quad \quad \quad 3^- \\ \diagdown \quad \quad \quad \diagup \\ \text{---} \quad \quad \quad \text{---} \\ \diagup \quad \quad \quad \diagdown \\ 1^- \quad \quad \quad 4^+ \end{array} = \begin{array}{c} 2^+ \quad \quad \quad 3^- \\ \diagdown \quad \quad \quad \diagup \\ \text{---} \quad \quad \quad \text{---} \\ \diagup \quad \quad \quad \diagdown \\ 1^- \quad \quad \quad 4^+ \end{array} + \begin{array}{c} 2^+ \quad \quad \quad 3^- \\ \diagup \quad \quad \quad \diagdown \\ \text{---} \quad \quad \quad \text{---} \\ \diagdown \quad \quad \quad \diagup \\ 1^- \quad \quad \quad 4^+ \end{array} \quad (4.5)$$

In this example, a gluon on-shell state circulates inside the loop. There are two possible helicity assignments, corresponding to the two possible orientations of the loop. In $\mathcal{N} = 4$ sYM theory, however, the entire vector on-shell supermultiplet circulates in the loop of these on-shell diagrams, rather than only the gluon. This leads to a discrepancy between the corresponding expressions for the leading singularities in pure YM and $\mathcal{N} = 4$ sYM theories.

Sewing the three-point amplitudes evaluated on the maximal cut solutions, we obtain the following leading singularity,

$$\begin{array}{c} 2^+ \quad \quad \quad 3^- \\ \diagdown \quad \quad \quad \diagup \\ \text{---} \quad \quad \quad \text{---} \\ \diagup \quad \quad \quad \diagdown \\ 1^- \quad \quad \quad 4^+ \end{array} = \text{PT}_{4,13} \times \left[\left(\frac{\langle 12 \rangle \langle 34 \rangle}{\langle 13 \rangle \langle 24 \rangle} \right)^4 + \left(\frac{\langle 14 \rangle \langle 23 \rangle}{\langle 13 \rangle \langle 24 \rangle} \right)^4 \right]. \quad (4.6)$$

In the $\mathcal{N} = 4$ sYM case, this on-shell diagram evaluates to the supersymmetric PT factor, in agreement with the general statement that MHV leading singularities at any loop order in this theory are PT factors [32, 48]. In contrast, in pure YM theory the leading singularity

(4.6) appears as a rational prefactor (together with the PT factor $\text{PT}_{4,13}$, owing to IR subtractions) in the maximally-transcendental part of the one-loop hard function for the helicity configuration $(1^-2^+3^-4^+)$.

The previous expression is readily extended to the n -point one-loop MHV case. In this setting, all leading singularities beyond the PT factors arise from the two-mass-easy box type on-shell diagrams in Fig. 3. The two negative helicity legs, 1^- and i^- , are placed in the separate MHV corners, and two possible orientations of the gluon circulating in the loop give rise to the following leading singularity,

$$R_{1i,jk,n}^{(1)} = \text{PT}_{n,1i} \times \left[\left(\frac{\langle 1j \rangle \langle ik \rangle}{\langle jk \rangle \langle 1i \rangle} \right)^4 + \left(\frac{\langle 1k \rangle \langle ij \rangle}{\langle jk \rangle \langle 1i \rangle} \right)^4 \right], \quad 1 < j < i < k \leq n. \quad (4.7)$$

This leading singularity contributes only for helicity configurations satisfying $i-1 \geq 2$, i.e. legs 1^- and i^- are nonadjacent. Consequently, the maximally-transcendental parts of the one-loop n -point MHV split-helicity hard functions $H_{-+...+}^{(1)}$ are pure functions, normalized by the PT factor. This observation is in agreement with the explicit expressions for the one-loop pure YM hard functions available in the literature.

In the following sections, we will see that MHV leading singularities beyond the PT factors always arise from non-singlet on-shell diagrams. This observation provides a guiding principle for classifying the prefactors in the hard function ansatz.

As a final comment, note that the on-shell diagrams are built from conformally-invariant tree-level amplitudes, which are sewn together in a conformally invariant manner. As a result, the corresponding leading singularities are conformally invariant and are therefore annihilated by the conformal boost generator [40, 84],

$$k_{\alpha\dot{\alpha}} = \sum_{i=1}^n \frac{\partial}{\partial \lambda_i^\alpha} \frac{\partial}{\partial \tilde{\lambda}_i^{\dot{\alpha}}}. \quad (4.8)$$

In fact, this annihilation is trivial for MHV leading singularities considered in this work, since the latter involve only angular spinor-helicity brackets $\langle \lambda_a \lambda_b \rangle$. One can see it explicitly for the one-loop leading singularity given in eq. (4.7), as well as for all two-loop MHV leading singularities, which we compute explicitly below. Let us also note that the conformal invariance of NMHV (and higher-helicity) leading singularities, which involve both λ and $\tilde{\lambda}$ helicity spinors, is nontrivial.

4.2 Two-loop MHV prefactors for pure YM amplitudes

We next analyze the two-loop MHV leading singularities. As discussed in section 3, when considering the maximal weight projection of the MHV amplitudes, the relevant contours for computing two-loop four-dimensional maximal cuts are the kissing-box, double-box, and penta-box cut, shown in Fig. 2. Thus, it suffices to study these on-shell diagrams. By enumerating all possible helicity assignments on the external legs and internal lines, one finds that genuinely new two-loop leading singularities, beyond both PT factors and one-loop leading singularities, arise from on-shell diagrams containing exactly two oriented

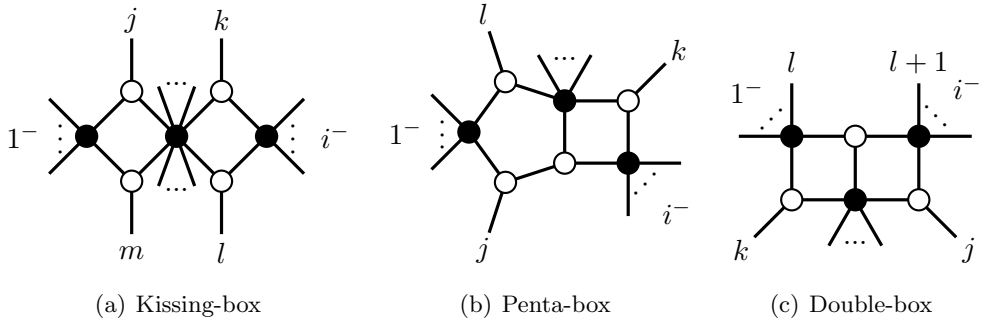
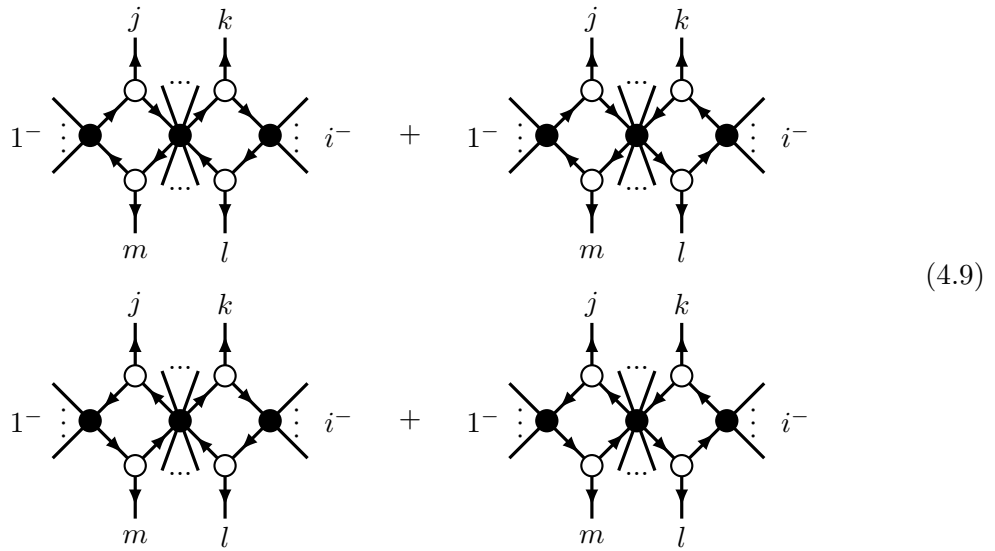


Figure 4. Non-singlet on-shell diagrams contributing to genuinely two-loops prefactors.

cycles of helicity flow. We also find that the pair of negative-helicity legs must be chosen as shown in Fig. 4. Note that, since the massless positive-helicity corners are present in these on-shell diagrams, the kissing-box cut contributes only starting from six points and for $i - 1 \geq 3$, while the penta-box cut contributes only starting from five points and for $i - 1 \geq 2$. By contrast, the double-box cut contributes starting from four points and in all MHV sectors.

We further compute all genuinely new two-loop leading singularities for pure YM MHV amplitudes at arbitrary multiplicity, which are represented by on-shell diagrams in Fig. 4. The kissing-box on-shell diagrams are readily evaluated by sewing together seven tree-level amplitudes that constitute them. For each facet of the kissing-box on-shell diagram, there are two possible helicity assignments, which form oriented cycles of the helicity flow,



Substituting the maximal cut solutions for the eight on-shell propagators (which coincide with those of the one-loop two-mass-easy box) into the MHV and $\overline{\text{MHV}}$ vertices of the on-shell diagrams, we obtain the following expression for the sum of four on-shell diagrams in (4.9),

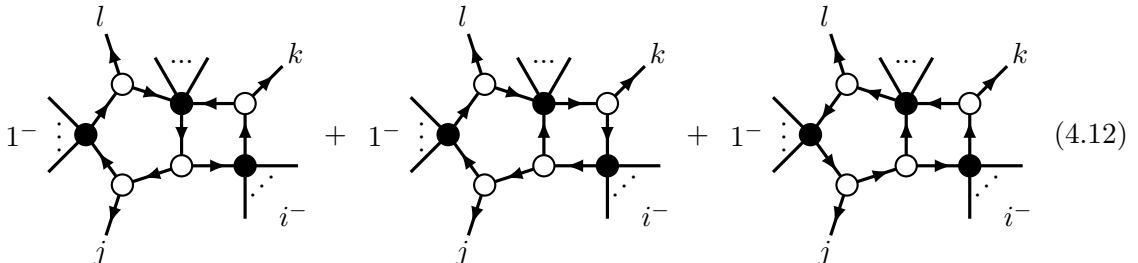
$$R_{1i,jklm,n}^{(2),\text{kb}} := \text{PT}_{n,1i} \times \left[\left(\frac{\langle 1j \rangle \langle ki \rangle \langle ml \rangle}{\langle 1i \rangle \langle jm \rangle \langle kl \rangle} \right)^4 + \left(\frac{\langle 1j \rangle \langle il \rangle \langle km \rangle}{\langle 1i \rangle \langle jm \rangle \langle kl \rangle} \right)^4 + \left(\frac{\langle 1m \rangle \langle ki \rangle \langle jl \rangle}{\langle 1i \rangle \langle jm \rangle \langle kl \rangle} \right)^4 + \left(\frac{\langle 1m \rangle \langle il \rangle \langle jk \rangle}{\langle 1i \rangle \langle jm \rangle \langle kl \rangle} \right)^4 \right],$$

$$1 < j < k < i < l < m \leq n . \quad (4.10)$$

The calculation for the penta-box cut proceeds analogously. Putting eight propagators on shell completely freezes the loop momenta. In spinor-helicity notations, these eight on-shell internal states carry the momenta (see (5.10) for the definition of the loop momenta)

$$\begin{aligned} \ell_a &= \frac{\lambda_j(P_{l+1,\dots,j-1} \cdot \lambda_l)}{\langle jk \rangle}, \quad \ell_b = \frac{\lambda_j(P_{j+1,\dots,l-1} \cdot \lambda_l)}{\langle jk \rangle}, \quad \ell_c = \frac{\lambda_l(P_{j+1,\dots,l-1} \cdot \lambda_j)}{\langle jk \rangle}, \\ \ell_d &= \frac{\lambda_l(P_{l+1,\dots,j-1} \cdot \lambda_j)}{\langle jk \rangle}, \quad \ell_e = \frac{\lambda_k(P_{l+1,\dots,k-1} + \ell_d) \cdot \lambda_a}{\langle ak \rangle}, \quad \ell_f = \frac{\lambda_k(P_{k+1,\dots,j-1} \cdot \lambda_a)}{\langle ak \rangle}, \\ \ell_g &= \frac{\lambda_a(P_{k+1,\dots,j-1} + \ell_k)}{\langle ak \rangle}, \quad \ell_h = \frac{\lambda_a(P_{l+1,\dots,k-1} + \ell_d) \cdot \lambda_k}{\langle ak \rangle}, \end{aligned} \quad (4.11)$$

where $\lambda_a := \lambda_{\ell_a}$ and $P_{i,\dots,j} := p_i + p_{i+1} + \dots + p_j$. By sewing the vertices of the on-shell diagram, we identify three possible cyclically oriented helicity assignments: either both facets of the graph carry an oriented cycle, or only one of the two facets carries an oriented cycle while the other oriented cycle flows through the larger loop, as depicted in eq. (4.12).



Using the maximal cut solutions (4.11) to evaluate the three on-shell diagrams, we finally obtain,

$$R_{1i,jkl,n}^{(2),\text{pb}} := \text{PT}_{n,1i} \times \left[\left(\frac{\langle 1j \rangle \langle ij \rangle \langle kl \rangle}{\langle 1i \rangle \langle jl \rangle \langle jk \rangle} \right)^4 + \left(\frac{\langle 1l \rangle \langle ij \rangle}{\langle 1i \rangle \langle jl \rangle} \right)^4 + \left(\frac{\langle 1j \rangle \langle ik \rangle}{\langle 1i \rangle \langle jk \rangle} \right)^4 \right]. \quad (4.13)$$

$$1 < j < i < k < l \leq n \quad \cup \quad 1 < l < k < i < j \leq n$$

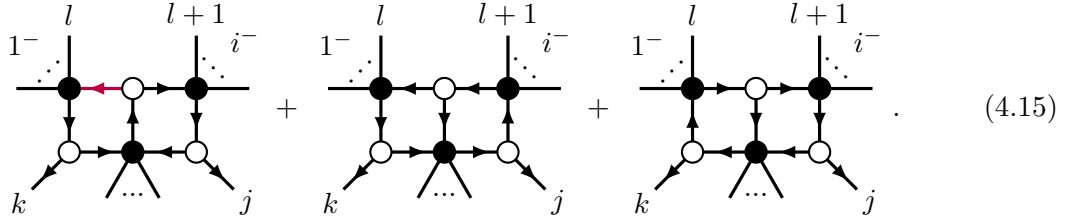
We would like to draw the reader's attention to the fact that this penta-box diagram is not invariant under reflection. As a result, clockwise and counterclockwise orderings of the external legs give rise to the two allowed ranges of j, k, l in the expression above. However, once the planarity ordering condition on the external legs is imposed, the arrangement of the three legs j, k, l effectively determines the positions of all other external legs. Hence, in

what follows, we simply use the ordered triple of indices $jk\ell$ as subscripts to specify the positions of external legs.

Notably, the sum of three terms inside the square brackets is symmetric under the exchange $1 \leftrightarrow i$ and $l \leftrightarrow k$. Therefore, this leading singularity is invariant under reflection symmetry, and it is always given by the sum of two distinct penta-box maximal cuts, i.e.

$$R_{1i,jkl,n}^{(2),\text{pb}} = R_{i1,jlk,n}^{(2),\text{pb}}. \quad (4.14)$$

The double-box on-shell diagrams are more subtle to compute, since the on-shell constraints imposed by their seven propagators do not completely localize the loop momenta. The leading singularities arising from this type of on-shell diagram are called *composite*. They originate from poles of the integrand at $\ell \rightarrow \infty$ and are extracted by choosing integration contours that evaluate the maximal residues in a loop-by-loop manner. We identify three distinct helicity assignments for the internal lines of the double-box that contain exactly two oriented cycles of helicity flow:



Solving the cut conditions for seven on-shell propagators, we obtain the following one-form expression for the sum of the three on-shell diagrams,

$$\begin{aligned} \Omega_{1i,jkl,n}^{(2)\text{db}} = & \text{PT}_{n,1i} \times \frac{\langle ll+1\rangle \langle k\ell(z)\rangle^2 dz}{\langle 1i\rangle^4 \langle l\ell(z)\rangle \langle l+1\ell(z)\rangle} \quad 1 \leq l < i < j < k \leq n, \\ & \times \left[\langle kj\rangle^4 \left(\frac{\langle 1\ell(z)\rangle \langle i\ell(z)\rangle}{\langle j\ell(z)\rangle \langle k\ell(z)\rangle} \right)^4 + \langle ij\rangle^4 \left(\frac{\langle 1\ell(z)\rangle}{\langle j\ell(z)\rangle} \right)^4 + \langle 1k\rangle^4 \left(\frac{\langle i\ell(z)\rangle}{\langle k\ell(z)\rangle} \right)^4 \right], \end{aligned} \quad (4.16)$$

where the variable z parametrizes the loop momentum

$$(\ell(z))^{\alpha\dot{\alpha}} = \left(z|k\rangle - \frac{P|k\rangle}{\langle k|P|k\rangle} \right)^\alpha (\langle k|P)^{\dot{\alpha}}, \quad (4.17)$$

flowing through the upper horizontal edge of left box subdiagram (colored in the first diagram) and $P := p_{k+1} + \dots + p_l$ is the total momentum flowing in the upper-left corner. The genuinely two-loop composite leading singularity is then obtained by taking the residue of this form at $z = \infty$. The general expression of this residue is too lengthy to present here. We denote the resulting invariant by $R_{1i,jkl,n}^{(2),\text{db}}$ in what follows. At six points, their explicit results can be found in the ancillary files.

In summary, all genuinely two-loop prefactors contributing to the maximally-transcendental part of pure YM MHV hard functions at arbitrary multiplicity fall into three classes: $R_{1i,jkl,n}^{(2),\text{kb}}$,

	(--++++)	(-+-+++)	(-++-++)
$L = 1$	1	4	5
$L = 2$	7	13	16

Table 2. Counting of independent prefactors for the maximally-transcendental part of the six-point L -loop pure YM hard functions in the MHV helicity sectors.

$R^{(2),\text{pb}}$, and $R^{(2),\text{db}}$. Together with the one-loop prefactors $R_{1i,jk,n}^{(1)}$ (4.7) and tree-level $\text{PT}_{n,1i}$ (2.5), they form a complete basis of prefactors for our computation of pure YM MHV hard functions. All these prefactors involve only angular spinor-helicity brackets and are therefore manifestly conformally invariant, being annihilated by the conformal boost generator (4.8). In the cases of four- and five-gluon scattering, we have verified that our results are in complete agreement with the prefactors appearing in the corresponding one-loop and two-loop hard functions available in the literature, referring to hard function results in [17, 27]. Moreover, the spinor-helicity representations of the rational prefactors computed in this section provide a substantial simplification compared to the corresponding lower-point expressions written in terms of Mandelstam invariants.

Our previous computations of the prefactors applies to arbitrary multiplicity n . We now specialize to the six-point case. By enumerating all possible distributions of external legs in the on-shell diagrams, we obtain the counting of independent prefactors for the six-point MHV sectors, summarized in Table 2. At six points, there are three inequivalent helicity sectors, see (2.28). There are no genuinely one-loop leading singularities in the sector $(--++++)$. By contrast, the two remaining sectors contain three and four such leading singularities, respectively, arising from the two-mass-easy box cuts. For the $(--++++)$ sector, only double-box on-shell diagrams contribute at two loops, yielding six genuinely two-loop leading singularities,

$$R_{12,ij1,6}^{(2),\text{db}} = \text{PT}_{6,12} \times \left[-2 + 12 \frac{\langle 1i \rangle \langle 2j \rangle}{\langle 12 \rangle \langle ij \rangle} - 30 \left(\frac{\langle 1i \rangle \langle 2j \rangle}{\langle 12 \rangle \langle ij \rangle} \right)^2 + 20 \left(\frac{\langle 1i \rangle \langle 2j \rangle}{\langle 12 \rangle \langle ij \rangle} \right)^3 \right], \quad (4.18)$$

with $2 < i < j \leq 6$. They featured in the two-loop bootstrap of Ref. [92]³. More types of two-loop on-shell diagrams contribute in the remaining two sectors. For the sector $(-+-+++)$, there is one PT-factor, three two-mass-easy box prefactors, six double-box prefactors, and three penta-box prefactors. By contrast, for the $(-++-++)$ sector, there is one PT-factor, four two-mass-easy box prefactors, six double-box prefactors, one kissing-box prefactors, and four penta-box prefactors.⁴ The corresponding on-shell diagrams are shown in Fig. 5 and Fig. 6.

Note that IR-divergent MHV amplitudes may involve a larger set of prefactors as compared to the IR-finite hard functions. For example, the maximally-transcendental part of the one-loop five-point pure YM amplitude in the split-helicity configuration $(--++ +)$

³Note that (4.18) differ from the leading singularities $R_{i,j}$ defined in [92] by a PT term.

⁴Note that for each penta-box on-shell diagrams, its reflection generates the same leading singularity. We only count and show independent ones in Fig. 5 and Fig. 6.

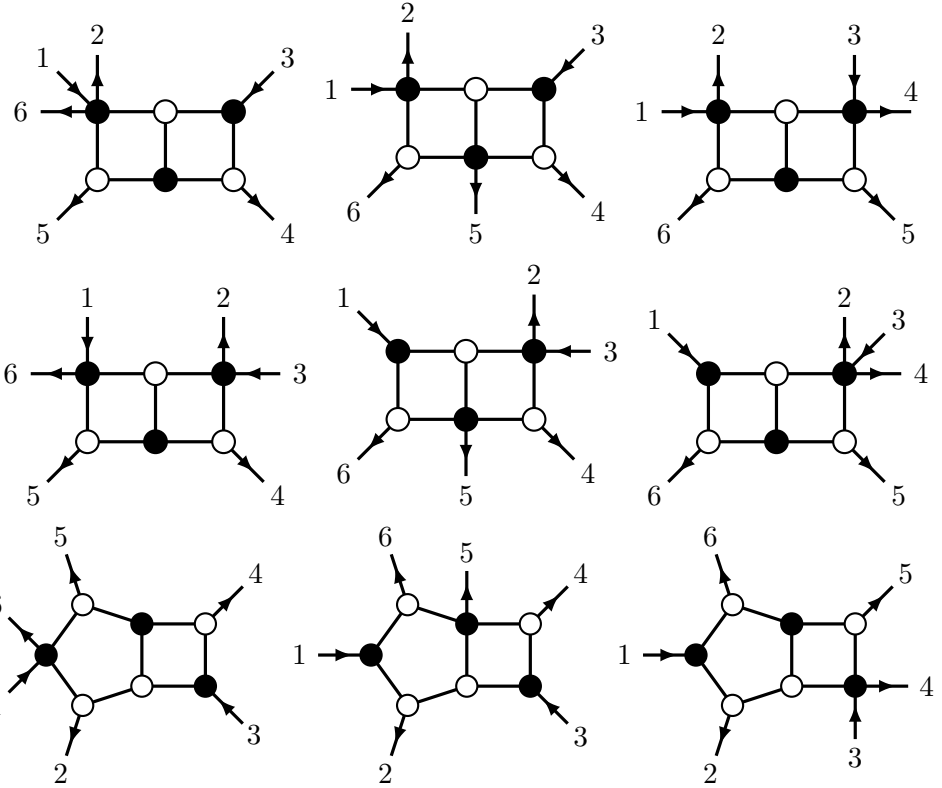


Figure 5. Two-loop on-shell diagrams for the MHV sector $(-+---+)$.

contains an additional prefactor at order $\mathcal{O}(\epsilon)$, see Ref. [27],

$$R_{\star}^{(1)} = \text{PT}_{6,12} \times \left(1 - \frac{4s_{15}s_{23}s_{34}s_{45}}{\text{tr}_5^2} + \frac{2s_{15}^2s_{23}^2s_{34}^2s_{45}^2}{\text{tr}_5^4} \right), \quad (4.19)$$

where $\text{tr}_5 := 4i\epsilon_{1234}$. This amplitude prefactor is not conformally-invariant and therefore cannot be captured by four-dimensional on-shell diagrams. Detecting it would instead require a D -dimensional leading singularity analysis, see [4, 131–133]. Furthermore, the corresponding two-loop five-point amplitude also involves $R_{\star}^{(1)}$ at order $\mathcal{O}(\epsilon^0)$. However, upon implementing the two-loop IR subtraction [119], one finds that $R_{\star}^{(1)}$ cancels out from the four-dimensional hard function. Its maximally-transcendental part involves only the conformally-invariant prefactors computed from on-shell diagrams.

4.3 Two-loop MHV prefactors for QCD amplitudes

The above computation of leading singularities straightforwardly extends to two-loop MHV amplitudes in QCD, requiring only minor modifications. The sole adjustment is the inclusion of tree-level amplitudes with both gluonic and fermionic legs as vertices in the on-shell diagrams. For instance, the basic building blocks involving a single quark-antiquark pair

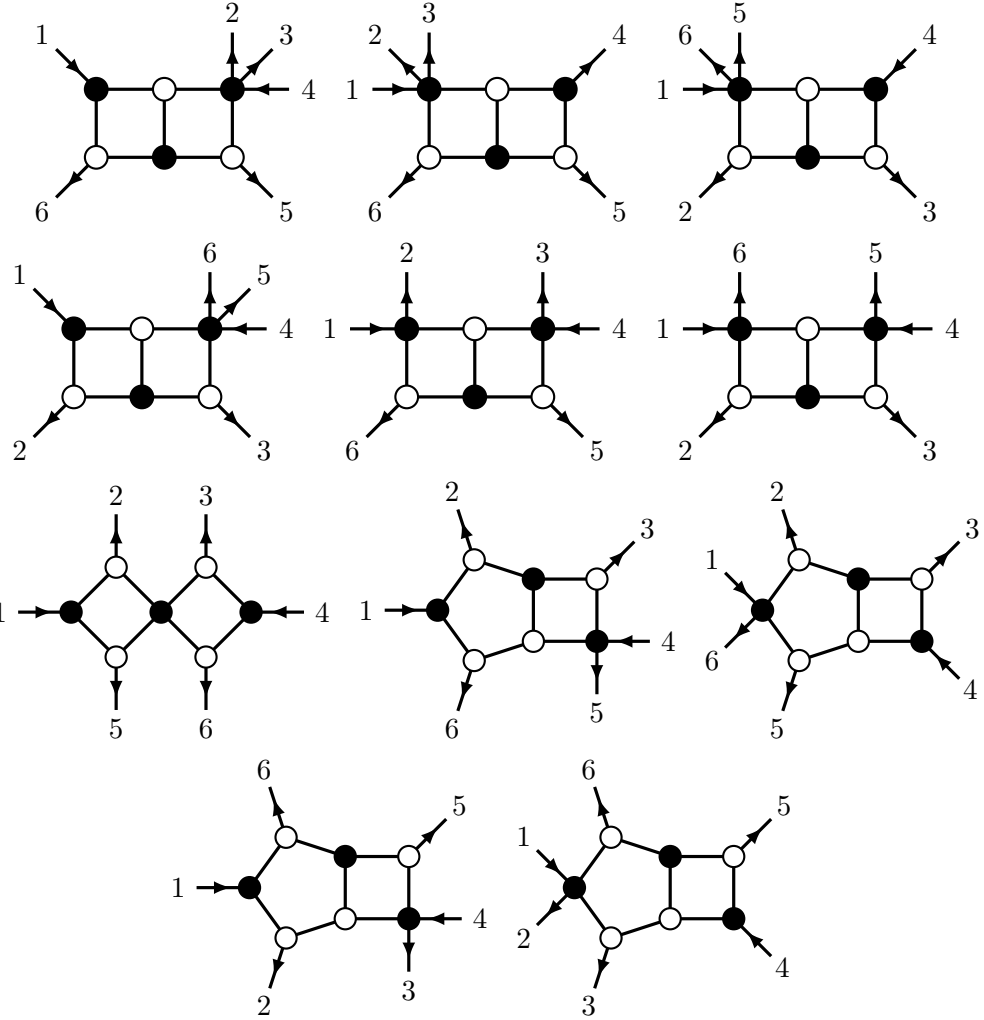


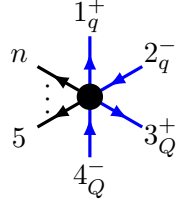
Figure 6. Two-loop on-shell diagrams for the MHV sector $(-+--++)$.

are given by the following tree-level amplitudes,

$$\begin{aligned}
 & \text{Diagram 1: } \bar{A}_3(a_g^+, b_q^+, c_q^-) = \frac{[ab]^3[ac]}{[ab][bc][ca]} \delta^{2 \times 2}(P) \\
 & \text{Diagram 2: } \mathcal{A}_n(1_q^+, 2_q^-, 3_g^+, \dots, i_g^-, \dots, n_g^+) = \frac{\langle 2i \rangle^3 \langle 1i \rangle}{\langle 12 \rangle \dots \langle n1 \rangle} \delta^{2 \times 2}(P)
 \end{aligned} \tag{4.20}$$

We represent quarks by blue lines, while thick black lines continue to denote gluons, and we also refer to the second expression as PT factors for tree-level QCD amplitudes with a pair

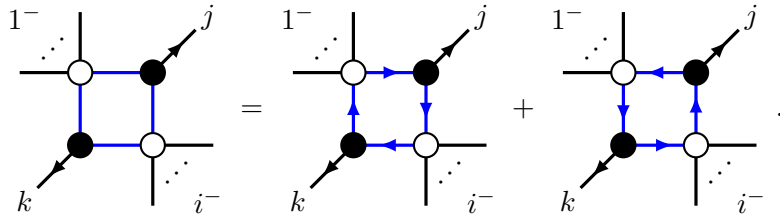
of fermionic external legs. For the N_f^2 contribution of helicity sector $(-+-+-+)$, we also need MHV tree-level amplitudes with two quark-antiquark pairs, which take the form



$$: \mathcal{A}_n(1_q^+, 2_q^-, 3_Q^+, 4_Q^-, \dots, n_g^+) = \frac{\langle 24 \rangle^3 \langle 13 \rangle}{\langle 12 \rangle \dots \langle n1 \rangle} \delta^{2 \times 2}(P) \quad (4.21)$$

For simplicity, we do not distinguish between different quark flavors in our diagrammatic notations. In what follows, we discuss leading singularities arising from N_f - and N_f^2 -contributions, which distinguish QCD from pure YM.

Tree-level gluon amplitudes are independent of quark content, while N_f -terms of gluonic amplitudes first arise at one loop. At one loop, the corresponding prefactors originate from non-singlet on-shell diagrams containing a closed cycle of quark lines,



The internal helicity assignment necessarily forms a closed cycle as a consequence of flavor conservation. Accordingly, PT factors are no longer allowed prefactors for N_f -terms. In the helicity sector $(- - + \dots)$, no non-singlet on-shell diagram exists. As a result, the N_f -term of the corresponding one-loop hard function vanishes, $H_{- - + \dots +}^{[1/2], (1)} = 0$, in agreement with the five-point expressions in Ref. [27]. By contrast, the leading singularities in the sector $(1^- 2^+ \dots i^- \dots n^+)$ are obtained by evaluating the on-shell diagrams in eq. (4.22),

$$S_{1i,jk,n}^{(1)} = \text{PT}_{n,1i} \times \left(\frac{\langle 1j \rangle^3 \langle ik \rangle^3 \langle 1k \rangle \langle ij \rangle}{\langle 1i \rangle^4 \langle jk \rangle^4} + \frac{\langle 1k \rangle^3 \langle ij \rangle^3 \langle 1j \rangle \langle ik \rangle}{\langle 1i \rangle^4 \langle jk \rangle^4} \right), \quad (4.23)$$

which contributes in the N_f -term of the hard function starting at one loop for $i - 1 > 1$.

Before proceeding to the two-loop analysis in QCD, we clarify a subtle point concerning on-shell diagrams involving quark lines. Since we work in the planar limit defined by N_c , $N_f \rightarrow \infty$ and fixed ratio N_f/N_c , see (2.21), special care is required in tracking the color and flavor structure of the on-shell diagrams. To this end, we review the double-line notation to determine which contributions survive in the planar limit and which are subleading.

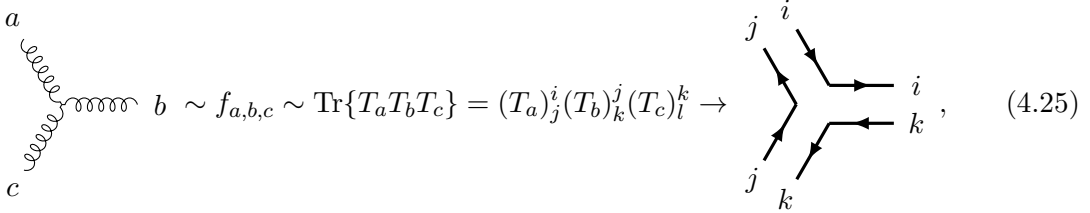
In QCD, there are N_f quarks transforming in the fundamental representation of $SU(N_c)$, while gluons transform in the adjoint representation. Since all N_f quarks interact identically with the gluons, the theory enjoys an additional global $SU(N_f)$ flavor symmetry. Under this symmetry, quarks transform in the fundamental representation, whereas the gluons are singlets, as they are neutral under flavor transformations. Subtleties of the planar limit arise when, in addition to taking $N_c \rightarrow \infty$, one also considers $N_f \sim N_c$. In this case, it is

no longer sufficient to count only the number of loops in a diagram, as the scaling depends on whether the loops are formed by quarks or by gluons.

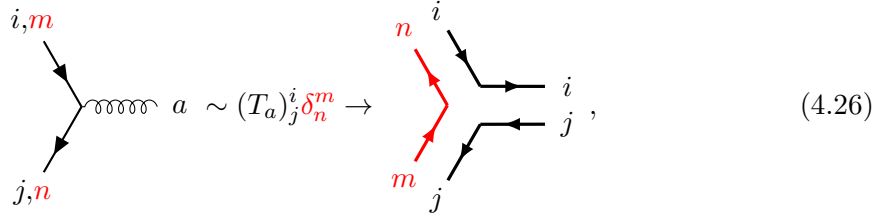
To make this explicit, we employ 't Hooft's double-line notation. In this framework, all color structures are expressed in terms of (anti-)fundamental representations, and lines denote index contractions dictated by the Feynman rules. Moreover, since two symmetry groups are involved— $SU(N_c)$ and $SU(N_f)$ —we use black and red lines to denote indices in the corresponding (anti-)fundamental representations. With this conventions, the gluon and quark propagators are represented as follows

$$a \text{ (wavy line)} b \sim \delta_{a,b} \rightarrow \delta_k^i \delta_j^l = \begin{array}{c} i \xleftarrow{\quad} k \\ j \xrightarrow{\quad} l \end{array}, \quad i, \text{ (red line)} \rightarrow k, \text{ (red line)} \sim \delta_l^i \delta_n^m \rightarrow \begin{array}{c} i \xleftarrow{\quad} j \\ m \xrightarrow{\quad} n \end{array}, \quad (4.24)$$

where i, j, k, l label indices in the (anti-)fundamental representation of $SU(N_c)$, whereas m, n label indices in the (anti-)fundamental of $SU(N_f)$. Following the same graphical convention, in which index contractions are represented by oriented lines connecting the corresponding indices, the three-point gluon vertex is depicted as

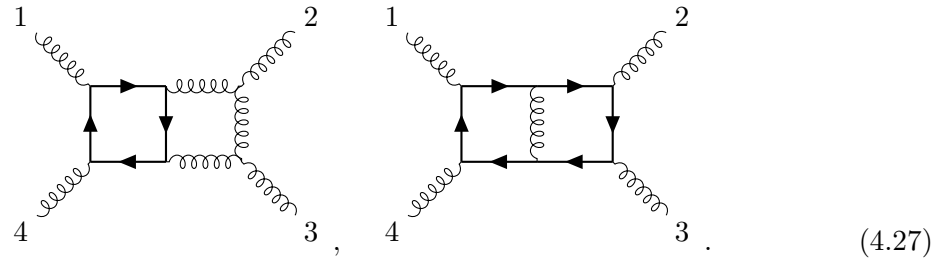


and the three-point quark-gluon interaction vertex as

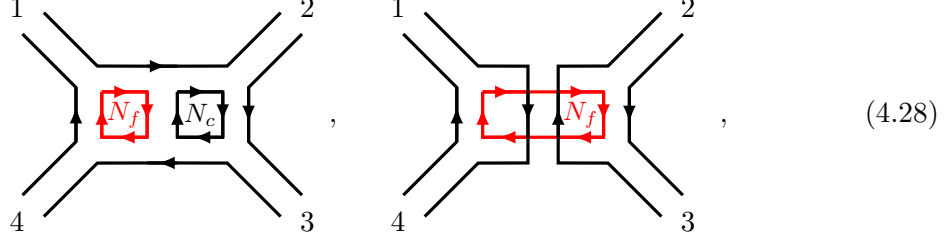


where the contraction of $SU(N_f)$ indices is explicitly indicated by a red line.

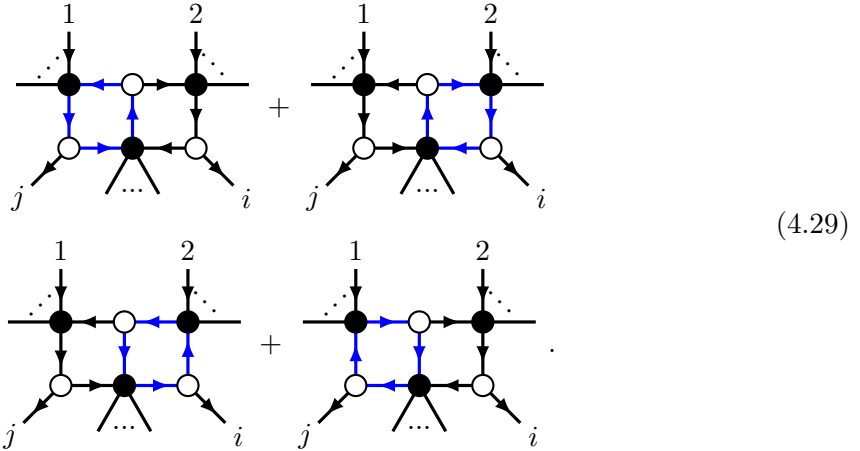
Let us now examine the behavior of the following two Feynman diagrams in the planar limit,



A priori, it is not obvious whether they both contribute at the same order in the planar limit. However, by employing the double-line notation, the diagrams can be rewritten as



and it becomes manifest that the first diagram contributes at leading order in the planar limit, while the second is subleading. This distinction is a crucial difference between QCD and $\mathcal{N} = 4$ sYM, where fermions live in the adjoint representation. From the perspective of leading singularities, which correspond precisely to the maximal cuts of the diagrams shown above, we therefore conclude that in the planar limit only double-box cuts containing a small quark loop contribute. Their contribution at order $\mathcal{O}(N_f N_c)$ is given by the sum of the following four terms,



The reason is that all other on-shell diagrams featuring a “large” quark cycle running along the perimeter are subleading, scaling as $\mathcal{O}(N_f)$, compared to the four on-shell diagrams above, which scale as $\mathcal{O}(N_c N_f)$. Summing these four on-shell diagrams, we reproduce the two-loop leading singularities for the N_f -contributions reported in [92],

$$S_{12,ij1,n}^{(2),\text{db}} = \text{PT}_{n,12} \times \left[-2 + 12 \frac{\langle 1i \rangle \langle 2j \rangle}{\langle 12 \rangle \langle ij \rangle} - 21 \left(\frac{\langle 1i \rangle \langle 2j \rangle}{\langle 12 \rangle \langle ij \rangle} \right)^2 + 11 \left(\frac{\langle 1i \rangle \langle 2j \rangle}{\langle 12 \rangle \langle ij \rangle} \right)^3 \right]. \quad (4.30)$$

In this work, we focus on six-gluon amplitudes in QCD. For the N_f -contribution to the two-loop hard function, we summarize the counting of independent prefactors in Table 3. Comparing with Table 2, in each helicity sector the counting always decreases by one, since the tree-level PT factor does not contribute at N_f^1 order. For the N_f^2 -contribution to the two-loop hard function, only the MHV sector $(-+--++)$ is nonvanishing. At this order, the maximally-transcendental contributions originate from the kissing-box cut, having only

	(--++++)	(-+-+++)	(-++-++)
$L = 1$	0	3	4
$L = 2$	6	12	15

Table 3. Counting of independent prefactors for the maximally-transcendental part of the six-point L -loop gluonic QCD hard functions at N_f^1 -order in the MHV helicity sectors.

one independent prefactor. The explicit expressions for all prefactors are provided in the ancillary files. We leave the discussion of on-shell diagrams with external quark legs and the corresponding QCD amplitudes to a future work.

5 Prescriptive unitarity integrals

Having computed the prefactors R_k in (3.5) as on-shell diagrams representing maximal residues along the contours shown in Fig. 2, we now turn to determining the transcendental functions that accompany them. Concretely, we perform loop integrations of the four-dimensional loop integrands \mathcal{I}_k , contributing to the IR-finite part of the amplitude. To separate the IR-finite contributions, we rely on the prescriptive unitarity construction of [93].

The central idea is that, given a set of independent maximal-cut contours, one can construct integrands that isolate individual contours by having unit residue on a chosen contour while vanishing on all others. Suppose we consider a set of independent ℓ -loop chiral contours $\{\alpha_{j,k} = 0\}_{j=1,\dots,4\ell}$, which evaluate the leading singularities $R_k^{(\ell)}$. For each such chiral contour, one can construct the corresponding 4ℓ -fold $d\log$ -form

$$\mathcal{I}_k = \bigwedge_{j=1}^{4\ell} d\log(\alpha_{j,k}), \quad (5.1)$$

which has unit residue on the ℓ -loop cut $\alpha_{j,k} = 0$ and vanishes on all other contours. Once the set of maximal cuts is complete, the four-dimensional amplitude integrand is obtained as a sum of products $\sum_k R_k \times \mathcal{I}_k$. This establishes a one-to-one correspondence between the loop integrands \mathcal{I}_k and the leading singularities $R_k^{(2)}$ in (3.5). As shown in [93], from the perspective of four-dimensional amplitude integrands, once a complete basis of prescriptive integrals has been constructed, all nontrivial physical information about a gauge-theory amplitude is encoded in the prefactors. In this framework, maximal cut contours contributing to the IR-finite part correspond to prescriptive integrals that are finite in four dimensions, whereas contours contributing to the IR-divergent part give rise to prescriptive integrals containing IR-divergences as well. This encapsulates the core idea of prescriptive unitarity.

Having expressed the maximally-transcendental IR-finite contributions to the amplitude in terms of prescriptive integrals, one still needs to rewrite them as conventional Feynman integrals and perform the loop integrations in order to make progress in computing the amplitude. In this section, we recall the explicit expressions for the one- and two-loop prescriptive unitarity integrals, with particular emphasis on those contributing to the IR-finite part of the decomposition (3.5). Furthermore, by examining lower-loop and lower-point expressions for QCD amplitudes available in the literature, we provide additional evidence that prescriptive unitarity integrals capture the maximally-transcendental parts of QCD amplitudes. Although prescriptive unitarity integrals alone are not sufficient to express the two-loop QCD hard functions, they nevertheless prove to be a necessary ingredient in our bootstrap.

5.1 One-loop prescriptive unitarity integrals and amplitudes

At one loop, the non-trivial IR-finite maximal cut contours for MHV amplitudes are the two-mass-easy boxes [47, 94] shown in Fig. 1. The corresponding prescriptive integrals are

obtained by introducing a chiral numerator. This choice ensures a unit residue on one of the two maximal cuts, while yielding vanishing residues on all remaining maximal cuts, including those associated with IR-divergent contours in the soft region of loop momentum. Diagrammatically, we denote such a numerator by a wavy line and write the corresponding integral as

$$, I_{n,jk} = \int \frac{d^4 \ell}{(2\pi)^2} \frac{[\![j, b, c, k]\!]}{\ell_a^2 \ell_b^2 \ell_c^2 \ell_d^2}, \quad (5.2)$$

where

$$[\![a_1, \dots, a_n]\!] := \epsilon_{\alpha_2 \dot{\beta}_1} \cdots \epsilon_{\alpha_n \dot{\beta}_{n-1}} \epsilon_{\alpha_1 \dot{\beta}_n} (a_1)^{\alpha_1 \dot{\beta}_1} (a_2)^{\alpha_2 \dot{\beta}_2} \cdots (a_n)^{\alpha_n \dot{\beta}_n} \quad (5.3)$$

and we abbreviate $p_k \rightarrow k$ and $\ell_a \rightarrow a$ for simplicity. This box integral is a prescriptive integral for the MHV branch of the maximal cut, i.e. $\ell_a^{(1)}$ in (3.7), since its numerator vanishes on the $\overline{\text{MHV}}$ branch as a consequence of the following relation

$$[\![j, b, c, k]\!] = s_{jk} (\ell_a - \ell_a^{(2)})^2 \quad (5.4)$$

while the factor s_{jk} ensures a unit residue on $\ell = \ell_a^{(1)}$.

In fact, one can verify from the one-loop MHV pure YM amplitudes available in the literature that the IR-finite functions associated with the one-loop leading singularities $R_{n,ij}^{(1)}$ (4.7) are given by the chiral two-mass-easy boxes, as expected from the decomposition (3.5). Since the cut shown in Fig. 1 exists only for $|j - k| > 1$, the maximally-transcendental parts of the six-point one-loop MHV hard functions are nonvanishing only in the following two helicity configurations (and their cyclic permutations) and take the form below, in agreement with [134],

$$\begin{aligned} H_{-+-++}^{(1)} &= \text{PT}_{6,13} f_{0,13} + R_{13,24,6}^{(1)} I_{6,24} + R_{13,25,6}^{(1)} I_{6,25} + R_{13,26,6}^{(1)} I_{6,26}, \\ H_{-++-+}^{(1)} &= \text{PT}_{6,14} f_{0,14} + R_{14,25,6}^{(1)} I_{6,25} + R_{14,26,6}^{(1)} I_{6,26} + R_{14,35,6}^{(1)} I_{6,35} + R_{14,36,6}^{(1)} I_{6,36}, \end{aligned} \quad (5.5)$$

where $f_{0,1i}$ are affected by the IR-subtraction.

Similarly, the maximally-transcendental part of the one-loop MHV hard function at arbitrary multiplicity is given by

$$H_{n,1i}^{(1)} = \text{PT}_{n,1i} f_{0,1i} + \sum_{1 < j < i < k \leq n} R_{1i,jk,n}^{(1)} I_{n,jk}, \quad (5.6)$$

where 1 and i label the negative-helicity gluons, $\text{PT}_{n,1i}$ is the Parke-Taylor factor (2.5), and $I_{n,jk}$ are the chiral-boxes given in (5.2).

Finally, it is also worth mentioning that an analogous structure holds for the N_f -term of the one-loop hard functions. As discussed in section 4.3 and summarized in Table 3, the

split-helicity MHV sector gives no contribution, $H_{-+-+++}^{[\frac{1}{2}],(1)} = 0$, while for the remaining two helicity sectors we find

$$\begin{aligned} H_{-+-+++}^{[\frac{1}{2}],(1)} &= S_{13,24,6}^{(1)} I_{6,24} + S_{13,25,6}^{(1)} I_{6,25} + S_{13,26,6}^{(1)} I_{6,26}, \\ H_{-++-++}^{[\frac{1}{2}],(1)} &= S_{14,25,6}^{(1)} I_{6,25} + S_{14,26,6}^{(1)} I_{6,26} + S_{14,35,6}^{(1)} I_{6,35} + S_{14,36,6}^{(1)} I_{6,36}, \end{aligned} \quad (5.7)$$

where the one-loop prefactors of the two-mass-easy box integrals are given in eq. (4.23). The maximally-transcendental part of N_f^1 -contribution to the one-loop MHV gluonic QCD hard function at arbitrary multiplicity is given by

$$H_{n,1i}^{[\frac{1}{2}],(1)} = \sum_{1 < j < i < k \leq n} S_{1i,jk,n}^{(1)} I_{n,jk}. \quad (5.8)$$

5.2 Two-loop prescriptive unitarity integrals

As discussed in section 3, there are five distinct types of two-loop contours. The corresponding prescriptive unitarity integrals were introduced in [93]. Their six-point instances can be found in Ref. [96], specifically in equations (I.1-4), (I.22), (I.23), (I.26) and (I.27) on pages 26–28, which cover the kissing-box, penta-box, double-pentagon, and hexa-box cuts. In addition, since the double-box cut is nonvanishing for pure YM amplitudes, the corresponding double-box prescriptive integrals from Table II of Ref. [93] are also required. This contrasts with $\mathcal{N}=4$ sYM amplitudes, for which these prescriptive integrals do not contribute.

We now list these two-loop prescriptive unitarity integrals using a diagrammatic notation in which wavy lines denote the numerators \mathbf{n}_{topo} where $\text{topo} = \text{kb}, \text{pb}, \text{db}, \text{dp}, \text{hb}$.

1. Kissing-box integrals

$$I_{n,jklm}^{\text{kb}} := \text{Diagram} \quad \mathbf{n}_{\text{kb}} = [\![m, b, c, j]\!] [\![k, f, g, l]\!] \quad (5.9)$$

The diagram shows a kissing-box configuration with two internal vertices. The top-left vertex is connected to a wavy line labeled ℓ_c and a solid line labeled ℓ_b , with external lines j and m . The top-right vertex is connected to a wavy line labeled ℓ_f and a solid line labeled ℓ_g , with external lines k and l . The bottom-left vertex is connected to a wavy line labeled ℓ_b and a solid line labeled ℓ_a , with external lines j and l . The bottom-right vertex is connected to a wavy line labeled ℓ_f and a solid line labeled ℓ_g , with external lines k and m .

2. Penta-box integrals

$$I_{n,jkl}^{\text{pb}} := \text{Diagram} \quad \mathbf{n}_{\text{pb}} = - [\![j, b, c, l]\!] [\![k, f, g, a]\!] + \frac{1}{2} [\![j, b, c, l, k, f, g, a]\!] \quad (5.10)$$

The diagram shows a penta-box configuration with three internal vertices. The top-left vertex is connected to a wavy line labeled ℓ_c and a solid line labeled ℓ_b , with external lines j and l . The top-right vertex is connected to a wavy line labeled ℓ_f and a solid line labeled ℓ_g , with external lines k and m . The bottom-left vertex is connected to a wavy line labeled ℓ_a and a solid line labeled ℓ_b , with external lines j and l . The bottom-right vertex is connected to a wavy line labeled ℓ_e and a solid line labeled ℓ_f , with external lines k and m . The middle vertex is connected to a wavy line labeled ℓ_d and a solid line labeled ℓ_h , with external lines l and m .

3. Double-box integrals

$$I_{n,jkl}^{\text{db}} := \text{Diagram} \quad , \quad \mathbf{n}_{\text{db}} := \frac{1}{2} \llbracket k, b, c, d, e, j \rrbracket \quad (5.11)$$

4. Double-pentagon integrals. These are the special case $C = \emptyset$ of the general “double-pentagon A” integrals in Tab. IV of Ref. [93]. In this special case, the integrals have a double-box topology, but we nevertheless refer to them and denote them as double-pentagons.

$$I_{n,jk}^{\text{dp}} := \text{Diagram} \quad , \quad \mathbf{n}_{\text{dp}} := -\llbracket k, b, c, f, e, j \rrbracket \quad (5.12)$$

5. Hexa-box integrals. These are the special case $C = \emptyset$ of the “general hexa-box B” integrals in Tab. III of Ref. [93]. In this special case, the integrals have a penta-triangle topology, but we nevertheless refer to them and denote them as hexa-boxes. It is worth noting that this integral vanishes when $k-1 = j+1$.

$$I_{n,jk}^{\text{hb}} := \text{Diagram} \quad , \quad \mathbf{n}_{\text{hb}} := s_{j+1, \dots, k-1} \llbracket k, b, c, j \rrbracket \quad (5.13)$$

The two-loop leading singularities $R_k^{(2)}$ appearing in the IR-finite part of the decomposition (3.5) arise from the first three types of maximal cuts, *i.e.* the kissing-box, penta-box and double-box cuts. Consequently, the corresponding IR-finite prescriptive integrals furnish all transcendental functions $\int \mathcal{I}_k$ required to determine the IR-finite part of (3.5). We now specialize the two-loop prescriptive integrals to the six-point case. In the six-point case, the loop integrations of these prescriptive integrals can be carried out using IBP reductions, taking advantage of the known basis of six-point two-loop master integrals. Further details of the IBP reductions employed in this calculation are presented in Appendix A. Up to dihedral permutations of the external legs, there is one kissing-box, three penta-boxes and four double-box integrals, which are shown in Fig. 7. We note that the first four integrals in Fig. 7 coincide with $(\mathcal{I}.1\text{-}4)$ of Ref. [96].

We also remark that, as discussed in [93, 96], the two-loop cuts shown in Figs. 2(d) and 2(e) coincide with one-loop two-mass-easy box cuts and therefore they do not compute

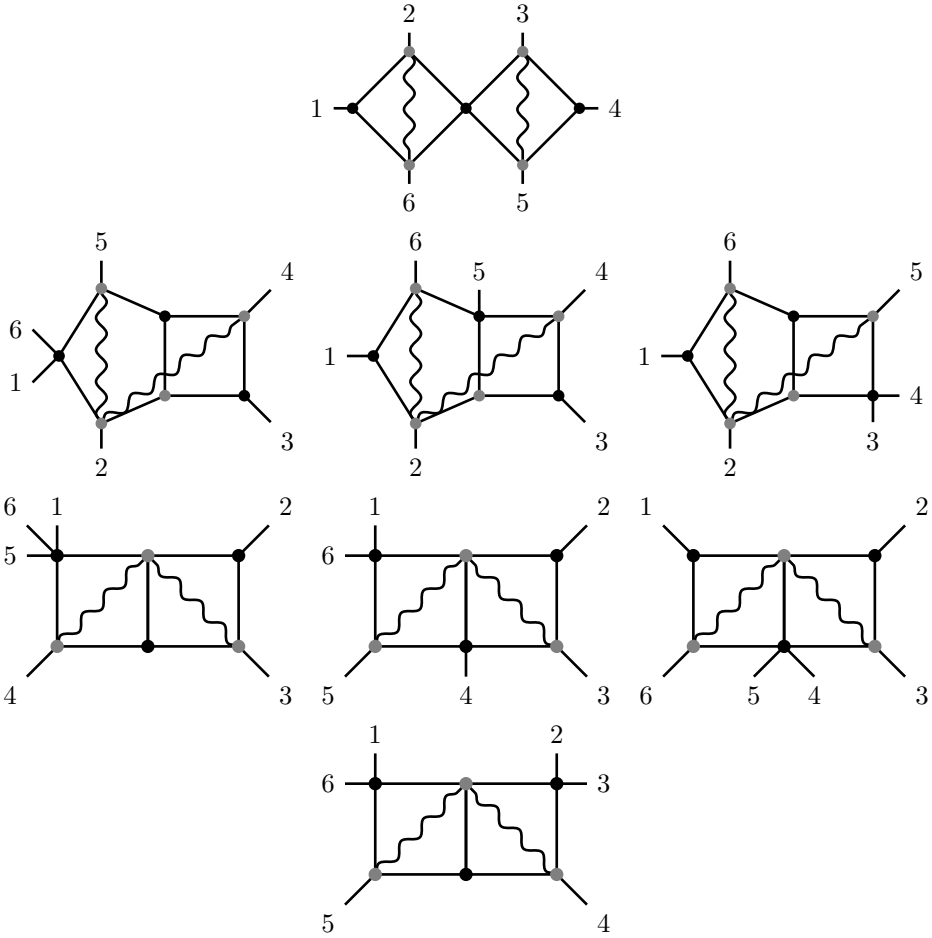


Figure 7. All six-point two-loop prescriptive unitarity integrals for the IR-finite part of MHV amplitudes, up to dihedral permutations of the external legs.

genuinely two-loop leading singularities. Therefore, they contribute to the IR-subtracted part of the two-loop pure YM hard functions in the decomposition (3.5). In section 6, they are required to compute the N_f -contributions to gluonic QCD amplitudes.

5.3 More examples at two loops

Finally, we provide further evidence for the two-loop prescriptive unitarity decomposition of the QCD amplitudes by examining the maximally-transcendental parts of known two-loop results. The examples presented in this part include the four- and five-point hard functions at two loops, for which we refer to results in [17] and [27], and the recently bootstrapped six-point hard function [92] in pure YM theory.

1. Four-point amplitudes:

At four points, the two-loop cuts are the double-boxes. There are two distinct MHV

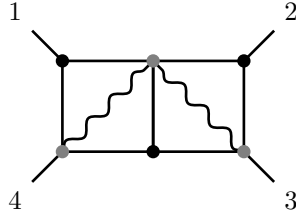


Figure 8. The four-point prescriptive integral contributing to the helicity sector $(- - + +)$.

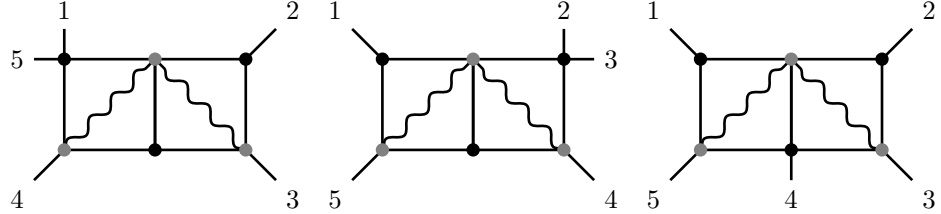


Figure 9. Three five-point prescriptive integrals contributing to the helicity sector $(- - + + +)$.

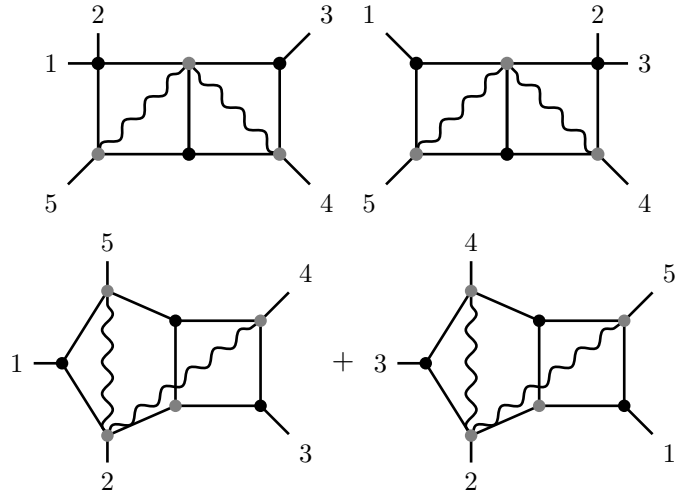


Figure 10. Three combinations of prescriptive integrals contributing to the helicity sector $(- - - + +)$.

helicity sectors, $(- - + +)$ and $(- + - +)$, and the corresponding hard functions are

$$\begin{aligned} H_{- - + +}^{(2)} &= \text{PT}_{4,12} g_{4,12}^{(2)} + R_{12,341,4}^{(2),\text{db}} I_{4,341}^{\text{db}}, \\ H_{- + - +}^{(2)} &= \text{PT}_{4,13} g_{4,13}^{(2)} + R_{13,24,4}^{(1)} g_{4,24}^{(2)}. \end{aligned} \quad (5.14)$$

The double-box prescriptive integral shown in Fig. 8 contributes in the helicity sector $(- - + +)$, whereas no IR-finite double-box integral exists in the helicity sector $(- + - +)$. Indeed, as noted above, the double-box cut contributes only when the indices j and k in (4.15) satisfy $i < j < k \leq n < 1$. The pure functions $g_{4,1i}^{(2)}$ and $g_{4,24}^{(2)}$ receive contributions from IR subtraction. We do not attempt to trace their origin to explicit Feynman integrals.

2. Five-point amplitudes:

At five points, there are two inequivalent MHV helicity sectors. By examining the maximally-transcendental part of the two-loop hard function in the helicity sector $(--+++)$, one finds three independent prefactors in addition to the tree-level PT factor. By contrast, the one-loop hard function in this helicity sector involves only the PT factor. Consequently, the transcendental functions accompanying the three genuinely two-loop prefactors are determined by IR-finite prescriptive integrals. Furthermore, as discussed in section 4, for the helicity sector $(--+\cdots)$ we only need to consider double-box cuts. Accordingly the hard function takes the form,

$$H_{--+++}^{(2)} = \text{PT}_{5,12} g_{5,12}^{(2)} + R_{12,341,5}^{(2),\text{db}} I_{5,341}^{\text{db}} + R_{12,451,5}^{(2),\text{db}} I_{5,451}^{\text{db}} + R_{12,351,5}^{(2),\text{db}} I_{5,351}^{\text{db}}, \quad (5.15)$$

where $g_{5,12}^{(2)}$ is a pure function arising from IR subtraction, and the three double-box integrals are depicted in Fig. 9.

Similarly, one finds five independent prefactors, in addition to the PT factor, in the two-loop hard function for the helicity sector $(-+-++)$. Two of these prefactors are inherited from one loop and are given by (4.7), while the remaining three are genuinely two-loop. In this helicity sector, both double-box and penta-box cuts contribute. The expression for the two-loop hard function can be written in the following form, where the three pure functions accompanying the two-loop prefactors are given by three combinations of prescriptive integrals shown in Fig. 10,

$$\begin{aligned} H_{-+-++}^{(2)} = & \text{PT}_{5,13} g_{5,13}^{(2)} + R_{13,24,5}^{(1)} g_{5,24}^{(2)} + R_{13,25,5}^{(1)} g_{5,25}^{(2)} \\ & + R_{13,451,5}^{(2),\text{db}} I_{5,451}^{\text{db}} + R_{13,452,5}^{(2),\text{db}} I_{5,452}^{\text{db}} + R_{13,245,5}^{(2),\text{pb}} (I_{5,245}^{\text{pb}} + I_{5,254}^{\text{pb}}). \end{aligned} \quad (5.16)$$

Specifically, the two penta-box integrals combine, since the penta-box prefactor (4.13) is determined by two distinct penta-box on-shell diagrams, see (4.14).

3. Six-point amplitude:

Our final example is the six-point MHV hard function in the helicity sector $(--++++)$, which has the following form [92],

$$H_{--+++-}^{(2)} = \text{PT}_{6,12} f_0 + \sum_{2 < i < j \leq 6} R_{12,ij1,6}^{(2),\text{db}} I_{6,ij1}^{\text{db}}, \quad (5.17)$$

where the pure function f_0 is affected by IR subtraction, and the prescriptive integrals accompanying the prefactors R^{db} are six double-boxes (four of these are shown in Fig. 7, while the remaining two are obtained by reflection $p_i \leftrightarrow p_{3-i}$). These are all possible double-box integrals $I_{n,jkl}^{\text{db}}$ with $l = 1$ and $2 < j < k \leq 6$. We conjecture that the IR-finite part of the two-loop hard function at arbitrary multiplicity n in the MHV sector $(--+\cdots)$ is obtained by replacing 6 with n in the summation range of the previous equation.

6 Bootstrapping six-gluon QCD amplitudes

Having discussed the IR decomposition (3.5) of the maximal weight projection of QCD amplitude integrands, reviewed the basis of prescriptive unitarity integrals, and classified the associated prefactors, we are now in a position to complete the computation of the QCD hard functions. We adopt a hybrid strategy that combines the symbol bootstrap with IBP reductions.

As explained in section 5, the prescriptive integrals completely determine the IR-finite part of the decomposition (3.5), and hence the corresponding contributions to the hard functions. These prescriptive integrals are calculated in Appendix A by projecting them onto a basis of six-point two-loop master integrals using IBP reductions. This task is significantly simpler than a full amplitude calculation via IBP, since the prescriptive integrals are finite in four dimensions, have unit leading singularities, evaluate to pure functions, and possess numerators of relatively low rank.

For the IR-subtracted part of the hard function, which involves tree-level PT factors and one-loop prefactors (4.7), we remain agnostic about the explicit loop integrand and instead employ a symbol ansatz, thereby avoiding direct loop integrations. The availability of explicit symbol representations for the prescriptive integrals drastically reduces the number of free parameters in the bootstrap ansatz compared to that used in the Letter [92] for the split-helicity MHV configuration. We find that this reduction is essential for uniquely fixing all remaining free parameters in the bootstrap for the other MHV helicity sectors.

We begin by bootstrapping the N_f^0 contributions and construct the corresponding ansatz using the prefactors enumerated in Table 2. We then turn to the quark contributions, which are N_f^k terms of the hard function with $k = 1, 2$. Guided by the known five-point two-loop results, we find that these contributions are determined by a dozen of functions and prescriptive integrals. Calculations in this section can be generalized to QCD amplitudes with quark external legs in a similar manner.

Finally, we examine the properties of the resulting hard functions, including their common symbol alphabet and the adjacency conditions. In particular, by uncovering a connection between our bootstrapped pure YM results and the two-loop six-point MHV remainder function in $\mathcal{N} = 4$ sYM theory, we shed light on the principle of maximal transcendentality from the perspective of prescriptive unitarity. This connection is discussed at the end of this section.

6.1 Bootstrapping pure YM amplitudes

Up to dihedral permutations, there are three inequivalent MHV helicity configurations of six external gluons. The sector $(-++++)$ was previously studied in the Letter [92]. We first revisit this case using prescriptive unitarity, and then complete the calculation for the remaining two MHV sectors, $(-+-+++)$ and $(-++-++)$ ⁵.

⁵It is worth noting that, in our initial approach to this problem, we adopted the bootstrap strategy of [92], which does not rely on the prescriptive unitarity and therefore requires a more general symbol ansatz. While the available physical constraints were sufficient to uniquely fix the sector $(-+-+++)$, the sector $(-+-+++)$ still contained approximately a dozen unfixed parameters. Nevertheless, these partially

We begin by outlining the symbol spaces and physical constraints employed in our bootstrap. Not all of the 712 independent two-loop weight-four symbols discussed in section 2.5 are required in our analysis. Since hard functions depend only on ratios of Mandelstam variables, the symbol entries can be chosen to be dimensionless. This choice reduces the number of independent weight-four symbols to 430. Furthermore, for each helicity sector we impose the corresponding dihedral symmetry relations (see (2.29)) and construct a symbol ansatz that manifestly respects these symmetries.

To fix all free parameters in the symbol ansatz, we impose several necessary physical constraints, namely spurious pole cancellation and consistency with the collinear and triple-collinear limits. First, the leading singularities $R_{i,j}^{(1)}$ and $R^{(2),\text{topo}}$, defined in (4.7) and (4.16), contain spurious poles at $\langle ij \rangle = 0$ for non-adjacent i and j . These unphysical singularities must be eliminated by requiring the accompanying weight-four symbols to vanish on these loci.

Second, we require the symbol ansatz to reproduce the known five-point planar hard functions of Ref. [27] in the limit where a pair of adjacent particles becomes collinear. In practice, we implement the collinear limits using the momentum-twistor parametrization of the kinematics. For definiteness, we take the limit $p_5 \parallel p_6$ and obtain the remaining cases by cyclic permutations of the ansatz. In momentum-twistor variables, we take

$$Z_6 \rightarrow Z_5 + \epsilon(a_1 Z_1 + a_2 Z_4) + \epsilon^2 a_3 Z_2, \quad (6.1)$$

where the parameters a_i are arbitrary and must cancel from the hard function in the limit $\epsilon \rightarrow 0$.

Third, we impose the triple-collinear limit of the symbol ansatz. When three adjacent external legs become collinear, the ansatz should reproduce the known four-point hard functions. Implementing this limit in momentum twistors and considering $p_4 \parallel p_5 \parallel p_6$, we take

$$Z_5 \rightarrow Z_4 + \epsilon(a_1 Z_3 + a_2 Z_1) + \epsilon^2 a_3 Z_2, \quad Z_6 \rightarrow Z_4 + \epsilon(b_1 Z_3 + b_2 Z_1) + \epsilon^2 b_3 Z_2, \quad (6.2)$$

where a_i and b_i are arbitrary parameters that must cancel from the hard function in this limit. A detailed review of multi-collinear limits of QCD scattering amplitudes is provided in section 7. In these limits, the hard functions obey the universal behavior specified in eqs. (7.8) and (7.25) whenever they develop singularities in the corresponding kinematic regimes. In particular, such singular behavior is required for tree-level amplitudes.

For all MHV helicity sectors, all free parameters in the symbol ansätze are uniquely fixed once the above conditions are imposed simultaneously.

Amplitudes and hard functions are known to exhibit universal behavior in the soft and multi-soft limits. These limits are not required as physical constraints in our bootstrap procedure, since a unique solution is obtained without invoking them. Nevertheless, we use them as nontrivial consistency checks of the bootstrapped results. We implement the soft constrained results already exhibited a clear correspondence with prescriptive unitarity integrals, which in turn motivated the more focused and efficient bootstrap strategy presented in this section.

kinematics using a momentum-twistor parametrization,

$$Z_6 \rightarrow Z_5 + a_1 Z_1 + \epsilon (a_2 Z_4 + a_3 Z_2), \quad (6.3)$$

where p_6 becomes soft, $p_6 \rightarrow 0$, as $\epsilon \rightarrow 0$. The double-soft limit can be implemented analogously by applying a similar parametrization to a pair of momentum twistors. Further details on soft and multi-soft limits are collected in section 7. In these limits, the hard functions behave as specified in eqs. (7.41) and (7.46).

Finally, we also calculated the multi-Regge asymptotics of the bootstrapped hard functions, which are presented in Appendix C.

Having outlined the general bootstrap strategy, we proceed to construct ansätze for each MHV helicity sector using the two-loop six-point planar symbol basis and the prescriptive unitarity framework. In the section, since $n = 6$ always holds, we drop the subscript n of all leading singularities (4.7), (4.10), (4.13), and (4.16) in the expressions.

1. Sector $(-+ +++)$:

The hard function in this sector was bootstrapped in [92]. Here, building on the decomposition (3.5), we instead employ a refined ansatz,

$$H_{-+ +++}^{(2)} = \text{PT}_{6,12} f_0 + \sum_{2 < i < j \leq 6} R_{12,ij1}^{(2),\text{db}} I_{6,ij1}^{\text{db}}, \quad (6.4)$$

where f_0 is a pure function for which we employ a symbol ansatz, the prefactors $R_{12,ij1}^{(2),\text{db}}$ are defined in eq. (4.16), and $I_{6,ij1}^{\text{db}}$ are the explicitly known double-box prescriptive integrals (5.11). Imposing the dihedral symmetry $p_i \leftrightarrow p_{3-i}$ of the hard function (see (2.29)) reduces the number of free parameters in the ansatz for f_0 from 430 to 238. These constitute the remaining unknowns in our ansatz, which are to be fixed by imposing physical constraints.

As shown in [92], the collinear and triple-collinear limits are sufficient to uniquely fix all remaining unknowns in this ansatz. In total, there are five independent collinear limits and four independent triple-collinear limits we can consider in this sector. The first column of Table 4 summarizes the number of independent constraints arising from each condition.

2. Sector $(-+ -++)$:

For this sector, the genuinely two-loop prefactors are determined by the on-shell diagrams shown in Fig. 5. These prefactors are accompanied by explicitly known prescriptive integrals. Accordingly, we adopt the following ansatz with 13 prefactors,

$$H_{-+ -++}^{(2)} = \text{PT}_{6,13} g_0 + R_{13,24}^{(1)} g_{2,4} + R_{13,25}^{(1)} g_{2,5} + R_{13,26}^{(1)} g_{2,6} + \sum_{\substack{l=1,2 \\ 3 < j < k \leq 6}} R_{13,jkl}^{(2),\text{db}} I_{6,jkl}^{\text{db}} + \sum_{\{j,k,l\} \in \sigma_1} R_{13,jkl}^{(2),\text{pb}} (I_{6,jkl}^{\text{pb}} + I_{6,jlk}^{\text{pb}}), \quad (6.5)$$

where $\sigma_1 = \{\{2, 4, 5\}, \{2, 4, 6\}, \{2, 5, 6\}\}$, and g_0 , $g_{2,4}$, $g_{2,5}$, and $g_{2,6}$ are pure functions to be determined by the bootstrap. Under the reflection symmetry $p_i \leftrightarrow p_{4-i}$ of the hard function (see (2.29)), the functions g_0 and $g_{2,5}$ are invariant, while $g_{2,4}$ and $g_{2,6}$ are related

by this symmetry. Taking this reflection invariance into account in the symbol ansatz, we find $2 \times 221 + 430 = 872$ unknowns in total.

We now proceed to fix the unknowns in the ansatz, starting with spurious pole cancellation. The one-loop prefactor $R_{13,ij}^{(1)}$ becomes singular as $\langle ij \rangle \rightarrow 0$, which constrains $g_{2,4}$ and $g_{2,5}$ on the loci $\langle 24 \rangle = 0$ and $\langle 25 \rangle = 0$, respectively. It is worth noting that the two-loop prefactors $R^{(2),\text{topo}}$ involve the same spurious poles, so their cancellation occurs among several terms in the ansatz (6.5). More precisely, we find that the nonvanishing residues at these spurious poles are all proportional,

$$\begin{aligned} \text{Res}_{\langle 24 \rangle=0} R_{13,24}^{(1)} &= \text{Res}_{\langle 24 \rangle=0} R_{13,245}^{(2),\text{pb}} = \text{Res}_{\langle 24 \rangle=0} R_{13,246}^{(2),\text{pb}} \neq 0, \\ \text{Res}_{\langle 25 \rangle=0} R_{13,25}^{(1)} &= \text{Res}_{\langle 25 \rangle=0} R_{13,452}^{(2),\text{db}} = -\text{Res}_{\langle 25 \rangle=0} R_{13,561}^{(2),\text{db}} = \text{Res}_{\langle 25 \rangle=0} R_{13,245}^{(2),\text{pb}} = \text{Res}_{\langle 25 \rangle=0} R_{13,256}^{(2),\text{pb}} \neq 0, \end{aligned} \quad (6.6)$$

which leads to constraints on the associated pure functions that are imposed at the level of symbols,

$$\begin{aligned} \left(g_{2,4} + I_{245}^{\text{pb}} + I_{254}^{\text{pb}} + I_{246}^{\text{pb}} + I_{264}^{\text{pb}} \right) \Big|_{\langle 24 \rangle \rightarrow 0} &= 0, \\ \left(g_{2,5} + I_{452}^{\text{db}} - I_{561}^{\text{db}} + I_{245}^{\text{pb}} + I_{254}^{\text{pb}} + I_{256}^{\text{pb}} + I_{265}^{\text{pb}} \right) \Big|_{\langle 25 \rangle \rightarrow 0} &= 0. \end{aligned} \quad (6.7)$$

Owing to the reflection symmetry of the ansatz, cancellation of the spurious pole at $\langle 26 \rangle = 0$ follows directly from that at $\langle 24 \rangle = 0$.

Finally, we consider the multi-collinear limits. In this helicity sector, the hard function exhibits universal behavior in six collinear limits and five triple-collinear limits. The triple collinear limit $p_1 \parallel p_2 \parallel p_3$, however, does not provide useful physical information, since the amplitude is nonsingular in this regime owing to the vanishing of the tree-level $\text{PT}_{6,13}$. To fully exploit the multi-collinear constraints, one must also account for the corresponding gluon splitting functions. At two loops, the collinear splitting functions are well-known, whereas the triple gluon splitting functions are not known apriori. Using the already bootstrapped helicity sector $(-+ + + +)$, we extract the following MHV triple gluon splitting functions [92],

$$+ \rightarrow +++, \quad - \rightarrow -++, \quad - \rightarrow ++-. \quad (6.8)$$

The remaining triple splitting, $- \rightarrow -+-$, cannot be accessed within this helicity configuration. We therefore impose the physical constraints arising from the three triple-collinear limits associated with the splittings in eq. (6.8).

Altogether, these constraints are sufficient to fix all unknowns in the ansatz and to determine a unique result. The counting of constraints arising from each condition is summarized in the second column of Table 4.

3. Sector $(-+ + + +)$:

Finally, for this sector we construct an ansatz involving 16 prefactors, based on the on-shell diagrams shown in Fig. 6,

$$\begin{aligned}
H_{-+--+}^{(2)} = & \text{PT}_{6,14}h_0 + R_{14,25}^{(1)}h_{2,5} + R_{14,26}^{(1)}h_{2,6} + R_{14,35}^{(1)}h_{3,5} + R_{14,36}^{(1)}h_{3,6} \\
& + R_{14,2356}^{(2),\text{kb}}I_{6,2356}^{\text{kb}} + \sum_{1 \leq l \leq 3} R_{14,56l}^{(2),\text{db}}I_{6,56l}^{\text{db}} + \sum_{4 \leq l \leq 6} R_{41,23l}^{(2),\text{db}}I_{6,23l}^{\text{db}} \\
& + \sum_{\{j,k,l\} \in \sigma_2} R_{14,jkl}^{(2),\text{pb}}(I_{6,jkl}^{\text{pb}} + I_{6,jlk}^{\text{pb}}),
\end{aligned} \tag{6.9}$$

where $\sigma_2 = \{\{6, 2, 3\}, \{5, 2, 3\}, \{2, 5, 6\}, \{3, 5, 6\}\}$, and h_0 and $h_{i,j}$ are pure functions to be determined by the bootstrap. Owing to the dihedral symmetries of the hard function (see (2.29)), we require the ansatz to be invariant under the reflections $p_i \leftrightarrow p_{5-i}$ and $p_i \leftrightarrow p_{8-i}$, as well as under the cyclic shift $p_i \rightarrow p_{i+3}$. The function h_0 is invariant under all these permutations. Under the first reflection, the functions $h_{2,5}$ and $h_{3,6}$ are mapped into one another, as are $h_{2,6}$ and $h_{3,5}$. The function $h_{2,5}$ is invariant under the cyclic shift, while $h_{3,5}$ is invariant under the second reflection. After imposing these discrete symmetry constraints, the resulting symbol ansatz contains $130 + 231 + 221 = 582$ unknowns.

We find the following linear relations among the nonvanishing residues of the prefactors at their spurious poles,

$$\begin{aligned}
\text{Res}_{\langle 25 \rangle=0} R_{14,25}^{(1)} &= \text{Res}_{\langle 25 \rangle=0} R_{41,234}^{(2),\text{db}} = -\text{Res}_{\langle 25 \rangle=0} R_{41,235}^{(2),\text{db}} = \text{Res}_{\langle 25 \rangle=0} R_{41,523}^{(2),\text{pb}} = \text{Res}_{\langle 25 \rangle=0} R_{14,256}^{(2),\text{pb}} \neq 0, \\
\text{Res}_{\langle 35 \rangle=0} R_{14,35}^{(1)} &= \text{Res}_{\langle 35 \rangle=0} R_{41,523}^{(2),\text{pb}} = \text{Res}_{\langle 35 \rangle=0} R_{14,356}^{(2),\text{pb}} \neq 0, \quad \text{Res}_{\langle 35 \rangle=0} R_{14,2356}^{(2),\text{kb}} \neq 0,
\end{aligned} \tag{6.10}$$

and the requirement of spurious pole cancellation then imposes corresponding constraints on the associated symbols,

$$\begin{aligned}
&\left(h_{2,5} + I_{234}^{\text{db}} - I_{561}^{\text{db}} + I_{523}^{\text{pb}} + I_{532}^{\text{pb}} + I_{256}^{\text{pb}} + I_{265}^{\text{pb}} \right) \Big|_{\langle 25 \rangle \rightarrow 0} = 0, \\
&\left(h_{3,5} + I_{523}^{\text{pb}} + I_{532}^{\text{pb}} + I_{356}^{\text{pb}} + I_{365}^{\text{pb}} \right) \Big|_{\langle 35 \rangle \rightarrow 0} = 0.
\end{aligned} \tag{6.11}$$

Finally, the hard function exhibits universal behavior in six collinear and six triple-collinear limits. Analogously to the previous sector, we impose only four triple collinear limits associated with the splittings in eq. (6.8) and disregard the remaining two, which involve the splitting $- \rightarrow +-+$. Taking all these constraints into account, we fix a unique solution to the bootstrap ansatz. In the third column of Table 4, we summarize the counting of constraints arising from each condition.

6.2 From pure YM to QCD hard functions

The pure YM two-loop hard functions bootstrapped in the previous subsection correspond to the N_f^0 -terms, $H_n^{[1],(2)}$, in the N_f -decomposition (2.27) of gluonic QCD hard functions in the planar limit. We now turn to calculating the remaining two-loop N_f^k -terms with $k = 1, 2$ in eq. (2.27). Their prefactors are computed from on-shell diagrams containing quark loops. In light of the IR-decomposition (3.5), in which the IR-finite part is completely

Sectors	(--++++)	(-+-+++)	(-++-++)
unknowns	238	872	582
Conditions			
no spurious poles			
$\langle 24 \rangle = 0$	-	403	-
$\langle 25 \rangle = 0$	-	208	216
$\langle 35 \rangle = 0$	-	-	205
collinear limits			
$p_6 p_5$	216	698	366
$p_5 p_4$	167	698	529
$p_4 p_3$	216	690	529
$p_3 p_2$	216	200	366
$p_2 p_1$	-	200	529
$p_1 p_6$	216	690	529
triple collinear limits			
$p_6 p_5 p_4$	205	283	129
$p_5 p_4 p_3$	205	476	-
$p_4 p_3 p_2$	205	-	129
$p_3 p_2 p_1$	-	-	129
$p_2 p_1 p_6$	-	-	-
$p_1 p_6 p_5$	205	476	129
Total	238	872	582

Table 4. Counting of independent constraints arising from each physical condition in each MHV helicity sector.

determined by the known two-loop prescriptive unitarity integrals, we need to introduce bootstrap ansätze only for the pure functions accompanying the one-loop prefactors (4.23).

At order N_f^1 in the helicity sector $(--++++)$, the one-loop contribution vanishes, $H_{--++++}^{[\frac{1}{2}],(1)} = 0$. As a result, all prefactors contributing at two loops are genuinely two-loop quantities and are computed from the double-box on-shell diagrams in eq. (4.29). The six prefactors $S_{12,ij1}^{(2),\text{db}}$ (see (4.30)) are accompanied by exactly the same double-box prescriptive integrals as in the N_f^0 -term in (6.4). Consequently, this helicity sector is completely fixed by prescriptive unitarity,

$$H_{--++++}^{[\frac{1}{2}]} = \sum_{2 < i < j \leq 6} S_{12,ij1}^{(2),\text{db}} I_{6,ij1}^{\text{db}}. \quad (6.12)$$

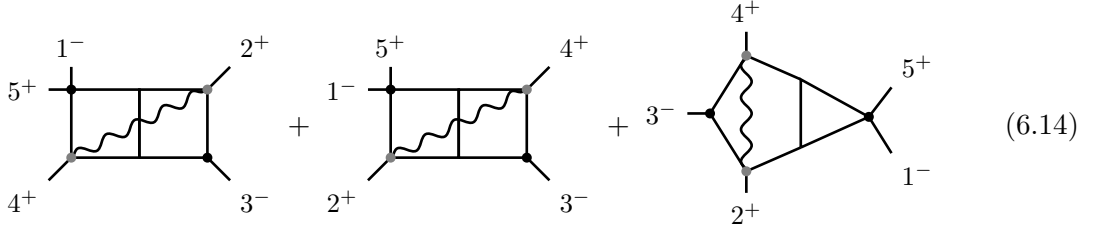
In the helicity sectors $(-+-+++)$ and $(-++-++)$ at order N_f^1 , there are 12 and 15 prefactors, respectively, of which three and four already appear at one loop, see Tab. 3. These one-loop prefactors are precisely those whose accompanying pure functions need to be bootstrapped. A bootstrap procedure employing ansätze analogous to the N_f^0 -expressions (6.5) and (6.9) can be carried out, and unique symbol results can be obtained after imposing

the physical constraints. However, as discussed below, we compute both sectors in a much simpler way, without resorting to the bootstrap.

To uncover relations between the N_f^0 and N_f^1 terms of the six-point hard functions, we first examine the five-point MHV sector $(-+--++)$, using the two-loop results of Ref. [27]. The N_f^0 -contribution, $H_{-+--++}^{[1]}$, is given in eq. (5.16), and an analogous representation holds for the N_f^1 -contribution, $H_{-+--++}^{[\frac{1}{2}]}$. Each involves three genuinely two-loop prefactors, corresponding to the three two-loop maximal cut contours of the integrals in Fig. 10. In both cases, the accompanying pure functions are given by the same set of prescriptive integrals. In contrast to the N_f^0 -contribution (5.16), the N_f^1 -term does not involve the tree-level prefactor $PT_{5,13}$. Its remaining two prefactors are one-loop quantities, $S_{13,24}^{(1)}$ and $S_{13,25}^{(1)}$, defined in (4.23). At one loop, they are computed from one-mass box on-shell diagrams. We verify that the following simple and elegant relation holds among the associated transcendental functions,

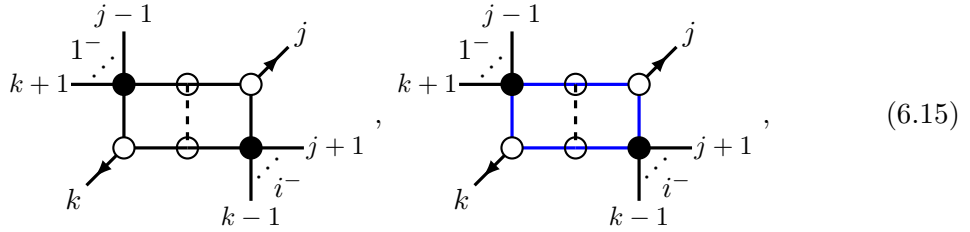
$$f_{2,4}^{[1]} - f_{2,4}^{[\frac{1}{2}]} = I_{24}^{\text{dp}} + \tilde{I}_{24}^{\text{dp}} + I_{42}^{\text{hb}} \quad (6.13)$$

where the functions $f_{2,4}^{[1]}$ and $f_{2,4}^{[\frac{1}{2}]}$ accompany the one-loop prefactors $R_{13,24}^{(1)}$ and $S_{13,24}^{(1)}$, respectively, contributing to $H_{-+--++}^{[1]}$ and $H_{-+--++}^{[\frac{1}{2}]}$. The double-pentagon and hexa-box prescriptive integrals appearing in the rhs of (6.13) are defined in eqs. (5.12) and (5.13), respectively, and $\tilde{I}_{24}^{\text{dp}}$ is obtained from I_{24}^{dp} by the reflection $p_i \rightarrow p_{6-i}$. Diagrammatically, the combination on the rhs of (6.13) can be represented as



An analogous relation holds for the pure functions accompanying the remaining one-loop prefactors $R_{13,25}^{(1)}$ and $S_{13,25}^{(1)}$. The maximal-cut contours associated with the two-loop prescriptive integrals in (6.14) yield the same residues, $R_{1i,jk}^{(1)}$ and $S_{1i,jk}^{(1)}$, as the one-mass box cut, see the discussion in subsection 3.2. Eq. (6.13) therefore shows that the prescriptive double-pentagon and hexa-box integrals contribute to the N_f^0 -term, but not to the N_f^1 -term.

This discrepancy between $f_{j,k}^{[1]}$ and $f_{j,k}^{[\frac{1}{2}]}$ can be understood from the large- N_c scaling of the double-pentagon and hexa-box on-shell diagrams in the planar limit, following reasoning similar to that discussed at the end of subsection 4.3. For instance, the double-pentagon on-shell diagrams with quarks circulating in one of the loops, which evaluate to the one-loop N_f^1 -order prefactors $S_{1i,jk}^{(1)}$, are shown below



where two orientations of the quark loop are possible, together with their reflections. The second diagram, which contains a “large” quark loop and scales as $\mathcal{O}(N_f)$, is suppressed in the planar limit compared to the first diagram, which scales as $\mathcal{O}(N_c N_f)$. An analogous scaling analysis applies to the hexa-box on-shell diagrams. By contrast, in the pure YM case all two-loop planar on-shell diagrams scale uniformly as $\mathcal{O}(N_c^2)$. Consequently, unlike the N_f^1 case, the N_f^0 terms receive additional contributions from purely gluonic on-shell diagrams associated with the double-pentagon and hexa-box contours shown in Fig. 2, and the corresponding prescriptive unitarity integrals contribute. This explains the discrepancy observed in eq. (6.13).

Based on this observation regarding the large- N_c scaling of on-shell diagrams with quark loops, we can immediately write down the N_f^1 -contributions for the remaining two MHV helicity six-point sectors! For the sector $(-+---+)$, we omit the PT term from the pure YM expression (6.5) and replace the one-loop $R^{(1)}$ and two-loop prefactors $R^{(2)}$ with their N_f^1 counterparts $S^{(1)}$ (see (4.23)) and $S^{(2)}$, respectively. These prefactors are computed from on-shell diagrams containing a single quark loop. Moreover, from the pure functions $g_{2,4}$, $g_{2,5}$, and $g_{2,6}$ appearing in (6.5), we subtract the sum of double-pentagon and hexa-box prescriptive integrals, as discussed previously. In this way, we obtain

$$H_{-+---+}^{[\frac{1}{2}]} = \sum_{i=4,5,6} S_{13,2i}^{(1)} (g_{2,i} - I_{2i}^{\text{dp}} - \tilde{I}_{2i}^{\text{dp}} - I_{2i}^{\text{hb}} - I_{i2}^{\text{hb}}) + \sum_{\substack{l=1,2 \\ 3 < j < k \leq 6}} S_{13,jkl}^{(2),\text{db}} I_{6,jkl}^{\text{db}} + \sum_{\{j,k,l\} \in \sigma_1} S_{13,jkl}^{(2),\text{pb}} (I_{6,jkl}^{\text{pb}} + I_{6,jlk}^{\text{pb}}) \quad (6.16)$$

where $\tilde{I}_{2i}^{\text{dp}}$ denotes the reflection $p_k \rightarrow p_{2+i-k}$ of I_{2i}^{dp} , and where $I_{24}^{\text{hb}} = I_{62}^{\text{hb}} = 0$. Remarkably, the resulting expression (6.16) satisfies all physical constraints that would arise in the bootstrap analysis, including the dihedral symmetry, spurious pole cancellation, and the correct behavior in the multi-collinear and soft limits, *etc.*, thereby providing a strong consistency check.

An analogous procedure also applies to the $(-+---+)$ sector and allows us to obtain the N_f^1 contribution from the corresponding N_f^0 expression (6.9),

$$H_{-+---+}^{[\frac{1}{2}]} = \sum_{j=2,3, i=5,6} S_{14,ij}^{(1)} (h_{i,j} - I_{ij}^{\text{dp}} - \tilde{I}_{ij}^{\text{dp}} - I_{ij}^{\text{hb}} - I_{ij}^{\text{hb}}) + S_{14,2356}^{(2),\text{kb}} I_{6,2356}^{\text{kb}} + \sum_{1 \leq l \leq 3} S_{14,45l}^{(2),\text{db}} I_{6,45l}^{\text{db}} + \sum_{4 \leq l \leq 6} S_{41,23l}^{(2),\text{db}} I_{6,23l}^{\text{db}} + \sum_{\{j,k,l\} \in \sigma_2} S_{14,jkl}^{(2),\text{pb}} (I_{6,jkl}^{\text{pb}} + I_{6,jlk}^{\text{pb}}) \quad (6.17)$$

where the pure functions $h_{i,j}$ appear in (6.9), and $\tilde{I}_{ij}^{\text{dp}}$ denotes the reflection $p_k \rightarrow p_{i+j-k}$ of I_{ij}^{dp} .

Finally, as discussed at the end of subsection 4.3, only the MHV sector $(-+-+-+)$ receives an N_f^2 -contribution at maximal transcendentality, originating from the kissing-box cut. The corresponding pure functions are given by the kissing-box prescriptive integrals,

$$H_{-+-+-+}^{[\frac{1}{2}, \frac{1}{2}]} = T_{14,2356}^{(2),\text{kb}} I_{6,2356}^{\text{kb}} \quad (6.18)$$

where the prefactors $T_{14,2356}^{(2),\text{kb}}$ are computed from the kissing-box on-shell diagrams with quarks propagating in both loops.

We have therefore determined all maximally-transcendental contributions to the two-loop planar QCD hard functions for six-gluon MHV amplitudes. The corresponding symbol expressions are collected in the ancillary files.

6.3 Six-point two-loop MHV symbol alphabet

By considering dihedral permutations of the bootstrapped results, we identify the complete set of symbol letters appearing in the maximally-transcendental part of the MHV gluonic QCD hard functions. Our main finding is that this symbol alphabet coincides with the set of 137 letters that have appeared in previous six-point two-loop gauge-theory calculations [92, 97, 98]. This reduces the alphabet from 167 symbol letters present in the finite parts of six-point two-loop Feynman integrals. As discussed in Section 5, the transcendental functions contributing to the hard functions have a clear origin in prescriptive unitarity integrals. This observation suggests that hard functions for quark scattering should likewise be closely related to prescriptive integrals, albeit with different prefactors. These results strongly indicate that, for any six-parton two-loop massless MHV scattering process in QCD, the underlying symbol alphabet is universally given by these 137 letters. We expect that a more systematic study of the six-parton scattering amplitudes, including contributions of non-maximal transcendentality, will further confirm this conjecture.

6.4 From pure YM to $\mathcal{N}=4$ sYM hard functions

We now discuss an interesting relation between the six-point hard functions in pure YM and in $\mathcal{N}=4$ sYM.

Based on our previous discussion of the prescriptive unitarity basis and the maximal weight projection of loop integrands, the four-dimensional amplitude integrands of pure YM and $\mathcal{N}=4$ sYM can be expanded in the same basis of prescriptive integrals, while the prefactors encode the theory dependence. In $\mathcal{N}=4$ sYM, all prefactors of MHV amplitudes are given by the supersymmetric PT factor, which we simply set to unity in this subsection. Consequently, by replacing the nontrivial prefactors appearing in the maximal weight projection of the pure YM integrand (3.5) with rational numbers, one recovers the corresponding four-dimensional integrand of the $\mathcal{N}=4$ sYM amplitude.

Remarkably, our bootstrapped results show that this relation persists at the level of integrated quantities. In the discussion of the finite part of the six-point MHV amplitude in $\mathcal{N}=4$ sYM, one usually introduces the remainder function [36, 135], defined as the dual

conformal invariant ratio of the amplitude to the BDS ansatz [72]. In order to draw a direct parallel between pure YM theory and $\mathcal{N} = 4$ sYM, however, we instead adopt an identical IR subtraction scheme for both gauge theories (see section 2.4). It is worth noting that the hard function in $\mathcal{N} = 4$ sYM differs from the remainder function by the exponentiation of the one-loop hard function. With this choice of IR subtraction, the hard function of $\mathcal{N}=4$ sYM can be obtained from the maximally-transcendental part of the corresponding six-point MHV hard function in pure YM theory by replacing all of its prefactors with rational numbers.

At one loop, consider the hard function for an arbitrary MHV helicity configuration (h_1, \dots, h_6) . Upon replacing all prefactors $\text{PT}_{n,1i}$ and $R_{1i,jk}^{(1)}$ by 1, one recovers the one-loop hard function of $\mathcal{N} = 4$ sYM,

$$H_{h_1 \dots h_6}^{(1)} = \text{PT}_{n,1i} f_0^{(1)} + \sum_i R_{1i,jk}^{(1)} I_{j,k} \xrightarrow{\text{PT}_{n,1i}, R_{1i,jk}^{(1)} \rightarrow 1} \left(H_6^{(1)} \right)^{\mathcal{N} = 4 \text{ sYM}}. \quad (6.19)$$

In particular, in the split-helicity sector $(--++++)$, the maximally-transcendental part of the one-loop hard function in pure YM theory coincides exactly with the hard function in $\mathcal{N}=4$ sYM theory.

At two loops, this relation continues to hold in an analogous manner. Since amplitude integrands in $\mathcal{N}=4$ sYM have no poles at infinity, double-box prescriptive integrals do not contribute to sYM amplitudes. For the bootstrapped result (6.4) in the split-helicity sector $(--++++)$, we verify that

$$f_0 = \left(H_6^{(2)} \right)^{\mathcal{N} = 4 \text{ sYM}}. \quad (6.20)$$

In other words, the two-loop hard functions in the two theories coincide upon setting $R_{12,ij1}^{(2),\text{db}} \rightarrow 0$ in (6.4). For the remaining two MHV helicity sectors, (6.5) and (6.9), double-pentagon and kissing-box prescriptive integrals also contribute. In these cases, the supersymmetric hard function is obtained from the pure YM hard functions by discarding the double-box contributions, $R_{1i,jkl}^{\text{db}} \rightarrow 0$, while replacing all remaining prefactors $R \rightarrow 1$. In a word, for any helicity sector (h_1, h_2, \dots, h_6) at two loops, we have

$$H_{h_1 \dots h_6}^{(2)} \xrightarrow[\substack{R^{(2),\text{db}} \rightarrow 0 \\ \text{PT, } R^{(1)}, R^{(2),\text{pb}}, R^{(2),\text{kb}} \rightarrow 1}]{} \left(H_6^{(2)} \right)^{\mathcal{N} = 4 \text{ sYM}}. \quad (6.21)$$

This identification can be viewed as a manifestation of the principle of maximal transcendentality previously observed in various QCD calculations, as mentioned in the Introduction. We expect that, in $D = 4-2\epsilon$ dimensions, there also exists a basis of prescriptive unitarity integrals. These Feynman integrals are uniformly transcendental in dimensional regularization and therefore contribute to the maximally-transcendental part of gauge-theory amplitudes. All theory-specific information is encoded in the corresponding prefactors, which are computed as D -dimensional leading singularities. Upon restricting to four dimensions, this putative basis for the MHV helicity sectors reduces to the two-loop prescriptive unitarity integrals of Refs. [93, 96]. We leave a detailed investigation of this perspective to future work.

7 Multi-collinear and multi-soft limits and splitting functions

In this section we review the behavior of gluonic QCD scattering amplitudes and their associated hard functions in (multi-)collinear and (multi-)soft limits. In these kinematic regimes, amplitudes factorize in a universal manner governed by splitting and soft functions. This universality makes these limits powerful tools both as physical constraints and as consistency checks in the amplitude bootstrap. Moreover, information extracted from low-multiplicity amplitudes in such limits can be systematically repurposed to constrain higher-multiplicity amplitudes in the same singular kinematic regimes. In section 6, we employed the collinear limit as a physical constraint in the symbol bootstrap of the six-point two-loop MHV hard functions in QCD. In this context, the collinear limit provides inhomogeneous bootstrap input by relating the sought-after six-point hard functions to the previously known five-point ones. Conversely, by analyzing the singular limits of the bootstrapped hard functions, we extract new results for the gluonic two-loop triple-collinear splitting and double-soft functions.

Throughout this work, we restrict to the large- N_c limit. All expressions are understood to refer to their maximally-transcendental contributions and are considered at the level of symbols. In particular, all transcendental constants are systematically omitted.

7.1 Review of collinear limit

For completeness, we briefly review the collinear factorization of QCD amplitudes and their corresponding hard functions. We consider the collinear limit in which a pair of adjacent light-like momenta in an $(n+1)$ -point amplitude, say p_n and p_{n+1} , satisfy

$$p_n \rightarrow z p_{\bar{n}}, \quad p_{n+1} \rightarrow (1-z) p_{\bar{n}} \quad (7.1)$$

where $0 < z < 1$ is the splitting fraction. In this limit, $s_{nn+1} \rightarrow 0$, and the combined momentum becomes light-like, $p_{\bar{n}}^2 = 0$, with $p_n + p_{n+1} \rightarrow p_{\bar{n}}$.

When a gauge theory amplitude develops a collinear singularity, its leading contribution in this kinematic limit is controlled by long-distance dynamics and exhibits a universal factorized structure. For color-ordered planar amplitudes, loop corrections obey the well-known collinear factorization formula [136],

$$A_{n+1}^{(L)}(p_1^{h_1}, \dots, p_n^{h_n}, p_{n+1}^{h_{n+1}}) \rightarrow \sum_{\ell=0}^L \sum_{h=\pm} \text{Split}_{-h}^{(\ell)}(z, p_n^{h_n}, p_{n+1}^{h_{n+1}}) A_n^{(L-\ell)}(p_1^{h_1}, \dots, p_{n-1}^{h_{n-1}}, p_{\bar{n}}^h). \quad (7.2)$$

The associated splitting functions carry nontrivial helicity dependence and decompose as follows

$$\text{Split}_{-h}^{(\ell)}(z, p_n^{h_n}, p_{n+1}^{h_{n+1}}) = \text{Split}_{-h}^{(0)}(z, p_n^{h_n}, p_{n+1}^{h_{n+1}}) r_{-h}^{(\ell) h_n h_{n+1}}(z, s_{nn+1}, \epsilon) \quad (7.3)$$

whenever the tree-level splitting function, $\text{Split}^{(0)}$, does not vanish. The tree-level splitting function contains a simple pole at $s_{nn+1} \rightarrow 0$, while its loop corrections $r^{(\ell)}$ give rise to logarithmic singularities in the collinear limit.

The tree-level splitting functions for the helicity configurations $- \rightarrow ++$ and $+ \rightarrow --$ vanish, and the corresponding loop corrections $r^{(\ell)}$ are of subleading transcendentality. Likewise, in the collinear limits of MHV amplitudes, the splittings $- \rightarrow --$, $+ \rightarrow +-$, and $+ \rightarrow -+$ can be neglected, as they appear in the factorization formula (7.2) multiplied by single-minus amplitudes. These amplitudes also vanish at tree-level, and their loop corrections are again of subleading transcendentality. Consequently, for the purposes of this work, we discard these splittings and retain only the remaining helicity configurations,

$$h \rightarrow h_n h_{n+1} : \quad + \rightarrow ++, \quad - \rightarrow +- , \quad - \rightarrow -+. \quad (7.4)$$

In particular, only a single intermediate helicity state $h = \pm 1$ contributes to the sum on the rhs of eq. (7.2). For example, at tree level the collinear factorization reduces to

$$A_{n+1}^{(0)} \rightarrow \text{Split}_{-h}^{(0)} h_n h_{n+1} A_n^{(0)}, \quad (7.5)$$

where the allowed helicity configurations are those listed in (7.4).

The planar loop corrections $r^{(\ell)}$ for splitting in QCD depend on the helicity configurations in (7.4). However, these discrepancies come in the form of subleading transcendentality contributions [137]. Their maximally-transcendental part is given by the splitting function of $\mathcal{N} = 4$ sYM amplitudes. At one loop, according to [111, 138],

$$r^{(1)}(z, s, \epsilon) = -\frac{1}{\epsilon^2} \left(\frac{(-s)z(1-z)}{\mu^2} \right)^{-\epsilon} + 2 \log(z) \log(1-z) + O(\epsilon) \quad (7.6)$$

and the two-loop splitting function is given by the ABDK/BDS exponentiation [72, 139],

$$r^{(2)} = \frac{1}{2} \left(r^{(1)} \right)^2 + O(\epsilon) \quad (7.7)$$

where we systematically ignore all transcendental constants. The quark flavor contribution also come in as subleading transcendentality, so we can ignore N_f -dependence of the splitting functions.

In our symbol bootstrap, the collinear limits of hard functions are employed, which entails subtracting IR divergences from the collinear factorization of amplitudes in (7.2). For maximally-transcendental parts of one- and two-loop MHV hard functions, normalized by their respective tree-level amplitudes, the collinear factorization takes the following simple form,

$$\begin{aligned} \left(H_{n+1}^{(1)} / A_{n+1}^{(0)} \right) &\rightarrow \left(H_n^{(1)} / A_n^{(0)} \right) + \mathcal{C}^{(1)}, \\ \left(H_{n+1}^{(2)} / A_{n+1}^{(0)} \right) &\rightarrow \left(H_n^{(2)} / A_n^{(0)} \right) + \mathcal{C}^{(1)} \left(H_n^{(1)} / A_n^{(0)} \right) + \frac{1}{2} \left(\mathcal{C}^{(1)} \right)^2, \end{aligned} \quad (7.8)$$

which involves only four-dimensional quantities and is independent of the helicity splitting configurations listed in (7.4). The collinear poles cancel explicitly in the ratios entering (7.8), while logarithmically divergent and finite terms are retained. The one-loop IR-subtracted splitting function is defined in terms of the IR subtraction function (2.24) as [137],

$$\mathcal{C}^{(1)} := I_n^{(1)} + r^{(1)} - \lim_{p_n \parallel p_{n+1}} I_{n+1}^{(1)}, \quad (7.9)$$

which is IR finite and independent of the multiplicity. Neglecting $\mathcal{O}(\epsilon)$ terms, it takes the explicit form,

$$\mathcal{C}^{(1)} = \log(z) \log(1-z) + \log(z) \log \left(\frac{p_{n-1} \cdot p_{\bar{n}}}{p_n \cdot p_{n+1}} \right) + \log(1-z) \log \left(\frac{p_1 \cdot p_{\bar{n}}}{p_n \cdot p_{n+1}} \right). \quad (7.10)$$

Let us note that $\mathcal{C}^{(1)}$ diverges logarithmically in the collinear limit. The exponentiation of loop corrections of the IR-subtracted splitting function in (7.8) is inherited from that in eqs. (2.25) and (7.7).

We emphasize that only hard functions which are singular in the collinear regime admit the universal collinear factorization in eq. (7.8). For instance, the MHV hard function $(++\dots+-)$ is finite and vanishes at tree level in the limit $p_n \parallel p_{n+1}$.

Finally, although the maximally-transcendental parts of the splitting functions are helicity independent, the hard functions themselves retain a non-trivial dependence on the helicity configuration. The collinear limits imposed in the symbol bootstrap are summarized in Tab. 4. We have also verified that the bootstrapped symbols of both pure YM and QCD hard functions satisfy all allowed collinear limits.

7.2 Review of triple-collinear limits

We now turn to the triple-collinear limit [103]. For six-point or higher-multiplicity scattering amplitudes, the kinematics of this limit is non-degenerate. In what follows, we therefore specialize to six-particle scattering. In the triple collinear limit $p_4 \parallel p_5 \parallel p_6$, the momenta of three external particles simultaneously approach a common light-like direction $p_{\bar{4}}$ at the same rate,

$$p_4 \rightarrow z_4 p_{\bar{4}}, \quad p_5 \rightarrow z_5 p_{\bar{4}}, \quad p_6 \rightarrow z_6 p_{\bar{4}}, \quad (7.11)$$

such that $p_4 + p_5 + p_6 \rightarrow p_{\bar{4}}$. The momentum fractions z_4, z_5, z_6 parameterize the splitting,

$$z_4 + z_5 + z_6 = 1, \quad 0 < z_i < 1. \quad (7.12)$$

The triple collinear limit is controlled by a parameter $\delta \rightarrow 0$, with Mandelstam variables involving only the collinear momenta scaling homogeneously,

$$s_{45} \sim s_{56} \sim s_{46} \sim s_{456} \sim \delta^2. \quad (7.13)$$

At tree level, scattering amplitudes develop a triple-collinear pole $1/\delta^2$, which receives logarithmic corrections at loop level. Provided that the color-ordered loop amplitude is singular in this limit, its most singular contribution assumes a universal form,

$$A_6^{(L)}(p_1^{h_1}, \dots, p_6^{h_6}) \rightarrow \sum_{\ell=0}^L \sum_{h=\pm} \text{Split}_{-h}^{(\ell)}(p_4^{h_5}, p_5^{h_5}, p_6^{h_6}) A_4^{(L-\ell)}(p_1^{h_1}, p_2^{h_2}, p_3^{h_3}, p_{\bar{4}}^h) \quad (7.14)$$

where less singular non-universal terms have been omitted on the rhs. In this limit, the kinematics factorizes. The reduced four-point amplitude A_4 depends on s_{12} and s_{23} , while the triple splitting functions depend on $s_{45}/s_{456}, s_{56}/s_{456}, z_4, z_6$. Since we restrict to the

maximally-transcendental parts of six-point MHV helicity amplitudes, and since four-point all-plus and single-minus helicity amplitudes contribute at subleading transcendentality, only the following triple-gluonic splitting channels are relevant,

$$h \rightarrow h_4 h_5 h_6 : \quad + \rightarrow +++, \quad - \rightarrow -++, \quad - \rightarrow ++-, \quad - \rightarrow +-+. \quad (7.15)$$

In this case, a single intermediate helicity state $h = \pm 1$ contributes to the sum in (7.14). The second and third splitting configurations in (7.15) are related by reflection symmetry,

$$\text{Split}_{-h}^{(\ell)}(p_4^{h_5}, p_5^{h_5}, p_6^{h_6}) = \text{Split}_{-h}^{(\ell)}(p_6^{h_6}, p_5^{h_5}, p_4^{h_5}). \quad (7.16)$$

The triple-collinear splitting functions carry a helicity dependence. We focus on their one- and two-loop corrections, which we find convenient to represent in the following form, since the tree-level splitting is nonvanishing for the helicity configurations listed in (7.15),

$$\text{Split}_{-h}^{(1)}(p_4^{h_5}, p_5^{h_5}, p_6^{h_6}) = \text{Split}_{-h}^{(0)}(p_4^{h_5}, p_5^{h_5}, p_6^{h_6}) \left(V_0 + V_{h_4 h_5 h_6}^{(1)-h} \right), \quad (7.17)$$

$$\text{Split}_{-h}^{(2)}(p_4^{h_5}, p_5^{h_5}, p_6^{h_6}) = \text{Split}_{-h}^{(0)}(p_4^{h_5}, p_5^{h_5}, p_6^{h_6}) \left(\frac{1}{2} \left(V_0 + V_{h_4 h_5 h_6}^{(1)-h} \right)^2 + V_{h_4 h_5 h_6}^{(2)-h} \right). \quad (7.18)$$

In contrast to the two-particle splittings in (7.3), three-particle splitting functions exhibit a significantly more intricate kinematic dependence, and comparatively little is known about them beyond one loop. Even at leading color and maximal transcendentality, the QCD triple-collinear splitting functions depend on the helicity configuration $h \rightarrow h_4 h_5 h_6$ as well as on the number of quark flavors N_f . Moreover, they do not obey a simple exponentiation of the one-loop result as in (7.7). In particular, the function $V^{(2)}$ in (7.18) is genuinely nontrivial. As an illustration, the six-gluon two-loop amplitude in $\mathcal{N} = 4$ sYM involves a non-vanishing remainder function, which corrects the one-loop BDS exponentiation of the triple-collinear splitting and can be identified with $V^{(2)}$ in this theory [135].

We now discuss the one- and two-loop functions V_0 , $V^{(1)}$, and $V^{(2)}$, which are free of spinor-helicity variables and appear in the triple-collinear splitting functions (7.17) and (7.18). The function V_0 is helicity independent and captures all IR divergences of the splitting function [103],

$$V_0 = -\frac{1}{\epsilon^2} \left(\left(\frac{-s_{45}}{\mu^2} \right)^{-\epsilon} + \left(\frac{-s_{56}}{\mu^2} \right)^{-\epsilon} + \left(\frac{-s_{456}}{\mu^2} \right)^{-\epsilon} (z_4^{-\epsilon} + z_6^{-\epsilon} - 2) \right). \quad (7.19)$$

The IR-finite part of the one-loop splitting in (7.17), $V_{h_4 h_5 h_6}^{(1)-h}$, depends on the helicity configuration. Its maximally-transcendental part for the first three helicity configurations listed in (7.15) is given by the following pure function [104],

$$\begin{aligned} V_{+++}^{(1)-} &= V_{-++}^{(1)+} = V_{++-}^{(1)+} = \frac{1}{2} [\log^2(z_4) + \log^2(z_6)] - \log \left(\frac{s_{45}}{s_{456}} \right) \log \left(\frac{s_{56}}{s_{456}} \right) \\ &+ \log \left(\frac{1-z_6}{z_4} \right) \log \left(\frac{s_{45}}{s_{456}} \right) + \log \left(\frac{1-z_4}{z_6} \right) \log \left(\frac{s_{56}}{s_{456}} \right) + \text{Li}_2 \left(-\frac{z_5}{z_4} \right) + \text{Li}_2 \left(-\frac{z_5}{z_6} \right) \\ &+ \text{Li}_2 \left(-\frac{z_4}{1-z_4} \right) + \text{Li}_2 \left(-\frac{z_6}{1-z_6} \right) - \text{Li}_2 \left(1 - \frac{s_{45}}{(1-z_6)s_{456}} \right) - \text{Li}_2 \left(1 - \frac{s_{56}}{(1-z_4)s_{456}} \right), \end{aligned} \quad (7.20)$$

where all transcendental constants has been omitted. The remaining helicity configuration in (7.15) instead receives a non-pure contribution [104],

$$V_{+-+}^{(1)+} = V_{+++}^{(1)-} + \left(r_{+-+}^{[1]-} + \frac{N_f}{N_c} r_{+-+}^{[\frac{1}{2}]-} \right) \left(\frac{1}{2} \log^2 \left(\frac{s_{45}}{s_{56}} \right) + \text{Li}_2 \left(1 - \frac{s_{456}}{s_{45}} \right) + \text{Li}_2 \left(1 - \frac{s_{456}}{s_{56}} \right) \right), \quad (7.21)$$

associated with the following prefactors, which can be obtained as triple-collinear limits of the six-point one-loop prefactors (4.7) and (4.23),

$$r_{+-+}^{[1]-} := -1 + \lim_{p_4||p_5||p_6} \frac{R_{i5,46,6}^{(1)}}{\text{PT}_{6,i5}}, \quad r_{+-+}^{[\frac{1}{2}]-} := \lim_{p_4||p_5||p_6} \frac{S_{i5,46,6}^{(1)}}{\text{PT}_{6,i5}} \quad (7.22)$$

where $i = 1, 2, 3$, and the result is independent of the choice of i . They multiply by the pure function in (7.21) given by the finite one-mass box $I_{6,46}$ (5.2).

The IR-finite contribution $V_{h_4 h_5 h_6}^{(2)-h}$ to the two-loop splitting in (7.18) encodes the deviation from one-loop exponentiation. In the following subsection, we determine $V^{(2)}$ from the bootstrapped hard functions. The reflection symmetry of the triple-collinear splitting functions in (7.16), together with that of V_0 , implies the corresponding reflection symmetry for their IR-finite parts,

$$V_{h_4 h_5 h_6}^{(\ell)-h} \left(\frac{s_{45}}{s_{456}}, \frac{s_{56}}{s_{456}}, z_4, z_6 \right) = V_{h_6 h_5 h_4}^{(\ell)-h} \left(\frac{s_{56}}{s_{456}}, \frac{s_{45}}{s_{456}}, z_6, z_4 \right). \quad (7.23)$$

Turning to hard functions, the triple-collinear limit is obtained by subtracting IR divergences from (7.14),

$$\left(H_6^{(1)}/A_6^{(0)} \right) \rightarrow \left(H_4^{(1)}/A_4^{(0)} \right) + \mathcal{C}_{h_4 h_5 h_6}^{(1)-h}, \quad (7.24)$$

$$\left(H_6^{(2)}/A_6^{(0)} \right) \rightarrow \left(H_4^{(2)}/A_4^{(0)} \right) + \mathcal{C}_{h_4 h_5 h_6}^{(1)-h} \left(H_4^{(1)}/A_4^{(0)} \right) + \frac{1}{2} \left(\mathcal{C}_{h_4 h_5 h_6}^{(1)-h} \right)^2 + V_{h_4 h_5 h_6}^{(2)-h}. \quad (7.25)$$

For six-point MHV scattering at maximal transcendentality, a single helicity configuration $h \rightarrow h_4 h_5 h_6$, drawn from the list (7.15), contributes in this limit. The IR divergences of the triple-collinear splitting functions arise exclusively from V_0 (7.19). Subtracting these divergences using the dipole function (2.24), we define

$$\mathcal{C}_0 := I_4^{(1)} + V_0 - \lim_{p_4||p_5||p_6} I_6^{(1)}, \quad (7.26)$$

and decompose the one-loop IR-subtracted triple-collinear splitting function accordingly,

$$\mathcal{C}_{h_4 h_5 h_6}^{(1)-h} := \mathcal{C}_0 + V_{h_4 h_5 h_6}^{(1)-h}, \quad (7.27)$$

where \mathcal{C}_0 takes the following simple form, with all trascendental constants omitted,

$$\mathcal{C}_0 = \log(z_4) \log \left(\frac{s_{12}}{s_{456}} \right) + \log(z_6) \log \left(\frac{s_{23}}{s_{456}} \right). \quad (7.28)$$

In the triple-collinear limit $\delta \rightarrow 0$, \mathcal{C}_0 exhibits logarithmic divergences, while $V^{(1)}$ and $V^{(2)}$ remain finite.

7.3 Two-loop triple-collinear splitting functions

We now turn to the two-loop triple-collinear gluonic splitting functions. More precisely, we focus on the function $V^{(2)}$ in (7.18), which encodes a deviation from the one-loop exponentiation ansatz for the IR finite part of the triple-collinear splitting functions. This function controls the triple-collinear asymptotics of the two-loop hard functions, according to (7.25). As we discussed above, $V^{(2)}$ is IR finite and defined in four dimensions. It is free of helicity-spinor variables, respects the reflection symmetry (7.23), and depends only on the dimensionless variables $s_{45}/s_{456}, s_{56}/s_{456}, z_4, z_6$. Consequently, $V^{(2)}$ remains finite in the triple-collinear limit $\delta \rightarrow 0$.

As discussed in the previous section, we employ partial information from the triple-collinear limit as input in the symbol bootstrap of the hard functions. Consistency with triple-collinear kinematic factorization is sufficient to completely fix the six-point two-loop MHV $--++++$ hard function in (6.4), without requiring an explicit expression for $V^{(2)}$, see also [92]. Subsequently, cyclically permuting the hard function, evaluating its triple-collinear limit, and matching the results to (7.25), we extract the maximally-transcendental part of $V^{(2)}$ for the helicity configurations listed in (6.8).

For the $+\rightarrow+++$ splitting, $V^{(2)}$ is reflection invariant and coincides with its counterpart in $\mathcal{N}=4$ sYM,

$$V_{+++}^{(2)-} = V_{\mathcal{N}=4 \text{ sYM}}^{(2)}, \quad (7.29)$$

where it is given by the two-loop remainder function after expressing the dual-conformal cross-ratios u_1, u_2, u_3 ,

$$u_1 = \frac{s_{12}s_{45}}{s_{123}s_{345}}, \quad u_2 = \frac{s_{23}s_{56}}{s_{234}s_{123}}, \quad u_3 = \frac{s_{34}s_{16}}{s_{345}s_{234}} \quad (7.30)$$

in the triple-collinear limit [135],

$$u_1 \rightarrow \frac{s_{45}}{s_{456}(1-z_6)}, \quad u_2 \rightarrow \frac{s_{56}}{s_{456}(1-z_4)}, \quad u_3 \rightarrow \frac{z_4 z_6}{(1-z_4)(1-z_6)}. \quad (7.31)$$

For the splitting $- \rightarrow -++$, $V^{(2)}$ receives a correction relative to the supersymmetric expression,

$$V_{-++}^{(2)+} = V_{+++}^{(2)-} + \left(r_{-++}^{[1]-} + \frac{N_f}{N_c} r_{-++}^{[\frac{1}{2}]-} \right) \hat{w}_1, \quad (7.32)$$

which is given by a weight-four finite pure function \hat{w}_1 . The accompanying prefactors $r_{-++}^{[1]-}$ and $r_{-++}^{[\frac{1}{2}]-}$ are obtained as the triple-collinear limit of the double-box prefactors in (4.18) and (4.30),

$$r_{-++}^{[1]-} := \lim_{p_4||p_5||p_6} \frac{R_{34,563}^{(2),\text{db}}}{\text{PT}_{6,34}}, \quad r_{-++}^{[\frac{1}{2}]-} := \lim_{p_4||p_5||p_6} \frac{S_{34,563}^{(2),\text{db}}}{\text{PT}_{6,34}}. \quad (7.33)$$

The result for the remaining helicity configuration in (6.8) then follows by applying the reflection symmetry in (7.23).

The triple-splitting functions discussed above are employed as input in the symbol bootstrap of the two remaining MHV hard functions in eqs. (6.5) and (6.9). The corresponding triple-collinear limits are summarized in Tab. 4. We do not invoke the remaining MHV splitting $- \rightarrow ++$ in (7.15) as input for the bootstrap. Instead, we extract the associated splitting function from the bootstrapped MHV hard functions,

$$\begin{aligned} V_{+-+}^{(2)+} = & V_{+++}^{(2)-} + r_{+-+}^{[1]-} \widehat{w}_2 + \frac{N_f}{N_c} r_{+-+}^{[\frac{1}{2}]-} \widehat{w}_3 \\ & - \frac{1}{2} \left(r_{+-+}^{[1]-} + \frac{N_f}{N_c} r_{+-+}^{[\frac{1}{2}]-} \right)^2 \left[\frac{1}{2} \log^2 \left(\frac{s_{45}}{s_{56}} \right) + \text{Li}_2 \left(1 - \frac{s_{456}}{s_{45}} \right) + \text{Li}_2 \left(1 - \frac{s_{456}}{s_{56}} \right) \right]^2 \end{aligned} \quad (7.34)$$

where \widehat{w}_2 and \widehat{w}_3 are reflection-invariant, weight-four finite pure functions, and prefactors $r_{+-+}^{[1]-}$, $r_{+-+}^{[\frac{1}{2}]-}$ are defined in (7.22).

Finally, we have verified that all possible triple-collinear limits of the bootstrapped MHV hard functions are consistent with the extracted functions $V^{(2)}$. We provide triple collinear splitting functions (7.29), (7.32) and (7.34) in the attached file.

7.4 Soft and double-soft limits

In the limit where the momenta of one or more external particles become soft, gauge-theory amplitudes exhibit a universal behavior governed by soft theorems. Provided the amplitude is singular in this limit, its leading singular behavior is captured by the eikonal approximation and encoded in universal soft functions, which are closely related to soft currents. The soft function can be represented as a matrix element describing the emission of soft particles from a gauge-invariant product of light-like Wilson lines oriented along the directions of the hard external momenta. In particular, this representation immediately implies that soft functions are invariant under rescalings of the hard particle momenta. For six-point kinematics, the soft and double-soft limits are nontrivial, and we review them in detail below. This discussion parallels that of the (multi-)collinear limits considered above. Restricting to the maximally-transcendental part of MHV gluon amplitudes, only soft limits of positive-helicity gluons are relevant.

We begin with the single-soft limit. In the limit $p_{n+1} \rightarrow 0$, a color-ordered $(n+1)$ -point amplitude factorizes universally as [140],

$$A_{n+1}^{(L)}(p_1^{h_1}, \dots, p_n^{h_n}, p_{n+1}^{h_{n+1}}) \rightarrow \sum_{\ell=0}^L \sum_{h=\pm} \text{Soft}^{(\ell)}(p_n, p_{n+1}^{h_{n+1}}, p_1) A_n^{(L-\ell)}(p_1^{h_1}, \dots, p_n^{h_n}). \quad (7.35)$$

The singular soft behavior is governed by the soft function

$$\text{Soft}^{(\ell)}(p_n, p_{n+1}^{h_{n+1}}, p_1) = \text{Soft}^{(0)}(p_n, p_{n+1}^{h_{n+1}}, p_1) e^{(\ell)}(p_n, p_{n+1}, p_1; \epsilon). \quad (7.36)$$

At tree level, the soft function exhibits a simple soft pole, while helicity-independent loop corrections $e^{(\ell)}$ generate logarithmic enhancements of the soft singularity. The soft function

is invariant under independent rescalings of the hard momenta, $p_i \rightarrow \lambda_i p_i$ with $i = 1, n$. At one loop, the soft function takes the form [140],

$$e^{(1)} = -\frac{1}{\epsilon^2} \left(-\frac{\mu^2 s_{1n}}{s_{1n+1} s_{nn+1}} \right)^\epsilon + O(\epsilon) \quad (7.37)$$

where all transcendental constants are omitted. At two loops, the maximally-transcendental part of the soft function is independent of the number of quark flavors N_f and is given by the exponentiation of the one-loop result [141],

$$e^{(2)} = \frac{1}{2} \left(e^{(1)} \right)^2 + O(\epsilon). \quad (7.38)$$

In close analogy with the collinear case, we subtract the IR divergences of the soft function using the dipole IR subtraction function (2.24) and subsequently remove the dimensional regulator,

$$\mathcal{S}^{(1)} := e^{(1)} + I_n^{(1)} - \lim_{p_{n+1} \rightarrow 0} I_{n+1}^{(1)}, \quad (7.39)$$

which evaluates to the following expression and exhibits a logarithmic divergence in the soft limit,

$$\mathcal{S}^{(1)} = -\log \left(\frac{s_{1n+1}}{s_{1n}} \right) \log \left(\frac{s_{nn+1}}{s_{1n}} \right). \quad (7.40)$$

The maximally-transcendental part of the MHV hard functions in the single-soft limit $p_{n+1} \rightarrow 0$ of a positive-helicity gluon, $h_{n+1} = 1$, then obeys

$$\begin{aligned} \left(H_{n+1}^{(1)} / A_{n+1}^{(0)} \right) &\rightarrow \left(H_n^{(1)} / A_n^{(0)} \right) + \mathcal{S}^{(1)}, \\ \left(H_{n+1}^{(2)} / A_{n+1}^{(0)} \right) &\rightarrow \left(H_n^{(2)} / A_n^{(0)} \right) + \mathcal{S}^{(1)} \left(H_n^{(1)} / A_n^{(0)} \right) + \frac{1}{2} \left(\mathcal{S}^{(1)} \right)^2. \end{aligned} \quad (7.41)$$

We have explicitly verified that the bootstrapped six-point hard functions satisfy these single-soft limits.

We turn now to the double-soft limit and focus on six-point kinematics. When a pair of external momenta vanish simultaneously, $p_5, p_6 \rightarrow 0$, the color-ordered amplitude factorizes universally as [102],

$$A_6^{(L)}(p_1^{h_1}, \dots, p_6^{h_6}) \rightarrow \sum_{\ell=0}^L \sum_{h=\pm} \text{Soft}^{(\ell)}(p_4, p_5^{h_5}, p_6^{h_6, p_1}) A_4^{(L-\ell)}(p_1^{h_1}, p_2^{h_2}, p_3^{h_3}, p_4^{h_4}) \quad (7.42)$$

where singular behavior in the limit is controlled by a universal double-soft function,

$$\text{Soft}^{(\ell)}(p_4, p_5^{h_5}, p_6^{h_6}, p_1) = \text{Soft}^{(0)}(p_4, p_5^{h_5}, p_6^{h_6}, p_1) J_{h_5 h_6}^{(\ell)}(p_4, p_5, p_6, p_1; \epsilon). \quad (7.43)$$

For the maximally-transcendental part of MHV amplitudes, only soft limits for positive-helicity gluons are relevant, $h_5 h_6 = ++$. The corresponding one-loop double-soft function

has been computed in [108, 109],

$$J_{++}^{(1)} = \left(-\frac{s_{56}}{\mu^2}\right)^{-\epsilon} \left\{ -\frac{2}{\epsilon^2} - \frac{1}{\epsilon} \log\left(\frac{s_{56}s_{14}}{s_{45}s_{16}}\right) - \text{Li}_2\left[1 - \frac{s_{56}s_{14}}{(s_{45}+s_{46})(s_{15}+s_{16})}\right] - \text{Li}_2\left[1 - \frac{s_{16}}{s_{15}+s_{16}}\right] \right. \\ \left. - \text{Li}_2\left[1 - \frac{s_{45}}{s_{45}+s_{46}}\right] - \frac{1}{2} \left[\log^2 \frac{s_{56}s_{14}}{(s_{45}+s_{46})(s_{15}+s_{16})} + \log^2 \frac{s_{16}}{(s_{15}+s_{16})} + \log^2 \frac{s_{45}}{(s_{45}+s_{46})} \right] \right\} \quad (7.44)$$

where we retain only terms of maximal transcendentality. In this approximation, the dependence on the number of quark flavors drops out. Moreover, one readily verifies that $J_{++}^{(1)}$ is invariant under independent rescalings of the hard momenta, $p_i \rightarrow \lambda_i p_i$ with $i = 1, 4$.

Implementing the IR subtraction of the double-soft function,

$$\mathcal{S}_{++}^{(1)} := J_{++}^{(1)} + I_4^{(1)} - \lim_{p_5, p_6 \rightarrow 0} I_6^{(1)} \quad (7.45)$$

we obtain the double-soft limit of the maximally-transcendental part of the MHV hard functions,

$$\begin{aligned} \left(H_6^{(1)}/A_6^{(0)}\right) &\rightarrow \left(H_4^{(1)}/A_4^{(0)}\right) + \mathcal{S}_{++}^{(1)}, \\ \left(H_6^{(2)}/A_6^{(0)}\right) &\rightarrow \left(H_4^{(2)}/A_4^{(0)}\right) + \mathcal{S}_{++}^{(1)} \left(H_4^{(1)}/A_4^{(0)}\right) + \frac{1}{2} \left(\mathcal{S}_{++}^{(1)}\right)^2 + \mathcal{S}_{++}^{(2)}. \end{aligned} \quad (7.46)$$

The function $\mathcal{S}_{++}^{(2)}$ encodes the deviation of the two-loop double-soft function from the simple exponentiation of the one-loop result. It is finite in the double-soft limit and depends on three independent combinations y_1 , y_2 , and y_3 , which are invariant under rescalings of the hard momenta,

$$y_1 = \frac{s_{45}}{s_{46}}, \quad y_2 = \frac{s_{16}}{s_{15}}, \quad y_3 = \frac{s_{45}s_{16}}{s_{56}s_{14}}. \quad (7.47)$$

We find that the maximally-transcendental part of the double-soft function in QCD coincides with that in $\mathcal{N} = 4$ sYM [92],

$$\mathcal{S}_{++}^{(2)} = \mathcal{S}_{\mathcal{N}=4 \text{ sYM}}^{(2)}. \quad (7.48)$$

Indeed, the dual-conformal cross-ratios (see (7.30)) of the $\mathcal{N} = 4$ sYM remainder function are finite in the double-soft limit,

$$u_1 \rightarrow \frac{s_{45}}{s_{46}+s_{45}}, \quad u_2 \rightarrow \frac{s_{14}s_{56}}{(s_{45}+s_{46})(s_{15}+s_{16})}, \quad u_3 \rightarrow \frac{s_{16}}{s_{15}+s_{16}} \quad (7.49)$$

and can be mapped to the variables in (7.47) through a birational transformation.

We have explicitly verified that the bootstrapped six-point hard functions agree with the double-soft limits.

8 Discussion and outlook

In this work, we systematically investigated the analytic structure and carried out a bootstrap computation of the maximally-transcendental part of planar scattering amplitudes in QCD. Starting from the maximal weight projection at the integrand level, we argued that the relevant amplitude prefactors are determined by two-loop contours satisfying triangle power-counting. Focusing on the MHV helicity sector and on IR subtracted hard functions, we showed that the prefactors appearing beyond the Parker-Taylor factor in the maximally-transcendental part are fully described by five types of two-loop contours and their corresponding maximal residues. By exploiting on-shell diagrams and on-shell functions, we derived these prefactors for the maximally-transcendental part of MHV pure YM amplitudes at arbitrary multiplicity. We further extended this analysis to QCD amplitudes, including N_f dependence arising from quark-loop contributions in gluonic amplitudes, as well as amplitudes with external quarks.

We then applied the framework of prescriptive unitarity to six-point two-loop MHV QCD amplitudes and argued that the transcendental functions appearing in the IR-finite parts of these amplitudes can be computed from three types of prescriptive unitarity integrals. We computed these integrals using IBP reduction and expressed the results in a function basis constructed via the canonical differential equation method. Furthermore, using this function basis, we constructed a symbol ansatz for the amplitude contributions affected by IR-subtraction. Employing a symbol-bootstrap approach, we computed the hard functions for three inequivalent MHV helicity sectors with purely gluonic external states. We observed that in all cases the corresponding symbol alphabets form subsets of the previously identified 137-letter alphabet. Finally, we discussed the implications of these bootstrap results for triple-collinear splitting and the double-soft functions.

Beyond providing new results and insights, our work also raises several questions for future investigation.

1. QCD leading singularities and Grassmannian geometry. On-shell diagrams and on-shell functions enjoy deep connections to mathematical structures such as Grassmannian geometry. Prior to this work, these tools have been applied primarily within sYM theories, both with maximal or reduced supersymmetry. Studies of on-shell diagrams involving fermions in QCD, along with their associated leading singularities and geometric interpretations, therefore remain scarce (see the recent work [142] for further developments). Moreover, when extending the analysis to higher multiplicities and non-MHV helicity sectors in QCD, we expect a substantially richer set of contours and prefactors to contribute. This renders the classification of structures analogous to the R-invariants of $\mathcal{N} = 4$ sYM an important direction for future research in QCD. Emerging phenomena, such as three-mass-triangle coefficients in pure YM NMHV amplitudes [134], indicate that this classification will exhibit a far richer structure than in sYM theories. Based on the classification results of leading singularities, we can consider bootstrap computations for helicity amplitudes in other QCD channels, including cases with external quark legs, as well as amplitudes in the NMHV helicity sector.

2. Effective $\mathcal{N}=1$ supersymmetry at maximal transcendentality. In the main text, we analyzed all quark-flavor N_f^k terms in planar gluonic QCD amplitudes. At one loop, an effective $\mathcal{N}=1$ supersymmetric structure emerges in the IR-finite part. Prefactors (4.7) and (4.23) from the same two-mass-easy box can be interpreted as arising from an $\mathcal{N}=1$ vector supermultiplet circulating in the loop. At two loops, however, the situation becomes more intricate. Owing to the different large- N_f and large- N_c scalings of the on-shell diagrams, additional structure emerges that warrants deeper investigation, both in the gluonic sector and in channels involving external quarks. This raises several natural questions. Can systematic connections and distinctions between QCD amplitudes and $\mathcal{N}=1$ sYM amplitudes [143] be identified through amplitudes with different arrangements of external gluons and fermions? Moreover, can on-shell functions and results from $\mathcal{N}=1$ sYM amplitudes facilitate computations in fermionic sectors of QCD, and conversely? We leave these questions for future work.

3. Full classification of QCD amplitude prefactors. In this work, we focused on the maximally-transcendental contributions. A complete calculation of QCD scattering amplitudes, however, also requires determining the subleading-transcendental contributions and rational terms. This therefore reduces once again to the problem of computing and classifying the rational prefactors. The study of two-loop all-plus Yang–Mills amplitudes [144, 145] indicated that, for the prefactors of the non-maximally-transcendental parts, on-shell diagrams with one-loop all-plus Yang–Mills amplitudes inserted as vertices can likewise be used to classify all of their leading-transcendentality prefactors. Besides, at one loop, generalized unitarity [146] has shown that amplitude prefactors are closely tied to specific non-maximal cuts and their associated phase-space integrals. Furthermore, rational terms in the amplitudes come from $D = 4 - 2\epsilon$ cuts of the integrand [131]. We therefore seek a more profound understanding of lower-transcendentality prefactors and of the rational terms. Frontier approaches to this problem also include prescriptive unitarity constructions beyond the maximally transcendental part [129], new surface integral formulation for pure YM amplitudes [147], and so on. We expect that such insights will not only facilitate extensions of our computational framework to higher multiplicities and loop orders, but also deepen our understanding of fundamental principles of QCD from a perturbative perspective.

Acknowledgments

We thank Simon Badger, Jacob Bourjaily, Subramanya Hegde, Xuhang Jiang, Jiahao Liu, Yichao Tang, Congkao Wen, Yu Wu, Huaimin Yu and Yu Jiao Zhu for valuable discussions. This work was supported by the European Union (ERC, UNIVERSE PLUS, 101118787). Views and opinions expressed are however those of the authors only and do not necessarily reflect those of the European Union or the European Research Council Executive Agency. Neither the European Union nor the granting authority can be held responsible for them. D.C. is supported by ANR-24-CE31-7996. YZ is supported by NSFC through Grant No. 12575078 and 12247103.

A IBP reduction calculation for the prescriptive unitarity integrals

To obtain the symbol expressions for prescriptive unitarity integrals, our strategy is to reduce them, via IBP identities, to the known two-loop six-point UT integral basis in [85].

The first step is to rewrite the numerators of prescriptive unitarity integrals to the local integrand form in terms of the trace of gamma matrices. With the definition of [96], those integrals have the numerator form,

$$[a_1, a_2, b_1, b_2, \dots, c_1, c_2] \equiv \left[(a_1 \cdot a_2)^\alpha{}_\beta (b_1 \cdot b_2)^\beta{}_\gamma \cdots (c_1 \cdot c_2)^\delta{}_\alpha \right], \quad (\text{A.1})$$

where for instance a_1 stands for the contraction with Pauli's matrices, $a_1^{\alpha\dot{\alpha}} = l_{1,\mu} \sigma^{\mu, \alpha\dot{\alpha}}$, where l_1 is either an external momentum or a *four-dimensional* loop momentum. $(a_1 \cdot a_2)^\alpha{}_\beta \equiv a_1^{\alpha\dot{\alpha}} \epsilon_{\dot{\alpha}\dot{\gamma}} a_2^{\dot{\gamma}\gamma} \epsilon_{\gamma\beta}$. It is not easy to reduce such expressions in standard IBP reduction programs, so following the discussion in [96], this numerator expression is reformulated as the “Dirac trace”,

$$[\dots] = \text{tr}_+ [\dots] = \frac{1}{2} \text{tr} [(1 + \gamma^5) \dots]. \quad (\text{A.2})$$

The second step is to expand the Dirac trace to the standard input form for IBP reduction programs. The standard procedure in [148] for the local integrand expansion is used here for the expansion. For the Dirac trace with even number of gamma matrices and free of γ_5 , the recursive relation,

$$\text{tr} [\gamma^{\nu_1} \dots \gamma^{\nu_{2n}}] = 2 \sum_{i=2}^{2n} (-1)^i \eta^{\nu_1 \nu_i} \text{tr} [\gamma^{\nu_2} \dots \hat{\gamma}^{\nu_i} \dots \gamma^{\nu_{2n}}], \quad (\text{A.3})$$

reduces the expression to scalar products and $\text{tr}[\mathbb{1}]$. The Dirac trace with the odd number of gamma matrices and free of γ_5 , $n \geq 5$ vanishes. We use the following formula to simplify a long trace with a γ^5 , $n \geq 4$,

$$\begin{aligned} \text{tr} [\gamma^5 \gamma^{\nu_1} \dots \gamma^{\nu_n}] &= \sum_{1 \leq i < j < k < l \leq n} (-1)^{i+j+k+l} \frac{\text{tr} [\gamma^5 \gamma^{\nu_i} \gamma^{\nu_j} \gamma^{\nu_k} \gamma^{\nu_l}]}{\text{tr} [\mathbb{1}]} \\ &\times \text{tr} [\gamma^{\nu_1} \dots \hat{\gamma}^{\nu_i} \dots \hat{\gamma}^{\nu_j} \dots \hat{\gamma}^{\nu_k} \dots \hat{\gamma}^{\nu_l} \dots \gamma^{\nu_n}], \end{aligned} \quad (\text{A.4})$$

For the trace with four γ matrices and a γ^5 ,

$$\text{tr} [\gamma^5 \gamma^{\nu_1} \gamma^{\nu_2} \gamma^{\nu_3} \gamma^{\nu_4}] l_{1,\nu_1} l_{2,\nu_2} l_{3,\nu_3} l_{4,\nu_4} = -\frac{G \begin{pmatrix} l_1 & l_2 & l_3 & l_4 \\ p_1 & p_2 & p_3 & p_4 \end{pmatrix}}{\epsilon(1, 2, 3, 4)}, \quad (\text{A.5})$$

where G denotes the Gram determinant, and $\epsilon(1, 2, 3, 4) = 4i \epsilon_{\mu\nu\rho\sigma} p_1^\mu p_2^\nu p_3^\rho p_4^\sigma$. Traces with fewer γ matrices and a γ^5 vanish. After this step, all prescriptive unitary numerators are converted to the combination of scalar products, the constants $\epsilon(1, 2, 3, 4)$ and $\text{tr}[\mathbb{1}]$. We set $\text{tr}[\mathbb{1}] = 4$.

In the third step, the prescriptive unitarity integrals are reduced in standard IBP programs like FIRE7 [149] and KIRA3 [150]. The two-loop six-point UT basis in [85] is

reduced in the meanwhile. Afterwards, the finite-field tool FINITEFLOW [11, 13] is called to convert the reduction results of prescriptive unitarity integrals on the UT basis. In practice, we find that, with the prescriptions in the first two steps, in all reduction tests, prescriptive unitarity integral in [96] are reduced to linear combinations of UT integrals with *constant* coefficients. Therefore, the IBP reduction for prescriptive unitarity integrals can be done with numeric kinematics.

The typical running time for all three steps in total is less than one hour on a workstation, with 20 cores and 128GB RAM. For example, the following integral with the integrand,

$$I_{6,361}^{\text{db}} := \text{Diagram} \quad , \quad \mathbf{n}_{\text{db}} := \frac{1}{2} [6, b, c, d, e, 3] , \quad (\text{A.6})$$

is reduced to,

$$\begin{aligned} & -\frac{1}{8}\mathcal{I}_{27} - \frac{3}{8}\mathcal{I}_{28} + \frac{1}{8}\mathcal{I}_{29} + \frac{1}{8}\mathcal{I}_{56} + \frac{1}{4}\mathcal{I}_{78} + \frac{1}{4}\mathcal{I}_{106} + \frac{1}{8}\mathcal{I}_{122} - \frac{1}{4}\mathcal{I}_{131} - \frac{1}{4}\mathcal{I}_{138} - \frac{1}{8}\mathcal{I}_{154} \\ & -\frac{1}{8}\mathcal{I}_{156} + \frac{1}{16}\mathcal{I}_{170} + \frac{1}{8}\mathcal{I}_{171} - \frac{1}{8}\mathcal{I}_{173} + \frac{1}{8}\mathcal{I}_{174} - \frac{1}{16}\mathcal{I}_{189} + \frac{3}{16}\mathcal{I}_{202} - \frac{1}{4}\mathcal{I}_{216} + \frac{1}{2}\mathcal{I}_{226} + \frac{1}{4}\mathcal{I}_{227} \\ & -\mathcal{I}_{233} + \frac{3}{16}\mathcal{I}_{243} + \frac{1}{8}\mathcal{I}_{248} - \frac{1}{8}\mathcal{I}_{258} - \frac{3}{8}\mathcal{I}_{259} + \frac{1}{4}\mathcal{I}_{260} + \frac{3}{16}\mathcal{I}_{263} + \frac{3}{16}\mathcal{I}_{264} - \frac{1}{4}\mathcal{I}_{266} , \end{aligned} \quad (\text{A.7})$$

where \mathcal{I}_i is the i -th UT integral for the double pentagon family defined in [85], with the permutation of external legs $p_i \rightarrow p_{i+4}$. From the expression of the UT integrals [85], (A.7) is finite and has the uniform weight four.

We remark that the prescriptive unitarity integrals' numerator essentially consist of *four-dimensional* loop momenta for the spinor helicity formalism [96], but the IBP reduction and the UT integral basis are calculated with dimensional regularization. There is no unique way to upgrade four-dimensional loop momenta to D -dimensional loop momenta, for the IBP reduction. Furthermore, the Dirac trace calculation depends on the chosen scheme. However, since the prescriptive integrals are finite, the different definitions of the (-2ϵ) -dimensional component of loop momenta, or different Dirac trace schemes, are expected to affect only the vanishing parts, $O(\epsilon)$, of those integrals.

B A review of on-shell diagrams and on-shell functions

The computation of on-shell diagrams has been crucial in understanding the underlying combinatorial structure of scattering amplitudes in gauge theories with some degree of supersymmetry. Nonetheless, this construction is perfectly well defined, albeit with fewer simplifications, in theories without supersymmetry, such as Yang-Mills theory or QCD. The purpose of this Appendix is thus to provide a practical guide to computing these functions, starting from the elementary building blocks of any perturbative theory—the three-particle amplitudes. To illustrate this, we work in pure YM, however, everything in our discussion remains valid for general gauge theories.

B.1 Three-particle amplitudes and gluing

As it is, by now, well known, three-particle amplitudes in four dimensions are completely fixed by requiring little group covariance and locality [151]. The usual story goes as follows: The momentum conservation condition for three massless particles is equivalent to

$$\lambda_1^\alpha \tilde{\lambda}_1^{\dot{\alpha}} + \lambda_2^\alpha \tilde{\lambda}_2^{\dot{\alpha}} + \lambda_3^\alpha \tilde{\lambda}_3^{\dot{\alpha}} = 0, \forall \alpha, \dot{\alpha} \in \{1, 2\}. \quad (\text{B.1})$$

This, in turn, produces a degenerate geometric configuration, either in λ -space or in $\tilde{\lambda}$ -space. To see this, one can organize the kinematic data into two three-dimensional vectors - $(\lambda_1^\alpha, \lambda_2^\alpha, \lambda_3^\alpha)$, and equivalently for $\tilde{\lambda}$. For generic momenta, both the λ and the $\tilde{\lambda}$ vectors span two 2-planes in 3 dimensions. What momentum conservation says is that these 2-planes must be orthogonal. In 3 dimensions, this can only be achieved provided one of the 2-planes degenerates into a line. Thus, there are two (parity related) solutions to three-particle momentum conservation condition

$$\begin{cases} \lambda_1 \sim \lambda_2 \sim \lambda_3, & \tilde{\lambda}_i \text{ generic} \\ \tilde{\lambda}_1 \sim \tilde{\lambda}_2 \sim \tilde{\lambda}_3, & \lambda_i \text{ generic}. \end{cases} \quad (\text{B.2})$$

In what follows, we will denote the first with a white vertex and the second with a black vertex. Graphically, we have that the three gluon amplitudes can be represented as

$$\begin{aligned} 2^- & \quad 1^- \\ \text{black vertex} & \quad \text{white vertex} \\ 3^+ & \quad 2^+ \\ & \quad 1^+ \\ & \quad 3^- \end{aligned} = \frac{\langle 12 \rangle^4}{\langle 12 \rangle \langle 23 \rangle \langle 31 \rangle} \delta^{2 \times 2}(\lambda_i \tilde{\lambda}_i), \quad = \frac{[12]^4}{[12][23][31]} \delta^{2 \times 2}(\lambda_i \tilde{\lambda}_i), \quad (\text{B.3})$$

where the momentum conserving delta functions $\delta^{2 \times 2}$ are, in each case separately, supposed to impose the two different parallel conditions of eq. (B.2). Moreover, note how each line is decorated with the corresponding helicity of the respective gluon—arrows going in denote negative helicity, while arrows going out denote positive helicity gluons.

In QCD, we also need to consider three-particle amplitudes involving fermions. We represent these as follows

$$\begin{aligned} 2_q^- & \quad 2_q^- \\ \text{black vertex} & \quad \text{white vertex} \\ 3_q^+ & \quad 2_q^- \\ & \quad 1_g^+ \\ & \quad 3_q^+ \end{aligned} = \frac{\langle 12 \rangle^2}{\langle 23 \rangle} \delta^{2 \times 2}(\lambda_i \tilde{\lambda}_i), \quad = \frac{[31]^2}{[23]} \delta^{2 \times 2}(\lambda_i \tilde{\lambda}_i), \quad (\text{B.4})$$

where fermions with positive helicity are represented by outgoing blue arrows, while negative helicity are represented by incoming blue arrows. Now that we have established the expressions for three-particle amplitudes, we can now discuss how to glue them to obtain more complicated objects.

Given any set of three-particle amplitudes, we can glue them by multiplying the corresponding expressions and integrating over the internal lines' Lorentz phase spaces. For instance, after gluing just two three-particle amplitudes, we obtain a factorization channel.

$$\begin{aligned}
\text{Diagram: } & \text{A four-point tree diagram with a black vertex (1-) and a white vertex (3+). External lines are labeled 1-, 2-, 3+, 4+. Internal lines are labeled } I \text{ and } I. \\
& = \int d^3 \text{LIPS}(I) \frac{\langle 12 \rangle^4}{\langle 12 \rangle \langle 2I \rangle \langle I1 \rangle} \frac{[34]^4}{[34][4I][I3]} \delta^{2 \times 2}(p_1 + p_2 + p_I) \delta^{2 \times 2}(p_3 + p_4 - p_I) \\
& = \delta^4(P_{\text{tot}}) \int d^4 p_I \delta(p_I^2) \delta^{2 \times 2}(p_3 + p_4 - p_I) \frac{\langle 12 \rangle^3}{\langle 2I \rangle \langle I1 \rangle} \frac{[34]^3}{[4I][I3]} \\
& = \delta^4(P_{\text{tot}}) \delta(\langle 34 \rangle) \frac{\langle 12 \rangle^4}{\langle 12 \rangle \langle 23 \rangle \langle 41 \rangle}.
\end{aligned} \tag{B.5}$$

This gluing over the Lorentz invariant phase space of the internal particle can be used to glue *any* on-shell object. In particular, we can glue higher-point MHV trees with three-point anti-MHV. For example, gluing a five-point MHV tree with the white vertex, we obtain a factorization channel

$$\text{Diagram: } \text{A five-point tree diagram with a black vertex (1-) and a white vertex (4). External lines are labeled 1, 2, 3, 4, 5. Internal lines are labeled } I. \\
= \delta^4(P_{\text{tot}}) \frac{\langle 14 \rangle^4}{\langle 12 \rangle \langle 23 \rangle \langle 34 \rangle \langle 51 \rangle} \delta(\langle 45 \rangle). \tag{B.6}$$

In the main text, since we want to connect to the usual unitarity cut analysis, we directly use n -point MHV tree amplitudes as ingredients for producing on-shell diagrams. This is slightly different from the on-shell diagrams of [44], where on-shell diagrams are exclusively made from cubic vertices. However, these can be connected by recognizing that the higher-point trees can be “blown up” into diagrams with only cubic vertices. In the example above, we could have blown up the four-point MHV into

$$\text{Diagram: } \text{A five-point tree diagram with a black vertex (1-) and a white vertex (4). External lines are labeled 1, 2, 3, 4, 5. Internal lines are labeled } I. \xrightarrow{\text{blow up}} \text{A box sub-diagram with a central black vertex (1) and four white vertices (2, 3, 4, 5).} \tag{B.7}$$

Whereas, for other higher point trees, a similar procedure can be done. The box sub-diagram from this blow-up procedure never contains oriented helicity distributions. As a consequence, it is always equivalent to directly sewing a higher-point PT factor.

B.2 BCFW-bridges and Inverse-soft factor

In order to construct arbitrarily complicated on-shell diagrams, we need two basic ingredients: BCFW bridges, which increase the "loop-order" and inverse soft-factors, which increase the number of external legs. A pure gluon BCFW bridge consists of gluing the structure of eq. (B.5) to an arbitrary diagram. This can be computed as follows

$$\begin{aligned}
 \text{Diagram: } & \text{A loop labeled } \mathcal{F} \text{ with two external legs } \hat{a} \text{ and } \hat{b} \text{ entering a black dot, which then splits into legs } a \text{ and } b. \text{ The loop } \mathcal{F} \text{ is connected to a white circle labeled } I. \\
 & = \int_{\hat{a}, \hat{b}, I} \underbrace{\mathcal{A}_L(a, I, \hat{a}) \mathcal{A}_R(b, \hat{b}, I) \mathcal{F}(\hat{a}, \hat{b}, \dots)}_{f(a, b, \hat{a}, \hat{b}, I)} \delta_R^4 \delta_L^4 \delta_{\mathcal{F}}^4 \\
 & = \delta^4(P_{\text{tot}}) \int \frac{dz}{z} \frac{1}{s_{ab}} f(p_{\hat{a}} = \tilde{\lambda}_a(\lambda_a - z\lambda_b), p_{\hat{b}} = \lambda_b(\tilde{\lambda}_b + z\tilde{\lambda}_a)) \\
 & = \delta^4(P_{\text{tot}}) \int \frac{dz}{z} z^{\theta_h} \mathcal{F}(\lambda_{\hat{a}} = \lambda_a - z\lambda_b, \tilde{\lambda}_{\hat{b}} = \tilde{\lambda}_b + z\tilde{\lambda}_a),
 \end{aligned} \tag{B.8}$$

where θ_h is an exponent which depends on the helicity of legs a and \hat{a} . For the sake of conciseness, we graphically represent the possible BCFW bridges and their corresponding z -integrands. We can write them explicitly as follows

$$\begin{aligned}
 \text{Diagram: } & \text{A loop labeled } \mathcal{F} \text{ with two external legs } \hat{a} \text{ and } \hat{b} \text{ entering a black dot, which then splits into legs } a \text{ and } b. \text{ The loop } \mathcal{F} \text{ is connected to a white circle labeled } I. \\
 & = \delta^4(P_{\text{tot}}) \int \frac{dz}{z} z^4 \mathcal{F}(z), \\
 \text{Diagram: } & \text{A loop labeled } \mathcal{F} \text{ with two external legs } \hat{a} \text{ and } \hat{b} \text{ entering a black dot, which then splits into legs } a \text{ and } b. \text{ The loop } \mathcal{F} \text{ is connected to a white circle labeled } I. \\
 & = \delta^4(P_{\text{tot}}) \int \frac{dz}{z} \mathcal{F}(z),
 \end{aligned} \tag{B.9}$$

Note how in the second bridge, we only assigned helicity to the intermediate leg, because the formula applies regardless of the helicity assignment on legs a and b .

To illustrate the usefulness of the construction above, we can apply it to the simplest case discussed so far—the factorization channel of eq. (B.5). Attaching a non-trivial BCFW bridge, we find

$$\begin{aligned}
 \text{Diagram: } & \text{A four-point tree-level diagram with legs } 1, 2, 3, 4 \text{ in a rectangle. The top-left vertex is black, the top-right is white, the bottom-left is white, and the bottom-right is black.} \\
 & = \delta^4(P_{\text{tot}}) \int \frac{dz}{z} \left(\frac{\langle 1\hat{3} \rangle^4}{\langle 12 \rangle \langle 23 \rangle \langle 41 \rangle} \delta(\langle \hat{3}4 \rangle) \right) \\
 & = \frac{\langle 13 \rangle^4}{\langle 12 \rangle \langle 23 \rangle \langle 41 \rangle} \int \frac{dz}{z} (\langle 13 \rangle - z\langle 12 \rangle)^4 \delta(\langle 34 \rangle - z\langle 24 \rangle) \\
 & = \frac{\langle 13 \rangle^4}{\langle 12 \rangle \langle 23 \rangle \langle 34 \rangle \langle 41 \rangle} \left(\frac{\langle 14 \rangle \langle 32 \rangle}{\langle 13 \rangle \langle 24 \rangle} \right)^4,
 \end{aligned} \tag{B.10}$$

which is an example of a non-Parke-Taylor leading singularity already shown in section 4.

The other useful tool in computing on-shell diagrams are the inverse soft-factors. These allow us to increase the number of legs by one, at the cost of introducing a delta function. To any on-shell function \mathcal{F} , we can attach a three-particle vertex in the following way

$$\begin{aligned}
 \text{Diagram: } & \text{A circle labeled } \mathcal{F} \text{ with two external legs labeled } n-1 \text{ and } 1 \text{ (with a dot between them), and a central vertex with a leg labeled } \bar{n} \text{ pointing to it. From this vertex, two legs emerge: one labeled } n \text{ and one labeled } n+1. \\
 & = \int d^4 p_{\bar{n}} \delta(p_{\bar{n}}^2) \delta_{\mathcal{F}}^4(p_n + p_{n+1} - p_{\bar{n}}) \mathcal{F}(p_1, \dots, p_{\bar{n}}) \mathcal{A}_3 \\
 & = \delta(\langle n, n+1 \rangle) \mathcal{F} \left(\lambda_{\bar{n}} = \lambda_n, \tilde{\lambda}_{\bar{n}} = \tilde{\lambda}_n + \frac{\langle r, n+1 \rangle}{\langle r, n \rangle} \tilde{\lambda}_{n+1} \right) \frac{\langle rn \rangle}{\langle r, n+1 \rangle} \delta^4(P_{\text{tot}}), \tag{B.11}
 \end{aligned}$$

where λ_r is an arbitrary reference spinor introduced when solving the momentum-conservation conditions. It may be chosen freely to simplify the calculations, provided it is distinct from λ_n and λ_{n+1} . Furthermore, as in the case of the BCFW bridge, different helicity configurations of legs n and $n+1$ lead to different factors of $\frac{\langle rn \rangle}{\langle r, n+1 \rangle}$. The remaining two soft-factors are

$$\begin{aligned}
 \text{Diagram: } & \text{A circle labeled } \mathcal{F} \text{ with two external legs labeled } n-1 \text{ and } 1 \text{ (with a dot between them), and a central vertex with a leg labeled } \bar{n} \text{ pointing to it. From this vertex, two legs emerge: one labeled } n \text{ and one labeled } n+1. \\
 & = \frac{\langle rn \rangle}{\langle rn+1 \rangle} \bar{\mathcal{F}} \delta(\langle n, n+1 \rangle), \\
 \text{Diagram: } & \text{A circle labeled } \mathcal{F} \text{ with two external legs labeled } n-1 \text{ and } 1 \text{ (with a dot between them), and a central vertex with a leg labeled } \bar{n} \text{ pointing to it. From this vertex, two legs emerge: one labeled } n \text{ and one labeled } n+1. \\
 & = \left(\frac{\langle rn+1 \rangle}{\langle rn \rangle} \right)^3 \bar{\mathcal{F}} \delta(\langle n, n+1 \rangle), \tag{B.12}
 \end{aligned}$$

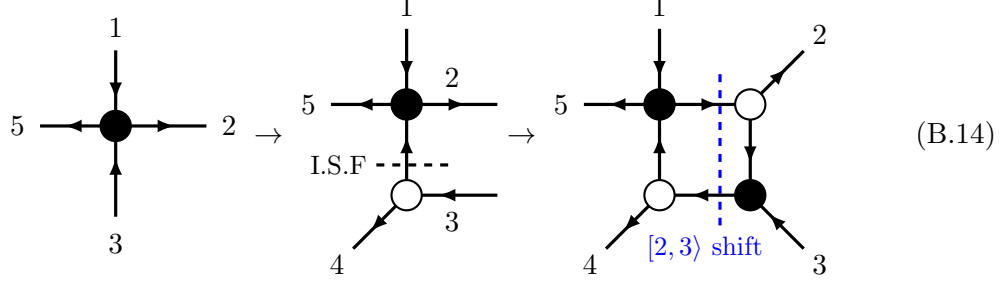
where $\bar{\mathcal{F}}$ is \mathcal{F} evaluated on the kinematic locus of eq. (B.11).

To put both of these methods to use, we end this discussion by computing the following five-point one-loop leading singularity

$$\text{Diagram: } \begin{array}{c} 1 \\ \downarrow \\ \text{A five-point one-loop diagram with a central black dot. It has five external legs labeled 1, 2, 3, 4, and 5. Leg 1 is vertical upwards, leg 2 is diagonal upwards, leg 3 is diagonal downwards, leg 4 is vertical downwards, and leg 5 is horizontal to the left.} \\ \cdot \end{array} \tag{B.13}$$

To compute it, we can break it down into two steps: first insert an inverse soft-factor and

then attach a BCFW bridge. One such possibility is

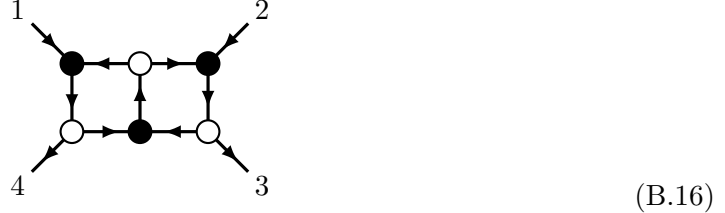


from which we obtain

$$\int \frac{dz}{z} \frac{\langle 1\hat{3} \rangle^4}{\langle 12 \rangle \langle 23 \rangle \langle 45 \rangle \langle 51 \rangle} \delta(\langle \hat{3}4 \rangle) = \text{PT}_{5,13} \left(\frac{\langle 14 \rangle \langle 32 \rangle}{\langle 24 \rangle \langle 13 \rangle} \right)^4, \quad (\text{B.15})$$

which exactly matches the second term of eq. (4.7).

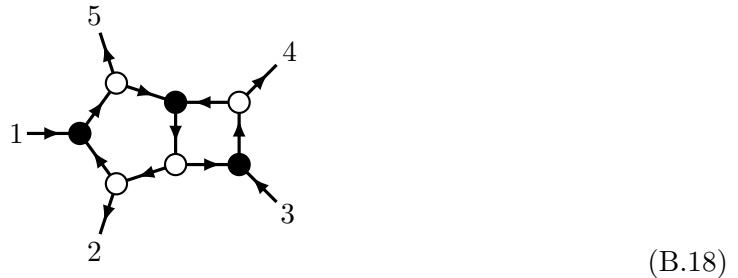
At two loops, low-multiplicity on-shell diagrams can be efficiently evaluated using the BCFW-bridge and inverse-soft constructions, rather than by sewing the tree-level vertices. In particular, this allows one to work recursively in the loop order. For instance, let us consider the four-point amplitude in the helicity configuration $(- - + +)$. Its two-loop leading singularities are computed from the double-box on-shell diagram. One of the helicity assignments featuring two orientated cycles is shown below,



This on-shell diagram is readily evaluated by applying the BCFW $\langle 23 \rangle$ -shift to its one-loop sub-diagram (left box of the double box),

$$\frac{\langle 13 \rangle^4}{\langle 12 \rangle \langle 23 \rangle \langle 34 \rangle \langle 41 \rangle} \left(\frac{\langle 12 \rangle \langle 34 \rangle}{\langle 13 \rangle \langle 24 \rangle} \right)^4 \xrightarrow{\langle 23 \rangle\text{-shift}} dz z^3 \frac{\langle 34 \rangle^3}{\langle 23 \rangle \langle 41 \rangle} \frac{(\langle 12 \rangle + z\langle 13 \rangle)^3}{(\langle 24 \rangle + z\langle 34 \rangle)^4}, \quad (\text{B.17})$$

that corresponds to the first term in the one-form $\Omega_{12,341,4}^{(2),\text{db}}$ (4.16). Similar simplifications also occur for penta-box on-shell diagrams, which we illustrate with the following five-point example in the helicity sector $(- + - + +)$,



We compute this on-shell diagram by attaching an inverse-soft factor to its one-loop box subdiagram,

$$\frac{\langle 35 \rangle^4}{\langle 23 \rangle \langle 34 \rangle \langle 45 \rangle \langle 52 \rangle} \times \left(\frac{\langle 23 \rangle \langle 45 \rangle}{\langle 24 \rangle \langle 35 \rangle} \right)^4 \xrightarrow[\text{factor } \lambda_1]{\text{inverse-soft}} \text{PT}_{5,13} \left(\frac{\langle 12 \rangle \langle 23 \rangle \langle 45 \rangle}{\langle 13 \rangle \langle 24 \rangle \langle 25 \rangle} \right)^4. \quad (\text{B.19})$$

The latter expression corresponds to the first term of $R_{13,245,5}^{(2),\text{pb}}$ given in (4.13).

C Multi-Regge limit

In subsection 6.4, we discussed an interesting relation between the hard functions in pure YM theory and the remainder function in $\mathcal{N} = 4$ sYM. Here we uncover a further interesting connection between these four-dimensional quantities in two gauge theories, now in the multi-Regge limit. Throughout this Appendix, all equations are understood at the level of symbols and for the maximally-transcendental parts.

We consider the bootstrapped pure YM hard functions in the multi-Regge kinematics [152] for the scattering channel $56 \rightarrow 1234$. In this kinematic regime, the transverse momenta are of comparable magnitude

$$|\mathbf{p}_1| \simeq |\mathbf{p}_2| \simeq |\mathbf{p}_3| \simeq |\mathbf{p}_4|, \quad (\text{C.1})$$

while the rapidities are strongly ordered,

$$|p_1^+| \gg |p_2^+| \gg |p_3^+| \gg |p_4^+|, \quad (\text{C.2})$$

$$|p_1^-| \ll |p_2^-| \ll |p_3^-| \ll |p_4^-|, \quad (\text{C.3})$$

where we use light-cone coordinates $p_i = (p_i^+, p_i^-, \mathbf{p}_i)$. To control the multi-Regge regime, we adopt the following parametrization of the kinematics with a small parameter $x \rightarrow 0$,

$$\begin{aligned} s_{12} &= \frac{s_1}{x}, & s_{23} &= \frac{s_2}{x}, & s_{34} &= \frac{s_3}{x}, & s_{56} &= \frac{s_1 s_2 s_3}{\kappa^2 |z_1 - z_2|^2 x^3}, & s_{345} &= -|z_2|^2 \kappa \\ s_{123} &= \frac{s_1 s_2}{\kappa |z_1 - z_2|^2 x^2}, & s_{234} &= \frac{s_2 s_3}{\kappa x^2}, & s_{16} &= -|z_1|^2 \kappa, & s_{45} &= -|1 - z_2|^2 \kappa \end{aligned} \quad (\text{C.4})$$

where only the leading terms in this limit are displayed; s_1, s_2, s_3, κ have the dimensions of Mandelstam variables, while $z_1, \bar{z}_1, z_2, \bar{z}_2$ are dimensionless. We employ the shorthand notation $|z_i|^2 = z_i \bar{z}_i$; in the Euclidean region, z_i, \bar{z}_i are treated as independent variables.

At one loop, we find that all prefactors (see (4.7)) are of the same order as $x \rightarrow 0$, once normalized by the tree-level $\text{PT}_{n,1i}$ (2.5),

$$\frac{R_{1i,jk}^{(1)}}{\text{PT}_{n,1i}} \rightarrow 1 \quad \text{at } x \rightarrow 0. \quad (\text{C.5})$$

The one-loop six-point hard functions for all MHV helicity configurations $(h_1 \dots h_6)$ exhibit identical asymptotic behavior as $x \rightarrow 0$, coinciding with that of the one-loop MHV hard function in $\mathcal{N} = 4$ sYM,

$$H_{h_1 \dots h_6}^{(1)} / A^{(0)} = \left(H^{(1)} / A^{(0)} \right)^{\mathcal{N} = 4 \text{ sYM}} \quad \text{at } x \rightarrow 0 \quad (\text{C.6})$$

where all divergent powers of $\log(x)$ and finite terms are retained, and $A^{(0)}$ is the tree-level partial amplitude given by the PT factor.

At two loops, some prefactors, normalized by the PT factor, become rational numbers $\{0, \pm 1, \pm \frac{1}{2}\}$ as $x \rightarrow 0$, while others diverge in this limit. We verify that the symbols accompanying the divergent prefactors vanish as $x \rightarrow 0$. As a result, the two-loop hard function in this limit is pure, *i.e.*, all prefactors reduce to numerical constants. Moreover, as in the one-loop case, we find that the two-loop hard functions in pure YM theory and $\mathcal{N} = 4$ sYM coincide in the multi-Regge limit for arbitrary MHV helicity configurations,

$$H_{h_1 \dots h_6}^{(2)} / A^{(0)} = \left(H^{(2)} / A^{(0)} \right)^{\mathcal{N} = 4 \text{ sYM}} = \frac{1}{2} \left(\left(H^{(1)} / A^{(0)} \right)^{\mathcal{N} = 4 \text{ sYM}} \right)^2 \quad \text{at } x \rightarrow 0 \quad (\text{C.7})$$

Let us recall that the symbol of the two-loop remainder function of $\mathcal{N} = 4$ sYM vanishes in the multi-Regge limit, which explains the one-loop exponentiation of the hard function in the previous equation.

Finally, we note that the N_f -contributions to QCD hard functions vanish in the multi-Regge limit. Consequently, eqs. (C.6) and (C.7) also hold for the QCD hard functions.

References

- [1] H. Elvang and Y.-t. Huang, *Scattering Amplitudes in Gauge Theory and Gravity*. Cambridge University Press, 4, 2015.
- [2] G. Travaglini et al., *The SAGEX review on scattering amplitudes*, *J. Phys. A* **55** (2022) 443001, [[2203.13011](#)].
- [3] S. Badger, J. Henn, J. C. Plefka and S. Zoia, *Scattering Amplitudes in Quantum Field Theory*, *Lect. Notes Phys.* **1021** (2024) pp., [[2306.05976](#)].
- [4] Z. Bern, L. J. Dixon and D. A. Kosower, *Progress in one loop QCD computations*, *Ann. Rev. Nucl. Part. Sci.* **46** (1996) 109–148, [[hep-ph/9602280](#)].
- [5] R. Britto, F. Cachazo and B. Feng, *Generalized unitarity and one-loop amplitudes in $N=4$ super-Yang-Mills*, *Nucl. Phys. B* **725** (2005) 275–305, [[hep-th/0412103](#)].
- [6] G. Ossola, C. G. Papadopoulos and R. Pittau, *Reducing full one-loop amplitudes to scalar integrals at the integrand level*, *Nucl. Phys. B* **763** (2007) 147–169, [[hep-ph/0609007](#)].
- [7] K. Chetyrkin and F. Tkachov, *Integration by parts: The algorithm to calculate beta-functions in 4 loops*, *Nuclear Physics B* **192** (1981) 159–204.
- [8] A. V. Kotikov, *Differential equations method: New technique for massive Feynman diagrams calculation*, *Phys. Lett. B* **254** (1991) 158–164.
- [9] J. M. Henn, *Multiloop integrals in dimensional regularization made simple*, *Phys. Rev. Lett.* **110** (2013) 251601, [[1304.1806](#)].
- [10] J. M. Henn, *Lectures on differential equations for Feynman integrals*, *J. Phys. A* **48** (2015) 153001, [[1412.2296](#)].
- [11] T. Peraro, *Scattering amplitudes over finite fields and multivariate functional reconstruction*, *JHEP* **12** (2016) 030, [[1608.01902](#)].

[12] S. Abreu, F. Febres Cordero, H. Ita, M. Jaquier, B. Page and M. Zeng, *Two-Loop Four-Gluon Amplitudes from Numerical Unitarity*, *Phys. Rev. Lett.* **119** (2017) 142001, [[1703.05273](#)].

[13] T. Peraro, *FiniteFlow: multivariate functional reconstruction using finite fields and dataflow graphs*, *JHEP* **07** (2019) 031, [[1905.08019](#)].

[14] E. W. N. Glover, C. Oleari and M. E. Tejeda-Yeomans, *Two loop QCD corrections to gluon-gluon scattering*, *Nucl. Phys. B* **605** (2001) 467–485, [[hep-ph/0102201](#)].

[15] Z. Bern, A. De Freitas and L. J. Dixon, *Two loop helicity amplitudes for gluon-gluon scattering in QCD and supersymmetric Yang-Mills theory*, *JHEP* **03** (2002) 018, [[hep-ph/0201161](#)].

[16] Z. Bern, A. De Freitas and L. J. Dixon, *Two loop helicity amplitudes for quark gluon scattering in QCD and gluino gluon scattering in supersymmetric Yang-Mills theory*, *JHEP* **06** (2003) 028, [[hep-ph/0304168](#)].

[17] Q. Jin and H. Luo, *Analytic Form of the Three-loop Four-gluon Scattering Amplitudes in Yang-Mills Theory*, [1910.05889](#).

[18] T. Ahmed, J. Henn and B. Mistlberger, *Four-particle scattering amplitudes in QCD at NNLO to higher orders in the dimensional regulator*, *JHEP* **12** (2019) 177, [[1910.06684](#)].

[19] F. Caola, A. Chakraborty, G. Gambuti, A. von Manteuffel and L. Tancredi, *Three-loop helicity amplitudes for four-quark scattering in massless QCD*, *JHEP* **10** (2021) 206, [[2108.00055](#)].

[20] F. Caola, A. Chakraborty, G. Gambuti, A. von Manteuffel and L. Tancredi, *Three-Loop Gluon Scattering in QCD and the Gluon Regge Trajectory*, *Phys. Rev. Lett.* **128** (2022) 212001, [[2112.11097](#)].

[21] S. Badger, H. Frellesvig and Y. Zhang, *A Two-Loop Five-Gluon Helicity Amplitude in QCD*, *JHEP* **12** (2013) 045, [[1310.1051](#)].

[22] S. Badger, G. Mogull, A. Ochirov and D. O’Connell, *A Complete Two-Loop, Five-Gluon Helicity Amplitude in Yang-Mills Theory*, *JHEP* **10** (2015) 064, [[1507.08797](#)].

[23] T. Gehrmann, J. M. Henn and N. A. Lo Presti, *Analytic form of the two-loop planar five-gluon all-plus-helicity amplitude in QCD*, *Phys. Rev. Lett.* **116** (2016) 062001, [[1511.05409](#)].

[24] S. Abreu, J. Dormans, F. Febres Cordero, H. Ita and B. Page, *Analytic Form of Planar Two-Loop Five-Gluon Scattering Amplitudes in QCD*, *Phys. Rev. Lett.* **122** (2019) 082002, [[1812.04586](#)].

[25] S. Badger, C. Brønnum-Hansen, H. B. Hartanto and T. Peraro, *Analytic helicity amplitudes for two-loop five-gluon scattering: the single-minus case*, *JHEP* **01** (2019) 186, [[1811.11699](#)].

[26] S. Badger, D. Chicherin, T. Gehrmann, G. Heinrich, J. M. Henn, T. Peraro, P. Wasser, Y. Zhang and S. Zoia, *Analytic form of the full two-loop five-gluon all-plus helicity amplitude*, *Phys. Rev. Lett.* **123** (2019) 071601, [[1905.03733](#)].

[27] S. Abreu, J. Dormans, F. Febres Cordero, H. Ita, B. Page and V. Sotnikov, *Analytic Form of the Planar Two-Loop Five-Parton Scattering Amplitudes in QCD*, *JHEP* **05** (2019) 084, [[1904.00945](#)].

[28] S. Abreu, F. Febres Cordero, H. Ita, B. Page and V. Sotnikov, *Leading-color two-loop QCD corrections for three-jet production at hadron colliders*, *JHEP* **07** (2021) 095, [[2102.13609](#)].

[29] B. Agarwal, F. Buccioni, F. Devoto, G. Gambuti, A. von Manteuffel and L. Tancredi, *Five-parton scattering in QCD at two loops*, *Phys. Rev. D* **109** (2024) 094025, [[2311.09870](#)].

[30] G. De Laurentis, H. Ita, M. Klinkert and V. Sotnikov, *Double-virtual NNLO QCD corrections for five-parton scattering. I. The gluon channel*, *Phys. Rev. D* **109** (2024) 094023, [[2311.10086](#)].

[31] G. De Laurentis, H. Ita and V. Sotnikov, *Double-virtual NNLO QCD corrections for five-parton scattering. II. The quark channels*, *Phys. Rev. D* **109** (2024) 094024, [[2311.18752](#)].

[32] N. Arkani-Hamed, F. Cachazo and J. Kaplan, *What is the Simplest Quantum Field Theory?*, *JHEP* **09** (2010) 016, [[0808.1446](#)].

[33] N. Arkani-Hamed, L. J. Dixon, A. J. McLeod, M. Spradlin, J. Trnka and A. Volovich, *Solving Scattering in $N = 4$ Super-Yang-Mills Theory*, [2207.10636](#).

[34] L. F. Alday and J. M. Maldacena, *Gluon scattering amplitudes at strong coupling*, *JHEP* **06** (2007) 064, [[0705.0303](#)].

[35] A. Brandhuber, P. Heslop and G. Travaglini, *MHV amplitudes in $N=4$ super Yang-Mills and Wilson loops*, *Nucl. Phys. B* **794** (2008) 231–243, [[0707.1153](#)].

[36] J. M. Drummond, J. Henn, G. P. Korchemsky and E. Sokatchev, *Hexagon Wilson loop = six-gluon MHV amplitude*, *Nucl. Phys. B* **815** (2009) 142–173, [[0803.1466](#)].

[37] N. Berkovits and J. Maldacena, *Fermionic T-Duality, Dual Superconformal Symmetry, and the Amplitude/Wilson Loop Connection*, *JHEP* **09** (2008) 062, [[0807.3196](#)].

[38] S. Caron-Huot, *Notes on the scattering amplitude / Wilson loop duality*, *JHEP* **07** (2011) 058, [[1010.1167](#)].

[39] L. J. Mason and D. Skinner, *The Complete Planar S-matrix of $N=4$ SYM as a Wilson Loop in Twistor Space*, *JHEP* **12** (2010) 018, [[1009.2225](#)].

[40] E. Witten, *Perturbative gauge theory as a string theory in twistor space*, *Commun. Math. Phys.* **252** (2004) 189–258, [[hep-th/0312171](#)].

[41] R. Britto, F. Cachazo and B. Feng, *New recursion relations for tree amplitudes of gluons*, *Nucl. Phys. B* **715** (2005) 499–522, [[hep-th/0412308](#)].

[42] R. Britto, F. Cachazo, B. Feng and E. Witten, *Direct proof of tree-level recursion relation in Yang-Mills theory*, *Phys. Rev. Lett.* **94** (2005) 181602, [[hep-th/0501052](#)].

[43] L. J. Mason and D. Skinner, *Scattering Amplitudes and BCFW Recursion in Twistor Space*, *JHEP* **01** (2010) 064, [[0903.2083](#)].

[44] N. Arkani-Hamed, J. L. Bourjaily, F. Cachazo, S. Caron-Huot and J. Trnka, *The All-Loop Integrand For Scattering Amplitudes in Planar $N=4$ SYM*, *JHEP* **01** (2011) 041, [[1008.2958](#)].

[45] F. Cachazo, *Sharpening The Leading Singularity*, [0803.1988](#).

[46] M. Bullimore, L. J. Mason and D. Skinner, *Twistor-Strings, Grassmannians and Leading Singularities*, *JHEP* **03** (2010) 070, [[0912.0539](#)].

[47] N. Arkani-Hamed, J. L. Bourjaily, F. Cachazo and J. Trnka, *Local Integrals for Planar Scattering Amplitudes*, *JHEP* **06** (2012) 125, [[1012.6032](#)].

[48] N. Arkani-Hamed, J. L. Bourjaily, F. Cachazo, A. B. Goncharov, A. Postnikov and J. Trnka,

Grassmannian Geometry of Scattering Amplitudes. Cambridge University Press, 4, 2016.
 10.1017/CBO9781316091548.

- [49] N. Arkani-Hamed and J. Trnka, *The Amplituhedron*, *JHEP* **10** (2014) 030, [[1312.2007](#)].
- [50] N. Arkani-Hamed and J. Trnka, *Into the Amplituhedron*, *JHEP* **12** (2014) 182, [[1312.7878](#)].
- [51] A. B. Goncharov, M. Spradlin, C. Vergu and A. Volovich, *Classical Polylogarithms for Amplitudes and Wilson Loops*, *Phys. Rev. Lett.* **105** (2010) 151605, [[1006.5703](#)].
- [52] C. Duhr, H. Gangl and J. R. Rhodes, *From polygons and symbols to polylogarithmic functions*, *JHEP* **10** (2012) 075, [[1110.0458](#)].
- [53] J. Golden, A. B. Goncharov, M. Spradlin, C. Vergu and A. Volovich, *Motivic Amplitudes and Cluster Coordinates*, *JHEP* **01** (2014) 091, [[1305.1617](#)].
- [54] J. Golden, M. F. Paulos, M. Spradlin and A. Volovich, *Cluster Polylogarithms for Scattering Amplitudes*, *J. Phys. A* **47** (2014) 474005, [[1401.6446](#)].
- [55] S. Caron-Huot, L. J. Dixon, J. M. Drummond, F. Dulat, J. Foster, O. Gürdö̈an, M. von Hippel, A. J. McLeod and G. Papathanasiou, *The Steinmann Cluster Bootstrap for $N = 4$ Super Yang-Mills Amplitudes*, *PoS CORFU2019* (2020) 003, [[2005.06735](#)].
- [56] J. Drummond, J. Foster, Ö. Gürdö̈an and C. Kalousios, *Algebraic singularities of scattering amplitudes from tropical geometry*, *JHEP* **04** (2021) 002, [[1912.08217](#)].
- [57] S. He, Z. Li and Q. Yang, *Kinematics, cluster algebras and Feynman integrals*, [2112.111842](#).
- [58] L. J. Dixon, J. M. Drummond and J. M. Henn, *Bootstrapping the three-loop hexagon*, *JHEP* **11** (2011) 023, [[1108.4461](#)].
- [59] L. J. Dixon, J. M. Drummond, C. Duhr, M. von Hippel and J. Pennington, *Bootstrapping six-gluon scattering in planar $N=4$ super-Yang-Mills theory*, *PoS LL2014* (2014) 077, [[1407.4724](#)].
- [60] L. J. Dixon and M. von Hippel, *Bootstrapping an NMHV amplitude through three loops*, *JHEP* **10** (2014) 065, [[1408.1505](#)].
- [61] J. M. Drummond, G. Papathanasiou and M. Spradlin, *A Symbol of Uniqueness: The Cluster Bootstrap for the 3-Loop MHV Heptagon*, *JHEP* **03** (2015) 072, [[1412.3763](#)].
- [62] L. J. Dixon, M. von Hippel and A. J. McLeod, *The four-loop six-gluon NMHV ratio function*, *JHEP* **01** (2016) 053, [[1509.08127](#)].
- [63] S. Caron-Huot, L. J. Dixon, A. McLeod and M. von Hippel, *Bootstrapping a Five-Loop Amplitude Using Steinmann Relations*, *Phys. Rev. Lett.* **117** (2016) 241601, [[1609.00669](#)].
- [64] L. J. Dixon, J. Drummond, T. Harrington, A. J. McLeod, G. Papathanasiou and M. Spradlin, *Heptagons from the Steinmann Cluster Bootstrap*, *JHEP* **02** (2017) 137, [[1612.08976](#)].
- [65] J. Drummond, J. Foster, Ö. Gürdö̈an and G. Papathanasiou, *Cluster adjacency and the four-loop NMHV heptagon*, *JHEP* **03** (2019) 087, [[1812.04640](#)].
- [66] S. Caron-Huot, L. J. Dixon, F. Dulat, M. von Hippel, A. J. McLeod and G. Papathanasiou, *Six-Gluon amplitudes in planar $\mathcal{N} = 4$ super-Yang-Mills theory at six and seven loops*, *JHEP* **08** (2019) 016, [[1903.10890](#)].
- [67] S. Caron-Huot, L. J. Dixon, F. Dulat, M. Von Hippel, A. J. McLeod and G. Papathanasiou, *The Cosmic Galois Group and Extended Steinmann Relations for Planar $\mathcal{N} = 4$ SYM Amplitudes*, *JHEP* **09** (2019) 061, [[1906.07116](#)].

[68] L. J. Dixon and Y.-T. Liu, *An eight loop amplitude via antipodal duality*, *JHEP* **09** (2023) 098, [[2308.08199](#)].

[69] S. He, X. Jiang, X. Li and J. Liu, *Heptagon Symbols at Five Loops and All-Loop Sequences*, [2511.09669](#).

[70] J. M. Drummond, J. Henn, G. P. Korchemsky and E. Sokatchev, *Dual superconformal symmetry of scattering amplitudes in $N=4$ super-Yang-Mills theory*, *Nucl. Phys. B* **828** (2010) 317–374, [[0807.1095](#)].

[71] J. M. Drummond, J. M. Henn and J. Plefka, *Yangian symmetry of scattering amplitudes in $N=4$ super Yang-Mills theory*, *JHEP* **05** (2009) 046, [[0902.2987](#)].

[72] Z. Bern, L. J. Dixon and V. A. Smirnov, *Iteration of planar amplitudes in maximally supersymmetric Yang-Mills theory at three loops and beyond*, *Phys. Rev. D* **72** (2005) 085001, [[hep-th/0505205](#)].

[73] J. M. Henn, *What Can We Learn About QCD and Collider Physics from $N=4$ Super Yang-Mills?*, *Ann. Rev. Nucl. Part. Sci.* **71** (2021) 87–112, [[2006.00361](#)].

[74] A. V. Kotikov and L. N. Lipatov, *DGLAP and BFKL equations in the $N = 4$ supersymmetric gauge theory*, *Nucl. Phys. B* **661** (2003) 19–61, [[hep-ph/0208220](#)].

[75] A. V. Kotikov, L. N. Lipatov, A. I. Onishchenko and V. N. Velizhanin, *Three loop universal anomalous dimension of the Wilson operators in $N = 4$ SUSY Yang-Mills model*, *Phys. Lett. B* **595** (2004) 521–529, [[hep-th/0404092](#)].

[76] A. Brandhuber, G. Travaglini and G. Yang, *Analytic two-loop form factors in $N=4$ SYM*, *JHEP* **05** (2012) 082, [[1201.4170](#)].

[77] Q. Jin and G. Yang, *Hidden Analytic Relations for Two-Loop Higgs Amplitudes in QCD*, *Commun. Theor. Phys.* **72** (2020) 065201, [[1904.07260](#)].

[78] Y. Guo, Q. Jin, L. Wang and G. Yang, *Deciphering the maximal transcendentality principle via bootstrap*, *JHEP* **09** (2022) 161, [[2205.12969](#)].

[79] T. Gehrmann, J. M. Henn and T. Huber, *The three-loop form factor in $N=4$ super Yang-Mills*, *JHEP* **03** (2012) 101, [[1112.4524](#)].

[80] L. J. Dixon, *The Principle of Maximal Transcendentality and the Four-Loop Collinear Anomalous Dimension*, *JHEP* **01** (2018) 075, [[1712.07274](#)].

[81] D. Chicherin and J. M. Henn, *Symmetry properties of Wilson loops with a Lagrangian insertion*, *JHEP* **07** (2022) 057, [[2202.05596](#)].

[82] D. Chicherin and J. Henn, *Pentagon Wilson loop with Lagrangian insertion at two loops in $N = 4$ super Yang-Mills theory*, *JHEP* **07** (2022) 038, [[2204.00329](#)].

[83] J. M. Henn and W. J. T. Bobadilla, *Maximal transcendental weight contribution of scattering amplitudes*, *JHEP* **03** (2022) 174, [[2112.08900](#)].

[84] J. Henn, B. Power and S. Zoia, *Conformal Invariance of the One-Loop All-Plus Helicity Scattering Amplitudes*, *JHEP* **02** (2020) 019, [[1911.12142](#)].

[85] J. Henn, A. Matijašić, J. Miczajka, T. Peraro, Y. Xu and Y. Zhang, *Complete Function Space for Planar Two-Loop Six-Particle Scattering Amplitudes*, *Phys. Rev. Lett.* **135** (2025) 031601, [[2501.01847](#)].

[86] S. Abreu, P. F. Monni, B. Page and J. Usovitsch, *Planar six-point Feynman integrals for four-dimensional gauge theories*, *JHEP* **06** (2025) 112, [[2412.19884](#)].

[87] L. J. Dixon, A. J. McLeod and M. Wilhelm, *A Three-Point Form Factor Through Five Loops*, *JHEP* **04** (2021) 147, [[2012.12286](#)].

[88] L. J. Dixon, O. Gurdogan, A. J. McLeod and M. Wilhelm, *Folding Amplitudes into Form Factors: An Antipodal Duality*, *Phys. Rev. Lett.* **128** (2022) 111602, [[2112.06243](#)].

[89] L. J. Dixon, O. Gurdogan, A. J. McLeod and M. Wilhelm, *Bootstrapping a stress-tensor form factor through eight loops*, *JHEP* **07** (2022) 153, [[2204.11901](#)].

[90] L. J. Dixon, O. Gürdogan, Y.-T. Liu, A. J. McLeod and M. Wilhelm, *Antipodal Self-Duality for a Four-Particle Form Factor*, *Phys. Rev. Lett.* **130** (2023) 111601, [[2212.02410](#)].

[91] B. Basso, L. J. Dixon and A. G. Tumanov, *The three-point form factor of $\text{Tr } \phi^3$ to six loops*, *JHEP* **02** (2025) 034, [[2410.22402](#)].

[92] S. Carrôlo, D. Chicherin, J. Henn, Q. Yang and Y. Zhang, *Bootstrapping Six-Gluon QCD Amplitudes*, [2510.20565](#).

[93] J. L. Bourjaily, E. Herrmann, C. Langer, A. J. McLeod and J. Trnka, *All-Multiplicity Nonplanar Amplitude Integrands in Maximally Supersymmetric Yang-Mills Theory at Two Loops*, *Phys. Rev. Lett.* **124** (2020) 111603, [[1911.09106](#)].

[94] J. L. Bourjaily, S. Caron-Huot and J. Trnka, *Dual-Conformal Regularization of Infrared Loop Divergences and the Chiral Box Expansion*, *JHEP* **01** (2015) 001, [[1303.4734](#)].

[95] J. L. Bourjaily, E. Herrmann and J. Trnka, *Prescriptive Unitarity*, *JHEP* **06** (2017) 059, [[1704.05460](#)].

[96] J. L. Bourjaily, E. Herrmann, C. Langer, A. J. McLeod and J. Trnka, *Prescriptive Unitarity for Non-Planar Six-Particle Amplitudes at Two Loops*, *JHEP* **12** (2019) 073, [[1909.09131](#)].

[97] S. Carrôlo, D. Chicherin, J. Henn, Q. Yang and Y. Zhang, *Hexagonal Wilson loop with Lagrangian insertion at two loops in $\mathcal{N} = 4$ super Yang-Mills theory*, *JHEP* **07** (2025) 214, [[2505.01245](#)].

[98] D. Chicherin, J. Henn, E. Mazzucchelli, J. Trnka, Q. Yang and S.-Q. Zhang, *Geometric Landau Analysis and Symbol Bootstrap*, [2508.05443](#).

[99] J. M. Campbell and E. W. N. Glover, *Double unresolved approximations to multiparton scattering amplitudes*, *Nucl. Phys. B* **527** (1998) 264–288, [[hep-ph/9710255](#)].

[100] S. Catani and M. Grazzini, *Collinear factorization and splitting functions for next-to-next-to-leading order QCD calculations*, *Phys. Lett. B* **446** (1999) 143–152, [[hep-ph/9810389](#)].

[101] V. Del Duca, A. Frizzo and F. Maltoni, *Factorization of tree QCD amplitudes in the high-energy limit and in the collinear limit*, *Nucl. Phys. B* **568** (2000) 211–262, [[hep-ph/9909464](#)].

[102] D. A. Kosower, *Antenna factorization in strongly ordered limits*, *Phys. Rev. D* **71** (2005) 045016, [[hep-ph/0311272](#)].

[103] S. Catani, D. de Florian and G. Rodrigo, *The Triple collinear limit of one loop QCD amplitudes*, *Phys. Lett. B* **586** (2004) 323–331, [[hep-ph/0312067](#)].

[104] S. Badger, F. Bucini and T. Peraro, *One-loop triple collinear splitting amplitudes in QCD*, *JHEP* **09** (2015) 188, [[1507.05070](#)].

[105] G. F. R. Sborlini, *NLO QCD corrections to triple collinear splitting functions*, *Nucl. Part. Phys. Proc.* **273-275** (2016) 2003–2008, [[1410.1680](#)].

[106] A. Volovich, C. Wen and M. Zlotnikov, *Double Soft Theorems in Gauge and String Theories*, *JHEP* **07** (2015) 095, [[1504.05559](#)].

[107] T. Klose, T. McLoughlin, D. Nandan, J. Plefka and G. Travaglini, *Double-Soft Limits of Gluons and Gravitons*, *JHEP* **07** (2015) 135, [[1504.05558](#)].

[108] Y. J. Zhu, *Double soft current at one-loop in QCD*, [2009.08919](#).

[109] M. Czakon, F. Eschment and T. Schellenberger, *Revisiting the double-soft asymptotics of one-loop amplitudes in massless QCD*, *JHEP* **04** (2023) 065, [[2211.06465](#)].

[110] K.-T. Chen, *Iterated path integrals*, *Bull. Am. Math. Soc.* **83** (1977) 831–879.

[111] Z. Bern, L. J. Dixon, D. C. Dunbar and D. A. Kosower, *One loop n point gauge theory amplitudes, unitarity and collinear limits*, *Nucl. Phys. B* **425** (1994) 217–260, [[hep-ph/9403226](#)].

[112] G. F. Sterman and M. E. Tejeda-Yeomans, *Multiloop amplitudes and resummation*, *Phys. Lett. B* **552** (2003) 48–56, [[hep-ph/0210130](#)].

[113] T. Becher and M. Neubert, *Infrared singularities of scattering amplitudes in perturbative QCD*, *Phys. Rev. Lett.* **102** (2009) 162001, [[0901.0722](#)].

[114] L. Magnea and G. F. Sterman, *Analytic continuation of the Sudakov form-factor in QCD*, *Phys. Rev. D* **42** (1990) 4222–4227.

[115] E. Gardi and L. Magnea, *Factorization constraints for soft anomalous dimensions in QCD scattering amplitudes*, *JHEP* **03** (2009) 079, [[0901.1091](#)].

[116] G. P. Korchemsky and A. V. Radyushkin, *Renormalization of the Wilson Loops Beyond the Leading Order*, *Nucl. Phys. B* **283** (1987) 342–364.

[117] I. A. Korchemskaya and G. P. Korchemsky, *On lightlike Wilson loops*, *Phys. Lett. B* **287** (1992) 169–175.

[118] L. J. Dixon, L. Magnea and G. F. Sterman, *Universal structure of subleading infrared poles in gauge theory amplitudes*, *JHEP* **08** (2008) 022, [[0805.3515](#)].

[119] S. Catani, *The Singular behavior of QCD amplitudes at two loop order*, *Phys. Lett. B* **427** (1998) 161–171, [[hep-ph/9802439](#)].

[120] S. M. Aybat, L. J. Dixon and G. F. Sterman, *The Two-loop soft anomalous dimension matrix and resummation at next-to-next-to leading pole*, *Phys. Rev. D* **74** (2006) 074004, [[hep-ph/0607309](#)].

[121] Y. Guo, L. Wang and G. Yang, *Bootstrapping a Two-Loop Four-Point Form Factor*, *Phys. Rev. Lett.* **127** (2021) 151602, [[2106.01374](#)].

[122] Y. Guo, L. Wang and G. Yang, *Analytic four-point lightlike form factors and OPE of null-wrapped polygons*, *Commun. Theor. Phys.* **77** (2025) 055203, [[2209.06816](#)].

[123] D. Chicherin, J. Henn, Y. Xu, S.-Q. Zhang and Y. Zhang, *Three-loop pentagonal Wilson loop with Lagrangian insertion*, [2512.17881](#).

[124] J. Henn, T. Peraro, Y. Xu and Y. Zhang, *A first look at the function space for planar two-loop six-particle Feynman integrals*, *JHEP* **03** (2022) 056, [[2112.10605](#)].

[125] J. M. Henn, A. Matijašić and J. Miczajka, *One-loop hexagon integral to higher orders in the dimensional regulator*, *JHEP* **01** (2023) 096, [[2210.13505](#)].

[126] J. M. Henn, A. Matijasić, J. Miczajka, T. Peraro, Y. Xu and Y. Zhang, *A computation of two-loop six-point Feynman integrals in dimensional regularization*, [2403.19742](#).

[127] J. L. Bourjaily, A. DiRe, A. Shaikh, M. Spradlin and A. Volovich, *The Soft-Collinear Bootstrap: $N=4$ Yang-Mills Amplitudes at Six and Seven Loops*, *JHEP* **03** (2012) 032, [[1112.6432](#)].

[128] J. M. Henn, T. Peraro, M. Stahlhofen and P. Wasser, *Matter dependence of the four-loop cusp anomalous dimension*, *Phys. Rev. Lett.* **122** (2019) 201602, [[1901.03693](#)].

[129] J. L. Bourjaily, E. Herrmann, C. Langer, K. Patatoukos, J. Trnka and M. Zheng, *Integrands of less-supersymmetric Yang-Mills at one loop*, *JHEP* **03** (2022) 126, [[2112.06901](#)].

[130] T. V. Brown, U. Oktem and J. Trnka, *Poles at infinity in on-shell diagrams*, *JHEP* **02** (2023) 003, [[2212.06840](#)].

[131] Z. Bern and A. G. Morgan, *Massive loop amplitudes from unitarity*, *Nucl. Phys. B* **467** (1996) 479–509, [[hep-ph/9511336](#)].

[132] S. D. Badger, *Direct Extraction Of One Loop Rational Terms*, *JHEP* **01** (2009) 049, [[0806.4600](#)].

[133] R. K. Ellis, Z. Kunszt, K. Melnikov and G. Zanderighi, *One-loop calculations in quantum field theory: from Feynman diagrams to unitarity cuts*, *Phys. Rept.* **518** (2012) 141–250, [[1105.4319](#)].

[134] D. C. Dunbar, *One-Loop Six Gluon Amplitude*, [0901.1202](#).

[135] Z. Bern, L. J. Dixon, D. A. Kosower, R. Roiban, M. Spradlin, C. Vergu and A. Volovich, *The Two-Loop Six-Gluon MHV Amplitude in Maximally Supersymmetric Yang-Mills Theory*, *Phys. Rev. D* **78** (2008) 045007, [[0803.1465](#)].

[136] D. A. Kosower, *All order collinear behavior in gauge theories*, *Nucl. Phys. B* **552** (1999) 319–336, [[hep-ph/9901201](#)].

[137] Z. Bern, L. J. Dixon and D. A. Kosower, *Two-loop $g \rightarrow gg$ splitting amplitudes in QCD*, *JHEP* **08** (2004) 012, [[hep-ph/0404293](#)].

[138] D. A. Kosower and P. Uwer, *One loop splitting amplitudes in gauge theory*, *Nucl. Phys. B* **563** (1999) 477–505, [[hep-ph/9903515](#)].

[139] C. Anastasiou, Z. Bern, L. J. Dixon and D. A. Kosower, *Planar amplitudes in maximally supersymmetric Yang-Mills theory*, *Phys. Rev. Lett.* **91** (2003) 251602, [[hep-th/0309040](#)].

[140] Z. Bern, V. Del Duca and C. R. Schmidt, *The Infrared behavior of one loop gluon amplitudes at next-to-next-to-leading order*, *Phys. Lett. B* **445** (1998) 168–177, [[hep-ph/9810409](#)].

[141] S. D. Badger and E. W. N. Glover, *Two loop splitting functions in QCD*, *JHEP* **07** (2004) 040, [[hep-ph/0405236](#)].

[142] J. L. Bourjaily, *The Supersymmetry of Cuts in Pure Gauge Theory and Gravity*, [2512.24984](#).

[143] H. Elvang, Y.-t. Huang and C. Peng, *On-shell superamplitudes in $N < 4$ SYM*, *JHEP* **09** (2011) 031, [[1102.4843](#)].

[144] D. C. Dunbar, J. H. Godwin, G. R. Jehu and W. B. Perkins, *Analytic all-plus-helicity gluon amplitudes in QCD*, *Phys. Rev. D* **96** (2017) 116013, [[1710.10071](#)].

[145] D. C. Dunbar, J. H. Godwin, W. B. Perkins and J. M. W. Strong, *Color Dressed Unitarity*

and Recursion for Yang-Mills Two-Loop All-Plus Amplitudes, *Phys. Rev. D* **101** (2020) 016009, [[1911.06547](#)].

- [146] D. Forde, Direct extraction of one-loop integral coefficients, *Phys. Rev. D* **75** (2007) 125019, [[0704.1835](#)].
- [147] N. Arkani-Hamed, Q. Cao, J. Dong, C. Figueiredo and S. He, Surface Kinematics and the Canonical Yang-Mills All-Loop Integrand, *Phys. Rev. Lett.* **134** (2025) 171601, [[2408.11891](#)].
- [148] S. Badger, G. Mogull and T. Peraro, Local integrands for two-loop all-plus Yang-Mills amplitudes, *JHEP* **08** (2016) 063, [[1606.02244](#)].
- [149] A. V. Smirnov and M. Zeng, FIRE 7: Automatic Reduction with Modular Approach, [2510.07150](#).
- [150] F. Lange, J. Usovitsch and Z. Wu, Kira 3: integral reduction with efficient seeding and optimized equation selection, [2505.20197](#).
- [151] P. Benincasa and F. Cachazo, Consistency Conditions on the S-Matrix of Massless Particles, [0705.4305](#).
- [152] V. Del Duca and L. J. Dixon, The SAGEX review on scattering amplitudes Chapter 15: The multi-Regge limit, *J. Phys. A* **55** (2022) 443016, [[2203.13026](#)].